Doctoral Thesis

Shibaura Institute of Technology

Low-cost routes and optimal processing conditions for mass production of $REBa_2Cu_3O_y$ bulk superconductors

2021/September

Sunsanee Pinmangkorn

Low-Cost Routes and Optimal Processing Conditions for Mass Production of $REBa_2Cu_3O_y$ Bulk Superconductors

Sunsanee Pinmangkorn

A dissertation submitted in fulfillment of
the requirements for the degree of
Doctor of Philosophy

Regional Environment Systems

Graduate School of Engineering and Science

Shibaura Institute of Technology

2021 September

Declaration

I hereby declare that except where specific reference is made to the work of others, the contents of this dissertation are original and have not been submitted in whole or in part for consideration for any other degree or qualification in this, or any other university. This dissertation is my own work and contains nothing that is the outcome of work done in collaboration with others, except as specified in the text and acknowledgments.

Signed:

(Sunsanee Pinmangkorn, NA18505)

Certified by:

(Prof. Dr. Muralidhar Miryala)

Acknowledgements

My deepest thanks and appreciation are given to my supervisor, Prof. Muralidhar Miryala, for his support and guidance of my wonderful journey at Shibaura Institute of Technology (SIT). Thank you for always motivating and pushing me forward towards my goals. I would like to thank Prof. Masato Murakami for his support and great opportunity.

I would like to thank my committee member, Prof. Takasaki Akito, Prof. Naomichi Sakai, Prof. Tomoyuki Naito and Prof. Paolo Mele. Also, professors in superconducting materials laboratory, Prof. Tetsuo Oka and Prof. Ayako Yamamoto, and all of students for their kind support during my course. Especially, Dr. Sai Srikanth Arvapalli for your help and kind support. In addition, Techno-plaza staff for helping me. Moreover, Ass.Prof.Dr.Atikorn Wongsatanawarid, who always kindly gave suggestion and support since my undergraduate level, I'm so grateful for your support.

I would like to thank SIT for providing the financial support for doctoral program (SIT scholarship). My three years as a PhD. student in SIT has been an honor and pride for me and my family. I had a lot of good chances to study, to do research and have experiences with international friends and cultures. I have a fabulous journey.

Finally, I most gratefully acknowledge my parents, my siblings, my chubby niece and my friends for all their huge support, I couldn't have done it without you. I'm glad that I have all you guys. I couldn't be more thankful. Please wait for a while :)

Sunsanee Pinmangkorn

Abstract

High temperature bulk $REBa_2Cu_3O_y$ (RE-123/RE: Nd, Eu, Gd, Y, Er) superconductors are attractive for superconducting super-magnet applications since they are able to trap high magnetic fields at liquid nitrogen temperature. Use of liquid nitrogen (boiling point 77.3 K) as a coolant is considerably cheaper than use of liquid helium (4.2 K). To widely explore these special properties, this material has to be fabricated in large amounts, which would also reduce its cost. The operation cost would be considerably reduced if critical temperature (T_c) of the superconductor was well above 77 K, typically above 90 K. In this thesis, two main issues on this superconductor were discussed. First, we focus on the refinement of RE_2BaCuO_5 (RE-211) secondary phase particles by high-energy ultra-sonication in order to improve the material performance and the cost. The second issue is fabrication of a new ternary $(Gd,Y,Er)Ba_2Cu_3O_y$ ((Gd,Y,Er)-123) compound with a considerable critical current density (J_c) and trapped field (TF) performance, produced in air. All RE-123, RE-211 and liquid phase powders used in this study were self-synthesized.

For the effective refinement of RE-211 secondary phase particles to suitable size by ultra-sonication technique, the ultra-sonication conditions had to be optimized. This technique provides an advantage of a contamination-less operation since the samples are not corrupted by any additives. In this technique, the ultra-sonic wave bombarded the Y-211 particles. The frequency and power were fixed constant at 20 Hz and 300 W, respectively, and the bombardment time varied from 0 to 100 min. We also observed that the shape of Y-211 secondary phase particles changed from the sphere-like to irregular shapes after bombarding by the ultra-sonic wave. For the PtO_2 was added to Y-123 for inhibiting grain growth of the Y-211 particles. The optimum time of ultra-sonication was found to be 80 minutes by top-

seeded melt growth (TSMG). With 0.5 wt% of PtO_2 addition the J_c value and TF increased twice compared to the standard process, where no ultra-sonic wave was applied, and no PtO_2 was added.

In the second step, we focused on the composition of the mixed RE-123 compound due to their exceptional superconducting ability because of several defect structures present. The ternary $(Gd_{0.33},Y_{0.33-x},Er_{0.33+x})Ba_2Cu_3O_y$ superconductor named as (Gd,Y,Er)-123 was chosen for this study, with the content factor X varying from 0 to 0.2. For the fabrication of the bulk superconductor, the calcined (Gd,Y,Er)-211 powder was used as a precursor, and the infiltration growth (IG) process was chosen to overcome the inherent problems occurring in TSMG. The values of J_c and TF increased monotonously with the Er increment. The microstructural and chemical analysis showed that the fine secondary phase particles uniformly dispersed in the (Gd,Y,Er)-123 matrix, and were rich in Er. The superconducting properties of ternary (Gd,Y,Er)-123 improved with respect to Y-123. However, the study of the entire bulk superconductor showed a spatial variation of superconducting properties. In the microstructure, a variation in (Gd,Y,Er)-211 particle size was also observed in the as-grown bulk sample.

The ultra-sonication conditions optimized for the ternary bulk (Gd,Y,Er)-123 fabrication process helped to improve superconducting properties of the ternary bulk. The highest J_c and TF values were achieved in $(Gd_{0.33},Y_{0.13},Er_{0.53})Ba_2Cu_3O_y$ sample. The self-field J_c at 77 K increased by 20% compared to that of the standard sample made of calcined (Gd,Y,Er)-211 powder. Moreover, the newly developed mixed RE system exhibited the higher J_c at both low and high magnetic fields. This J_c improvement in a wide range of magnetic fields at liquid nitrogen temperature provides an exceptional advantage for commercial applications.

Contents

List of Publications **vii**

List of Figures **xi**

List of Tables **xvii**

Abbreviations **xxi**

1 Introduction **1**

1.1 Superconductivity 1

1.1.1 Background 1

1.1.2 Meissner effect 2

1.1.3 Types of superconductors 3

1.1.3 (a) Type I superconductor 3

1.1.3 (b) Type II superconductor 4

1.1.4 Coherence length (ξ) 5

1.1.5 Penetration depth (λ) 5

1.1.6 Phenomenological theories 6

1.1.6 (a) London theory 6

1.1.6 (b) BCS theory 6

1.2 Superconducting properties 7

1.2.1 Critical temperature (T_c) 7

1.2.2 Critical current density (J_c) 7

1.2.3 Trapped field (TF) 7
1.2.4 Flux pinning 8
1.3 Applications 10
1.4 Historical background of high temperature superconductors 10
1.4.1 Phase diagram 11
1.4.2 Crystal structure 12
1.4.3 Processing 14
1.4.4 Seeding techniques 17
1.5 Research objectives 18
References 20

2 Experimental Details 27

2.1 Synthesis 28
2.1.1 Powders preparation 28
2.1.2 Melt growth process 34
2.1.2 (a) Top seeded melt growth (TSMG) 34
2.1.2 (b) Infiltration growth (IG) 36
2.1.3 Oxygen annealing 37
2.1.4 Refinement techniques 38
2.1.4 (a) Ultra-sonication technique 38
2.1.4 (b) PtO_2 addition 39
2.2 Characterization techniques 39
2.2.1 X-ray diffraction (XRD) 39
2.2.2 Differential thermal analysis (DTA) 40
2.2.3 Field emission scanning electron microscopy (FESEM) and energy dispersive x-ray (EDX) analysis 40
2.2.4 Superconducting quantum interference device (SQUID) 41
2.2.5 Hall probe scanning 42
References 43

3 Bulk $YBa_2Cu_3O_y$ Superconductors with Ultra-sonicated Y_2BaCuO_5 Secondary Phase Particles **45**

3.1 Introduction 45

3.2 Experimental details 47

3.3 Results and discussion 48

3.3.1 Ultra-sonicated Y_2BaCuO_5 secondary phase particle analysis 48

3.3.2 Fabrication of bulk Y-123 superconductors without PtO_2 addition 52

3.3.2 (a) Fabrication of bulk Y-123 52

3.3.2 (b) Trapped field experiments 53

3.3.2 (c) Superconducting properties 55

3.3.2 (d) Microstructure analysis 58

3.3.3 Fabrication of bulk Y-123 superconductors with PtO_2 addition 60

3.3.3 (a) Fabrication of bulk Y-123 60

3.3.3 (b) Trapped field experiments 62

3.3.3 (c) Superconducting properties 64

3.3.3 (d) Microstructure analysis 66

3.3.4 Comparison of bulk Y-123 superconductors with and without PtO_2 addition 69

3.4 Conclusions 72

References 74

4 Development of Ternary Bulk $(Gd,Y,Er)Ba_2Cu_3O_y$ Superconductor **79**

4.1 Introduction 79

4.2 Experimental details 82

4.3 Results and discussion 84

4.3.1 X-ray diffraction 85

4.3.2 Superconducting properties 86

4.3.3 Microstructure analysis 93

4.4 Conclusions 103

References 104

5 Spatial Variation of $(Gd_{0.33},Y_{0.13},Er_{0.53})Ba_2Cu_3O_y$ Bulk Superconductors 111

5.1 Introduction 111

5.2 Experimental details 112

5.3 Results and discussion 114

5.3.1 Variation of superconducting properties 114

5.3.1 (a) Critical temperature (T_c) 114

5.3.1 (b) Critical current density (J_c) 115

5.3.2 Variation of microstructure 119

5.3.3 Variation of RE-211 pellet in the processes 125

5.4 Conclusions 128

References 130

6 $(Gd,Y,Er)Ba_2Cu_3O_y$ Superconductors with Ultra-sonicated Secondary Phase Particles 133

6.1 Introduction 133

6.2 Experiment details 134

6.3 Results and discussion 135

6.3.1 Ultra-sonicated secondary phase particle analysis 135

6.3.2 Fabrication of bulk $(Gd,Y,Er)Ba_2Cu_3O_y$ superconductors 137

6.3.3 Trapped field experiments 138

6.3.4 Superconducting properties 140

6.3.5 Microstructure analysis 143

6.4 Batch production of bulk $(Gd_{0.33},Y_{0.13},Er_{0.53})$-123 145

6.5 Conclusions 149

References 151

7 Conclusions and Future Prospect **155**

7.1 Conclusions 155

7.2 Future prospect 159

List of Publications

Journal Papers:

[1] **S. Pinmangkorn,** M. Miryala, S.S. Arvapalli, M Jirsa, T. Oka, N. Sakai, M. Murakami, (Gd,Y,Er)$Ba_2Cu_3O_y$ bulk superconducting system processed via infiltration growth, *J. Alloy Comd.,* Vol 881, 160535, 2021

[2] **S. Pinmangkorn**, M. Miryala, S. S. Arvapalli and M. Murakami, "Enhancing the superconducting performance of melt grown bulk $YBa_2Cu_3O_y$ via ultrasonically refined Y_2BaCuO_5 without PtO_2 and CeO_2"**,** *Mater. Chem. Phys.*, 244:122721, 2020

[3] **S. Pinmangkorn**, M. Miryala, S. S. Arvapalli and M. Murakami, "Effect of Ultra-sonicated Y_2BaCuO_5 on Top-Seeded Melt Growth $YBa_2Cu_3O_y$ Bulk Superconductor", *J. Supercond. Nov. Magn.*, Vol 33, pages 1667–1673, 2020

[4] **S. Pinmangkorn**, M. Miryala, S. S. Arvapalli and M. Murakami, "Y_2BaCuO_5 Particle Size Control via Ultrasonication and its Effect on Bulk $YBa_2Cu_3O_y$ Superconductor", *IOP conf. ser., Mater. sci. eng.*, 773, 012017, 2020

[5] Alish Nursyahirah Kamarudin, Mohd Mustafa Awang Kechik, Muralidhar Miryala, **Sunsanee Pinmangkorn**, Masato Murakami, Soo Kien Chen, Hussein Baqiah, Aima Ramli, Kean Pah Lim, and Abdul Halim Shaari, "Microstructure, Phase Formation, and Superconducting Properties of Bulk $YBa_2Cu_3O_y$ Superconductors Grown by Infiltration

Growth Process Utilizing the $YBa_2Cu_3O_y$+$ErBa_2Cu_3O_y$+$Ba_3Cu_5O_8$ as a Liquid Source", *J. Coatings*., 11, 377, 2021

[6] Arvapalli S S, Muralidhar M, **Pinmangkorn S**, Jirsa M, and Murakami M, "Superconducting properties of sintered bulk MgB_2 prepared from hexane-mediated high-energy-ultra-sonicated boron", *MSEB,* Vol 265, 115030, 2021

[7] Arvapalli S S, Muralidhar M, **Pinmangkorn S**, Jirsa M, Sakai N, Oka T and Murakami M, "Optimization of carbon encapsulated boron doping for high-performance bulk sintered MgB_2", *Adv. Eng. Mater*., 2000478, 2020

[8] M. Muralidhar, **P. Sunsanee**, K. Takemura, A. Sai Srikanth, M.Jisa, M. Murakami, "Recent progress in production of infiltration-growth and melt-growth processed bulk (RE)$Ba_2Cu_3O_y$", *Supercond. Sci. Technol.*, Vol.33, 074002 pp.10, 2020

Presentations:

[1] ***Oral Presentation,*** **P. Sunsanee**, M. Muralidhar, A. Sai Srikanth, N. Sakai, T. Oka and M. Murakami "Properties of infiltration grown (Gd,Y,Er)BCO bulk superconductors", *8th, Green Innovation 2021,* Febuary 26, 2021

[2] ***Oral Presentation,*** **S Pinmangkorn**, M Miryala, S.S Arvapalli and M Murakami, "Superconducting properties of TSIG processed ternary bulk (Gd,Y,Er)$Ba_2Cu_3O_y$", *33rd International Symposium on Superconductivity (ISS2020)*, December 1-3, 2020

[3] ***Oral Presentation,*** Muralidhar Miryala, Sai Srikanth Arvapalli, **Sunsanee Pinmangkorn**, Milos Jirsa, Jacques Noudem, Naomichi Sakai, Tetsuo Oka, and M Murakami, "Low-cost and Improved Critical Current Densitise in Ultra-Sonicated born

added Bulk MgB_2", *33rd International Symposium on Superconductivity (ISS2020)*, December 1-3, 2020

[4] ***Oral Presentation,*** N. Sota, M. Muralidhar, **P. Sunsanee**, A. Sai Srikanth, S. Naomichi, O. Tetsuo, M. Masato, "Variation of Superconducting Properties in Single-Grain Bulk Y123 produced by TSMG and TSIG process", *33rd International Symposium on Superconductivity (ISS2020)*, December 1-3, 2020

[5] ***Oral Presentation,*** Sai Srikanth Arvapalli, Muralidhar Miryala, Yiteng Xing, **Sunsanee Pinmangkorn**, Jacques Noudem, Milos Jirsa, Masato Murakami, "Correlation between superconducting properties and microstructure in silver added MgB_2 bulk", *33rd International Symposium on Superconductivity (ISS2020)*, December 1-3, 2020

[6] ***Oral Presentation,*** **S Pinmangkorn**, M Miryala, S.S Arvapalli and M Murakami, "Flux pinning and superconducting performance of melt grown bulk $YBa_2Cu_3O_y$ via ultrasonically refined Y_2BaCuO_5", *International Symposium on Superconducting, Magnetic and Energy Materials (ISSM 2020)*, October 6-7, 2020

[7] ***Oral Presentation,*** Sai Srikanth Arvapalli, Muralidhar Miryala, **Sunsanee Pinmangkorn**, and Masato Murakami, "Refinement of Commercial Boron using High Energy Ultrasonication", *Japan International Conference on Carbon Materials and Nanotechnology (JICCMAN-2020)*, June 30 -July 1, 2020

[8] ***Oral Presentation,*** **S Pinmangkorn**, M Miryala, S.S Arvapalli and M Murakami, "Optimization of Infiltration Grown Ternary Mixed Rare-Earth Bulk $(Gd,Y,Er)Ba_2Cu_3O_y$ Superconductor", *Japan International Conference on Carbon Materials and Nanotechnology (JICCMAN-2020)*, June 30 -July 1, 2020

[9] ***Poster Presentation,*** **S. Pinmangkorn**, M. Miryala, S. S. Arvapalli and M. Murakami, "Superconducting Performance of Top-Seeded Melt Grown Bulk $YBa_2Cu_3O_y$ Made from Ultrasonicated Y_2BaCuO_5", *7th Green Innovation 2020*, Febuary 18, 2020

[10] ***Oral Presentation,*** **S Pinmangkorn**, M Miryala, S.S Arvapalli and M Murakami, "Y_2BaCuO_5 Particle Size Control via Ultrasonication and its Effect on Bulk $YBa_2Cu_3O_y$ Superconductor", *The 2nd International Conference on Materials Research and Innovation (ICMARI)*, December 16-18, 2019

[11] ***Invited,*** M. Muralidhar, **S. Pinmangkorn**, T. Kento, Arvapalli S S and M Murakami, "Recent progress in production of infiltration-growth and melt-growth processed bulk (RE)Ba2Cu3Oy", *11th International Workshop on Processing and Application of Superconducting Bulk Materials, PASREG2019*, August 29-30, 2019

[12] ***Poster Presentation,*** **S. Pinmangkorn**, M. Miryala, S. S. Arvapalli and M. Murakami, "Effect of Ultrasonicated Y_2BaCuO_5 on superconducting properties of bulk $YBa_2Cu_3O_y$ superconductors grown by TSMG process", *11th International Workshop on Processing and Application of Superconducting Bulk Materials, PASREG2019*, August 29-30, 2019

[13] ***Oral Presentation,*** Sai Srikanth Arvapalli, Miryala Muralidhar, **Pinmangkorn Sunsanee** and Masato Murakami, "Effect of high energy ultra-sonicated Boron on superconducting properties in solid state sintered bulk MgB_2", *11th International Workshop on Processing and Application of Superconducting Bulk Materials, PASREG2019,* August 29-30, 2019

[14] ***Poster Presentation,*** **S. Pinmangkorn**, M. Miryala, S. S. Arvapalli and M. Murakami**,** **"**Novel Processing of High Performance YBCO Superconductors by Ultrasonicated Y211", *14th European Conference on Applied Superconductivity*, September 1-5, 2019

[15] ***Oral Presentation,*** M. Muralidhar, Pavan, **S. Pinmangkorn**, Arvapalli S S and M Murakami, "High performance IG processed bulk YBCO produced with sharp-edge Y211 precipitates", *Applied Superconductivity Conference (ASC 2018),* October 28-November 2, 2018

List of Figures

1.1	The superconducting transition in Hg [2]	2
1.2	Meissner effect	3
1.3	Schematic illustrations showing the magnetic behavior of type I and type II superconductors	4
1.4	The magnetization and field cure showing fluxoids penetrating the superconductor	8
1.5	The Lorentz force acts on the fluxoids when the currents were passed in the mixed state of type II superconductor	9
1.6	Pseudo-binary phase diagram for the Y-123 system [49,50]	11
1.7	Crystal structure of Y-123 (a) a tetragonal structure, and (b) the CuO chains introduces an orthorhombic structure	13
1.8	Dependence of T_c on oxygen content (y: $7-\delta$) in $YBa_2Cu_3O_y$ [33]	14
1.9	Schematic illustration of MG process [15]	15
1.10	Comparison between TSMG and IG process for bulk RE-123 superconductor	16
1.11	(a) Schematic illustration of cold and hot seeding techniques, and top surface of (Gd,Y,Er)-123 sample single from which can be seen growth lines from the seed, and schematic of five-domain morphology (b) in the (001) plane and (c) along the (001) direction.	18
2.1	Temperature profile for calcination of RE-123, RE-211, and LP powders	29
2.2	Y-123 powder after calcination at (a) 860°C, (b) 880°C, (c) 900°C, and (d) 920°C	30

2.3	Y-211 powder after calcination at (a) 820°C, (b) 840°C, (c) 860°C, and (d) 880°C	30
2.4	$Ba_3Cu_5O_8$ powder after calcination at (a) 860°C, and (b) 880°C	31
2.5	XRD result of calcined Y-123 powder; (a) third calcination at T_m = 900°C, and (b) fourth calcination at T_m = 920°C	32
2.6	XRD result of calcined Y-211 powder; (a) third calcination at T_m = 860°C, and (b) fourth calcination at T_m = 880°C	33
2.7	Sample assembly to fabricating Y-123 bulk superconductors by TSMG process; (a) top-view, and (b) side-view of the precursor	35
2.8	Temperature profile for the TSMG process of bulk Y-123 superconductor	35
2.9	Arrangement of the sample assembly for fabricating (Gd,Y,Er)-123 bulk superconductors by IG process (a) top-view, and (b) side-view of the precursor	36
2.10	Temperature profile for the IG process of (Gd,Y,Er)-123 bulk superconductor	37
2.11	Temperature profile for oxygen annealing of bulk (a) Y-123, and (b) (Gd,Y,Er)-123	38
2.12	Refinement of RE-211 particles via ultra-sonication technique	39
3.1	FESEM images and histograms of Y-211 powder of ultra-sonication for (a) 0, (b) 20, (c) 40, (d) 60, (e) 80, and (f) 100 minutes	50
3.2	High magnification FESEM images of Y-211 ultra-sonicated at (a) 0, (b) 80, and (c) 100 minutes	51
3.3	X-Ray diffraction patterns for Y-211 ultra-sonicated at 0-100 minutes	51
3.4	Top view of as-grown (a) Y0, (b) Y20, (c) Y40, (d), Y60, (e) Y80, and (f) Y100 bulk samples	52
3.5	X-Ray diffraction patterns for bulk Y-123 samples fabricated with ultra-sonicated Y-211 for 0-100 minutes	53
3.6	The trapped field distribution under an applied magnetic field of 0.45 T at 77.3 K and 1.3 mm above the top surface for Y100 sample	54

3.7	Trapped field values Y-123 sample without PtO_2 addition under an applied magnetic field of 1 T at 77.3 K and 0.3 mm above the top surface as a function of ultra-sonication times	55
3.8	The temperature dependence of DC susceptibility measurements of bulk Y-123 material fabricated with Y-211 ultra-sonicated	56
3.9	Field dependences of the critical current density of bulk Y-123 samples at 77 K, H//*c*-axis	57
3.10	The normalized flux pinning curve, $F_p / F_{p,max}$ as a function of the reduced field, $h = H_a / H_{irr}$ for Y0 and Y100 samples	59
3.11	FESEM images of a) Y0, and b) Y100 samples	59
3.12	Top view of as-grown (a) YPt0, (b) YPt20, (c) YPt40, (d), YPt60, (e) YPt80, and (f) YPt100 samples	61
3.13	X-Ray diffraction patterns for YPt0, YPt40 and YPt80 samples	62
3.14	The trapped field distribution under an applied magnetic field of 0.45 T at 77.3 K and 1.3 mm above the top surface for YPt80 sample	63
3.15	Trapped field values of Y-123 sample with PtO_2 addition under an applied magnetic field of 1 T at 77.3 K and 0.3 mm above the top surface as a function of ultra-sonication times	63
3.16	The temperature dependence of the normalized DC susceptibility measurements of (a) YPt0, (b) YPt40, and (c) YPt80 samples	65
3.17	Field dependences of the critical current density (J_c) at 77 K, *H//c*-axis of Y-123 with PtO_2 addition samples	66
3.18	FESEM images of a) YPt0 and b) YPt100 samples	67
3.19	Average particles size of Y-211 powders as a function of ultra-sonic times along with inset FESEM images of Y-211 ultra-sonicated at 0 and 80 minutes	69
3.20	Trapped field value measured under a magnetic field of 1 T at 77.3 K as a function of ultra-sonic time	70
3.21	Critical temperature (T_c) as a function of ultra-sonic times	71
3.22	Critical current density (J_c) at 0 T and 2 T as a function of ultra-sonic times	72

4.1	DTA results of ($Gd_{0.33}Y_{0.33-x}Er_{0.33+x}$)-123 powders	83
4.2	(a) Sample assembly, and (b) temperature and time program for fabricate ($Gd_{0.33}Y_{0.33-x}Er_{0.33+x}$)-123 samples	84
4.3	**(**$Gd_{0.33}$,$Y_{0.33-x}$,$Er_{0.33+x}$)-123 single grains growth samples (20 mm in diameter)	85
4.4	X-ray diffraction patterns for ($Gd_{0.33}$,$Y_{0.33-x}$,$Er_{0.33+x}$)-123 samples	86
4.5	The trapped field distribution of (a) X0, (b) X0.05, (c) X0.1, (d) X0.15, and (e) X0.2 sample under an applied magnetic field 1 T at 77.3 K and 1.3 mm above top surface	88
4.6	Trapped field values under an applied field 1 and 0.5 T at 77.3 K as a function of X for ($Gd_{0.33}$,$Y_{0.33-x}$,$Er_{0.33+x}$)-123 samples	89
4.7	The temperature dependence of DC magnetic susceptibility measurements for ($Gd_{0.33}$,$Y_{0.33-x}$,$Er_{0.33+x}$)-123 samples	90
4.8	J_c values at 77 K, H // *c*-axis of ($Gd_{0.33}$,$Y_{0.33-x}$,$Er_{0.33+x}$)-123 samples	90
4.9	J_c values at 77, 70, 65, 60, 55, and 50 K, H // *c*-axis of ($Gd_{0.33}$,$Y_{0.13}$,$Er_{0.53}$)-123, (X=0.2) sample	91
4.10	The normalized pinning force, $F_p/F_{p,max}$, as a function of the reduce field, h = H_a/H_{irr} for ($Gd_{0.33}$,$Y_{0.33-x}$,$Er_{0.33+x}$)-123 samples	92
4.11	FESEM images of (a) X0, (b) X0.05, (c) X0.1, (d) X0.15, and (e) X0.2 samples	95
4.12	EDX area element analysis data for the bulk (a) X0, and (b) X0.2 samples	96
4.13	EDX mapping of X0 sample	98
4.14	EDX mapping of X0.05 sample	99
4.15	EDX mapping of X0.1 sample	100
4.16	EDX mapping of X0.15 sample	101
4.17	EDX mapping of X0.2 sample	102
5.1	(a) Bulk ($Gd_{0.33}$,$Y_{0.13}$,$Er_{0.53}$)-123 sample, and (b) Cutting method, and the label position indicating each specimen of the bulk sample	113
5.2	(a) The preparation of the samples for IG process and temperature profile of RE-211 preforms at (b) 880ºC, and (c) 1050ºC	113

5.3	Temperature dependence of normalized dc magnetization for specimens cut from various positions	114
5.4	J_c-B curves of $(Gd_{0.33},Y_{0.13},Er_{0.53})$-123 bulk sample at various positions	116
5.5	J_c values at self-field, 77 K versus the position in the bulk sample (a) layer 1, (b) layer 2, and (c) layer 3	117
5.6	FESEM images of the layer 1	121
5.7	FESEM images of the layer 2	121
5.8	FESEM images of the layer 3	122
5.9	The histograms of the $(Gd_{0.33},Y_{0.13},Er_{0.53})$-211 secondary particles size in each layer	123
5.10	Surface morphology of RE-211 pellet before heat-up process	125
5.11	The heated samples at (a) 880ºC, (b) 1050ºC and (c) positions of each specimen in the RE-211 preform	126
5.12	FESEM images of RE-211 pellet at various positions of sample quenched at 880ºC	126
5.13	FESEM images of RE-211 pellet at various positions of sample quenched at 1050ºC	127
6.1	FESEM images of calcined and ultra-sonicated Gd-211, Y-211 and Er-211 powders	136
6.2	High magnification of FESEM images of ultra-sonicated Gd-211, Y-211 and Er-211 powders	136
6.3	As-grown bulk $(Gd_{0.33},Y_{0.33-x},Er_{0.33+x})Ba_2Cu_3O_y$ superconductors	137
6.4	Trapped field distribution profiles of (a) XU0, (b) XU0.05, (c) XU0.1, (d) XU0.15, and (e) XU0.2	139
6.5	The temperature dependence of the normalized DC susceptibility measurements	140
6.6	Field dependences of the critical current density (J_c) at 77 K, H//c-axis	141
6.7	J_c values at 77, 70, 65, 60, 55, and 50 K, H // c-axis of $(Gd_{0.33},Y_{0.13},Er_{0.53})$-123, (XU0.2) sample	142

6.8	FESEM images for (a) XU0, (b) XU0.05, (c) XU0.1, (d) XU0.15, and (e) XU0.2 samples	144
6.9	EDX line scan analysis of microstructure and individual element line spectra of (a) and (b) for XU0 sample, (c) and (d) for XU0.2 sample	145
6.10	Three samples of the first batch production of (a) $(Gd_{0.33},Y_{0.13},Er_{0.53})$-123 preform for IG process and (b) set-up samples in the normal box furnace	146
6.11	Six samples of the second batch production of (a) $(Gd_{0.33},Y_{0.13},Er_{0.53})$-123 preform for IG process and (b) set-up samples in the normal box furnace	146
6.12	Top view of as-grown $(Gd_{0.33},Y_{0.13},Er_{0.53})$-123 bulk samples for the first batch production	147
6.13	Top view of as-grown $(Gd_{0.33},Y_{0.13},Er_{0.53})$-123 bulk samples for the second batch production	147
6.14	The trapped field values of each bulk $(Gd_{0.33},Y_{0.33-x},Er_{0.33+x})Ba_2Cu_3O_y$	148
6.15	The trapped field profile at 77.3 K for bulk $(Gd_{0.33},Y_{0.33-x},Er_{0.33+x})Ba_2Cu_3O_y$ of diameter 20 mm.	149

List of Tables

1.1	Peritectic decomposition temperatures (T_P) of the various RE-123 superconductors	12
1.2	Lattice parameters and unit cell volume of $YBa_2Cu_3O_y$ [54]	13
3.1	Superconducting transition temperature, Critical current density (J_c) at self-field and 1T, trapped field at 77 K of the bulk Y-123 superconductor produced ultra-sonicated Y-211, compared to recent results reported in literature	68
4.1	EDX spectra of the X0 sample in Fig. 12(a)	97
4.2	EDX spectra of the X0.2 sample in Fig. 12(b)	97
4.3	EDX mapping element analysis of the X0 sample in Fig 4.13	98
4.4	EDX mapping element analysis of the X0.05 sample in Fig 4.14	99
4.5	EDX mapping element analysis of the X0.1 sample in Fig 4.15	100
4.6	EDX mapping element analysis of the X0.15 sample in Fig 4.16	101
4.7	EDX mapping element analysis of the X0.2 sample in Fig 4.17	102
5.1	T_c values at various positions of $(Gd_{0.33},Y_{0.13},Er_{0.53})$-123 bulk sample	115
5.2	J_c values at various positions and fields of $(Gd_{0.33},Y_{0.13},Er_{0.53})$-123 bulk sample	118
5.3	The secondary $(Gd_{0.33},Y_{0.13},Er_{0.53})$-211 particle size at various positions	124

Abbreviations

Al_2O_3	=	Aluminum oxide
B	=	Boron
Ba	=	Barium
BA-TSMG	=	Buffer-aided top seeded melt growth
BaO_2	=	Barium oxide
BCS	=	Bardeen J., Cooper L., and Schrieffer R.
BEC	=	Bose-Einstein condensation
Bi	=	Bismuth
C	=	Celsius (degree)
c	=	Velocity
Ca	=	Calcium
CeO_2	=	Cerium oxide
Cu	=	Copper
CuO	=	Copper oxide
DTA	=	Differential Thermal Analysis
Dy	=	Dysprosium
E	=	Electric filed
EDX	=	Energy Dispersive X-ray
Er	=	Erbium
ErO_2	=	Erbium oxide
Er-123	=	$ErBa_2Cu_3O_y$
Er-211	=	Er_2BaCuO_5
Eu	=	Europium

F	=	Lorentz force
FC	=	Field cooled
Fe	=	Ferrum
FESEM	=	Field emission scanning electron microscopy
Fig	=	Figure
Ge	=	Germanium
Gd	=	Gadolinium
GdO_2	=	Gadolinium oxide
Gd-123	=	$GdBa_2Cu_3O_y$
Gd-211	=	Gd_2BaCuO_5
GL	=	Ginzburg-Landau
h	=	Hour
H_c	=	Critical magnetic fields
H_{c1}	=	Low critical magnetic fields
H_{c2}	=	High critical magnetic fields
Hg	=	Mercury
Ho	=	Holmium
HTS	=	High temperature superconductors
IG	=	Infiltration growth
J_c	=	Critical current density
K	=	Kelvin
kA	=	Kiloampere
kHz	=	Kilohertz
kN	=	Kilonewton
L	=	Liquid
La	=	Lanthanum
LHe	=	Liquid helium
LN_2	=	Liquid nitrogen
LP	=	Liquid phase
LRE	=	Light rare earth

m	=	Mass
Mg	=	Magnesium
MG	=	Melt growth
MPMG	=	Melt powder melt growth
MTG	=	Melt-texture-growth
MRI	=	Magnetic resonance imaging
M-H	=	Magnetization hysteresis
mm	=	Millimeter
N	=	Nitrogen
n	=	Superconducting electron density
Nd	=	Neodymium
Nd-123	=	$NdBa_2Cu_3O_y$
nm	=	Nanometer
NMR	=	Nuclear magnetic resonance
O	=	Oxygen
OCMG	=	Oxygen-controlled melt growth
Pb	=	Lead
PDF	=	Powder diffraction file
PMP	=	Powder melting
Pt	=	Platinum
PtO_2	=	Platinum oxide
QMG	=	Quench and melt growth
RE	=	Rare earth
RE-123	=	$(RE)Ba_2Cu_3O_y$
RE-211	=	$(RE)_2BaCuO_5$
S	=	Solid
Sm	=	Samarium
SQUID	=	Superconducting Quantum Interference Device
Sr	=	Strontium
T	=	Tesla

T_c	=	Critical temperature
TF	=	Trapped field
Ti	=	Titanium
T_m	=	Maximum temperature
T_p	=	Peritectic temperature
TSMG	=	Top-seeded melt growth
W	=	Watt
wt%	=	Percentage by weight
XRD	=	X-Ray Diffraction
Y	=	Yttrium
Yb	=	Ytterbium
Y_2O_3	=	Yttrium oxide
Y-123	=	$YBa_2Cu_3O_y$
Y-211	=	Y_2BaCuO_5
ZFC	=	Zero field cooled
Zr	=	Zirconium
µm	=	Micrometer
λ	=	Penetration depth
ξ	=	Coherence length
κ	=	GL parameter
$\hbar$	=	Planck's constant
v_F	=	Fermi velocity
ε_0	=	Electric constant,
μ_0	=	Permeability in vacuum
ϕ_0	=	Magnetic flux
e	=	Magnitude of each carrier's charge

Chapter 1

Introduction

1.1 Superconductivity

1.1.1 Background

Superconductivity was first discovered in 1911 by Kamerlingh Onnes when he performed an experiment to measure the electric resistance of solid mercury [1]. Onnes expected a gradual approach of resistivity to zero with progressive decrease in temperature. However, he found that the resistance of mercury dropped to zero in the liquid helium tank (at 4.2 K) as seen in Fig.1.1 [2]. Onnes claimed that this new state of mercury with zero resistivity is the superconducting state.

Since the discovery of superconductivity, many metallic elements exhibited superconducting state below their critical temperature (T_c). In 1930, numerous researchers tried to explore the superconductivity in various compounds and alloys such as Cu-S with

T_c = 1.6 K, Pb-Bi with T_c = 8.8 K, Nd-Ti with T_c = 1.6 K, and in 1941, Nd-N with T_c = 15 K [3].

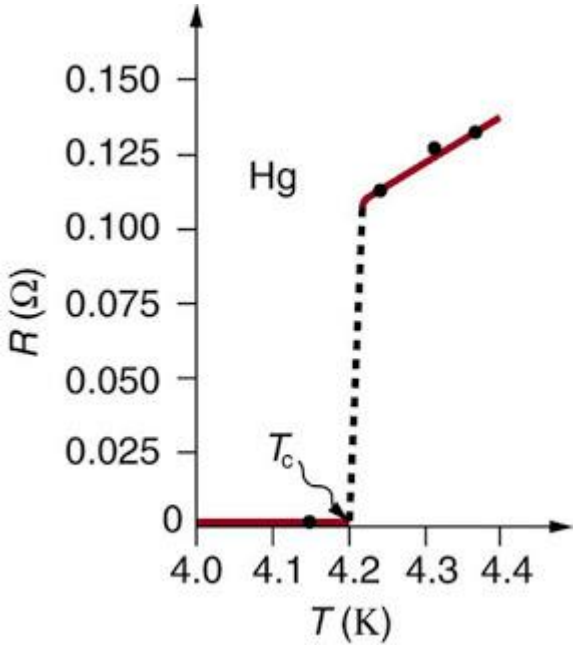

Figure 1.1 The superconducting transition in Hg [2]

1.1.2 Meissner effect

In 1933, Walther Meissner and Robert Ochsenfeld made a significant discovery of the novel superconducting properties at the low applied magnetic field. The superconductors are cooled down below their transition temperature completely expelled the external magnetic field below a certain value, called as the critical magnetic field (H_c) shown in Fig. 1.2. This phenomenon is noted as Meissner effect and the superconductors exhibit perfect diamagnetism [4].

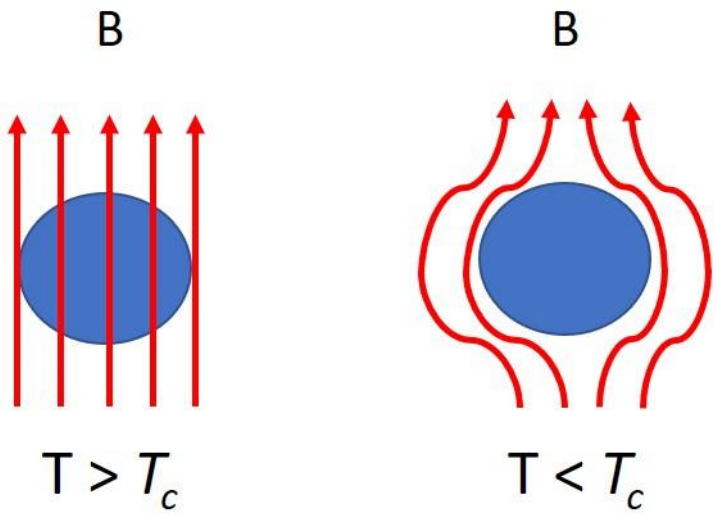

Figure 1.2 Meissner effect

1.1.3 Types of superconductors

The normal conductor is cooled below the T_c of materials and becomes a superconductor. Magnetic behavior of superconducting alloys and metalloids are different when compared with pure metals. There are two different types, which are type I and II superconductors depending on the flux expulsion of the magnetic field [5]. The magnetic behavior of type I and II are illustrated in Fig. 1.3

1.1.3 (a) Type I superconductor

Type I superconductors exhibit the complete Meissner effect and zero resistance below their H_c and T_c. When applied field exceeds H_c, the superconducting properties will be destroyed and becomes a normal conductor. For type I, superconductors are well described by the BCS theory [6].

1.1.3 (b) Type II superconductor

Type II superconductors exhibit different magnetic behavior from type I. There are two critical magnetic fields H_{c1} and H_{c2}. When type II is cooled below the T_c and subjected to a magnetic field $H_a < H_{c1}$, it shows no resistance and interior magnetic fields are completely expelled like a type I superconductors. However, when the field excess $H_{c1,}$ the external magnetic field starts to penetrate the non-superconducting phase and create a mixed state or vortex state in form of a quantized fluxoid. In the mixed state, the material still maintains zero resistance. When $H_a > H_{c2}$, the superconductivity will be destroyed.

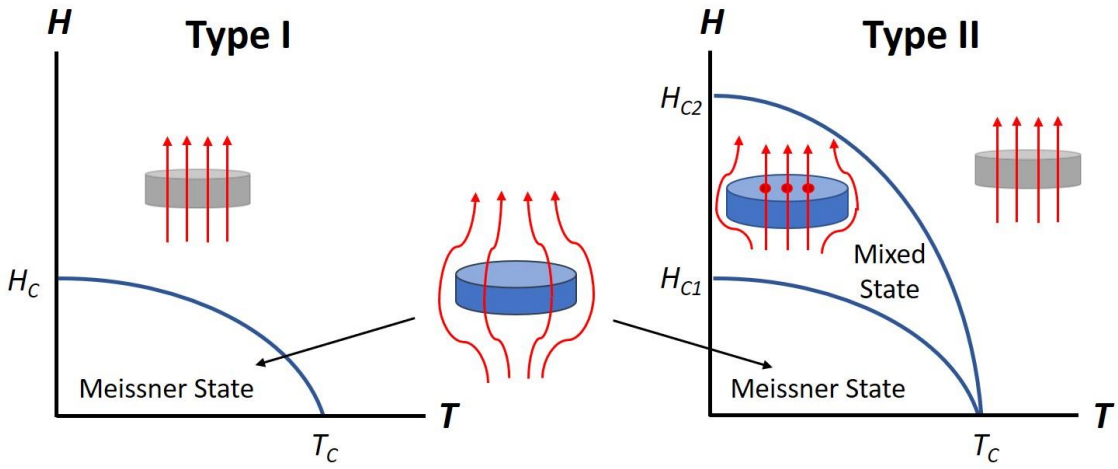

Figure 1.3 Schematic illustrations showing the magnetic behavior of type I and type II superconductors

The phenomenological approach for type I and type II superconductors are proposed by Ginzburg-Landau (GL) using the parameter called GL parameter also known as kappa; κ [7].

$$\kappa = \frac{\lambda_L}{\xi} \tag{1.1}$$

where, λ_L is a London penetration depth, and ξ is a coherence length. The superconductors are classified as type I when $\kappa < 1/\sqrt{2}$, and type II when $\kappa > 1/\sqrt{2}$. The magnitude of the

interfacial energy between the normal conducting and superconducting regions is reflected by GL parameter. When the surface energy is positive, these two regions tend to separate, while the surface energy is negative, these regions tend to mix due to the mixed state.

1.1.4 Coherence length (ξ)

One of the characteristic lengths for the description of average distance between the two electrons in a cooper pair is known as the coherence length (ξ). In the superconducting state, there is a minimum coherence length due to the relation of fermi velocity and energy gap of material associate with the condensation to the superconducting state [8].

$$\xi_0 = \frac{-2\hbar v_F}{\pi E_g} \tag{1.2}$$

where v_F is fermi velocity, E_g is superconducting band gap, and $\hbar$ is Planck's constant.

1.1.5 Penetration depth (λ)

The characteristic length associated with the decay of the magnetic field at the surface of a superconductor is known as the penetration depth, and the distance required for the magnetic field to fall to 1/e times the externally applied field. It depends on the number density of superconducting electrons [9]. We can estimate a value of λ by:

$$\lambda_L = \sqrt{\frac{\varepsilon_0 mc^2}{ne^2}} \tag{1.3}$$

where ε_0 is the electric constant, *m* is the mass of the charge carries, *c* is the velocity, *n* is superconducting electron density, and *e* is the magnitude of each carrier's charge.

1.1.6 Phenomenological theories

1.1.6 (a) London theory

One of the theoretical approaches to describe the superconducting state is the London equation [10]. London equation linked the electromagnetic fields with supercurrent flowing around a superconductor as:

$$E = \mu_0 \lambda_L^2 \frac{dJ_c}{dt} \tag{1.4}$$

$$B = -\mu_0 \lambda_L^2 \nabla x J_c \tag{1.5}$$

where, *E* is electric field, μ_0 is permeability in vacuum, J_c is critical current density, λ_L is the penetration depth, and *B* is applied magnetic field.

$$\nabla^2 B = \frac{B}{\lambda_L} \tag{1.6}$$

The eq.1.4 defines zero resistivity as the electric field accelerates the superconducting electrons and eq.1.5 and 1.6 shows that magnetic field impinging on a superconductor varies exponentially over a characteristic length scale λ_L.

1.1.6 (b) BCS theory

The theory developed by John Bardeen, Leon Cooper, and Robert Schrieffer (BCS) [6], explains the foundation of microscopic theory pertaining to electron-phonon coupling. The theory emphasized on the existence of attractive forces between conduction electrons at the Fermi surface, forming stable pairs with opposite wave vectors by overcoming the columbic repulsive force. The attractive force induced by crystal-lattice vibration (phonons) could keep the electrons in a pair called as Cooper pair. These pairs of electrons can condense into a state of zero electrical resistance [11].

1.2 Superconducting properties

1.2.1 Critical temperature (T_c)

The superconductor shows vanishing resistance and pronounces diamagnetic property below a critical temperature. This is an indicator of the physical properties of superconductors and normal conductors. In a superconductor, the resistivity drops to zero and the magnetic susceptibility shows negative value [12, 13].

1.2.2 Critical current density (J_c)

Critical current density (J_c) is the maximum steady current density that a superconductor can carry with zero resistance. This characteristic property is determined by flux pinning interactions by defects called pinning centers. Some examples of flux pinning centers are secondary phases in the matrix, grain boundaries, dislocations, stacking faults, etc. The critical current density can be determined from the magnetic measurement based on Bean's model [14, 15].

1.2.3 Trapped field (TF)

Type II superconductors contain the pinning centers which can trap magnetic flux by supercurrent circulating macroscopically within the bulk material. It can be predicted by the critical state model [14]. The super magnets may be activated by cooling in an applied magnetic field, called as field-cool activation (FC). They may also be activated by cooling them without an applied magnetic field and then applying a field after reaching stable cryo-temperature, called zero-field-cool activation (ZFC) [16]. The bulk superconductor can trap the magnetic field that is one order of magnitude stronger than the permanent magnet such as $Nd_2Fe_{14}B$ [17].

1.2.4 Flux pinning

Type II superconductor in the mixed state, has some of the magnetic flux lines in the form of individual flux vortices entering the non-superconducting phase when applying the magnetic field as shown in the Fig. 1.4. The interface energy between superconducting and non-superconducting regions is minimized in the mixed state. Each flux line carries a quantum of magnetic flux (ϕ_0):

$$\phi_0 = \frac{h}{e} \tag{1.7}$$

where *h* is Planck's constant and *e* is elementary charge [18, 19].

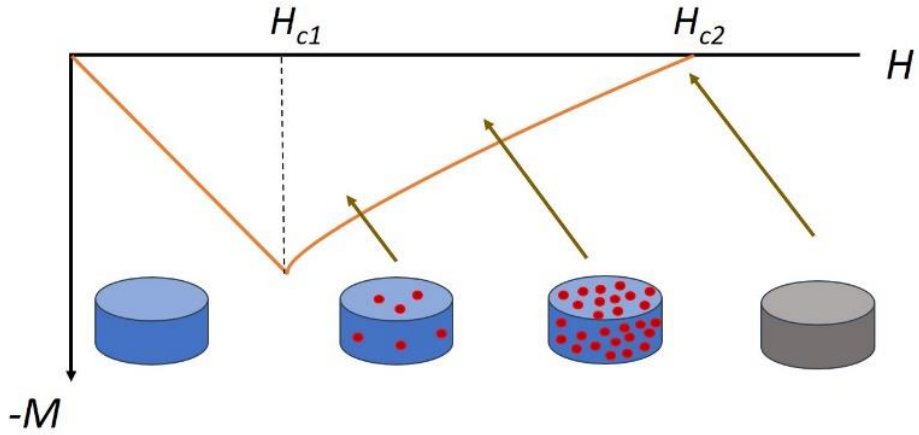

Figure 1.4 The magnetization and field cure showing fluxoids penetrating the superconductor

The flux line can move under the influence of Lorentz force (*F*) towards the direction to *j*-*B* plane as shown in Fig. 1.5 and *F* is given by

$$F = j\ x\ B \tag{1.8}$$

where j is current density and *B* is applied magnetic field.

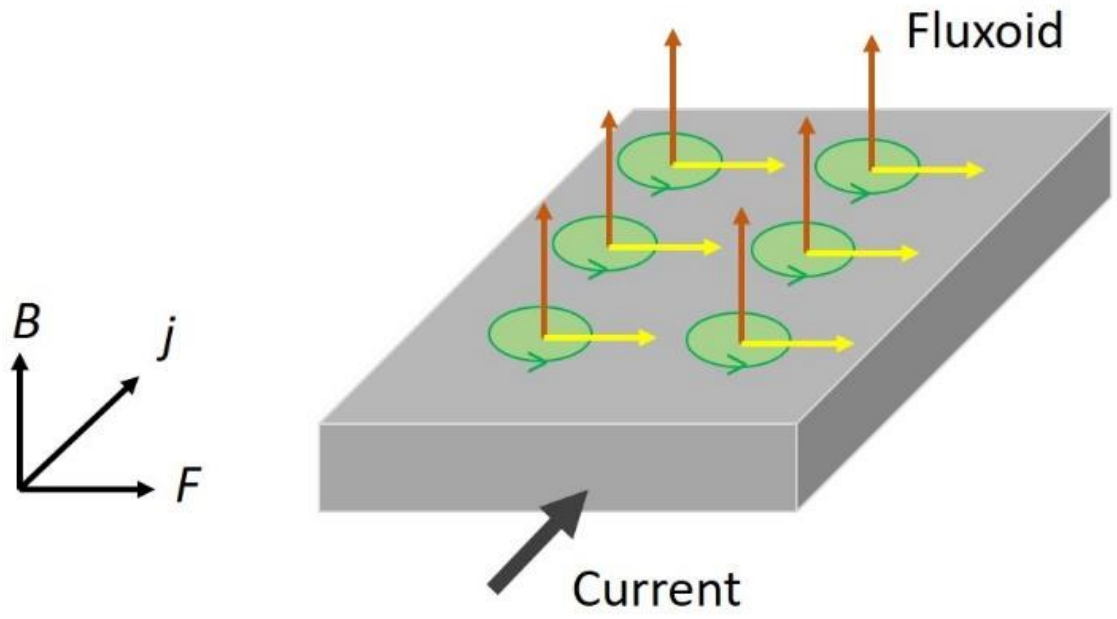

Figure 1.5 The Lorentz force acts on the fluxoids when the currents were passed in the mixed state of type II superconductor

The mixed state of type II superconductor, the non-superconducting phase prevents the flux motion and acts as pining centers. The effectiveness of flux pinning is generally associated with defects whose dimensions are close to ξ of the materials [20-23]. Some effective defects for flux pinning are oxygen defects [24], stacking faults [25, 26], dislocations [27, 28], twin boundaries [29], twin structures [30], and chemical fluctuations [31, 32] etc.

1.3 Applications

Since superconductors exhibit zero electrical resistivity, Meissner effect and Josephson junctions, they can be used in several applications in various fields [33]. The application of high temperature superconductors can be classified into three types:

(a) Wire and tape material for electrical power applications, for example, the underground transmission cables, and rotating machinery such as motors and generators used for the transportation of large currents [34, 35]

(b) Thin films for superconducting electronics and circuits [36, 37]

(c) Bulk materials for high trapped field superconducting magnets for levitation applications, bearing, flywheel, and permanent magnet application [38, 39].

1.4 Historical background of high temperature superconductors

In 1986, superconductivity in Nb_3Ge was discovered with transition temperature around 23.2 K [40], and $La_{1.85}Ba_{0.15}CuO_4$ was discovered by J.Georg Bednorz and K. Alex Muller that exhibited superconducting transition at 35 K [41]. In 1987, Paul C.W. Chu demonstrated the copper oxide based superconductor, $YBa_2Cu_3O_y$ (Y-123) had a critical temperature of 92 K which is above the liquid nitrogen at 77.3 K [42]. In 1988, high T_c oxide superconductors without a rare earth element such as; $Bi_2Sr_2Ca_1Cu_2O_8$ with T_c ~ 80 K [43] , $Bi_2Sr_2Ca_2Cu_3O_{10}$ with T_c ~ 110 K [44] , $Tl_2Ba_2Ca_2Cu_3O_{10}$ with T_c ~ 125 K [45], and $HgBa_2Ca_2Cu_3O_8$ with T_c ~ 134 K [46] were discovered. All high-temperature superconductors known at the present time were classified as type II superconductors. After discovering so many kinds of high temperature superconductors that have T_c higher than liquid Nitrogen temperature ~ 77.3 K, these materials are cheap and easy to operate.

1.4.1 Phase diagram

The RE-123 can be fabricated through the T_p, based on the peritectic reaction. The RE-123 heat above the T_p, resulting in decomposition of RE-123 into RE-211 reacts with Ba-Cu-O liquid. The sample is then slowly cooled then from RE-123 bulk superconductor, according to the following chemical reaction [47, 48]:

$$\text{RE-123 (S)} \rightleftharpoons \text{RE-211 (S)} + \text{Ba-Cu-O liquid (L)} \qquad (1.9)$$

For example, the reaction of Y-123 is illustrated by the pseudo-binary phase diagram as seen in Fig. 1.6 [49, 50]. A pseudo-binary phase diagram has been developed based on the solidification of different phases in the RE-123. The peritectic decomposition temperatures of different RE-123 compounds are summarized in table 1.1 [51].

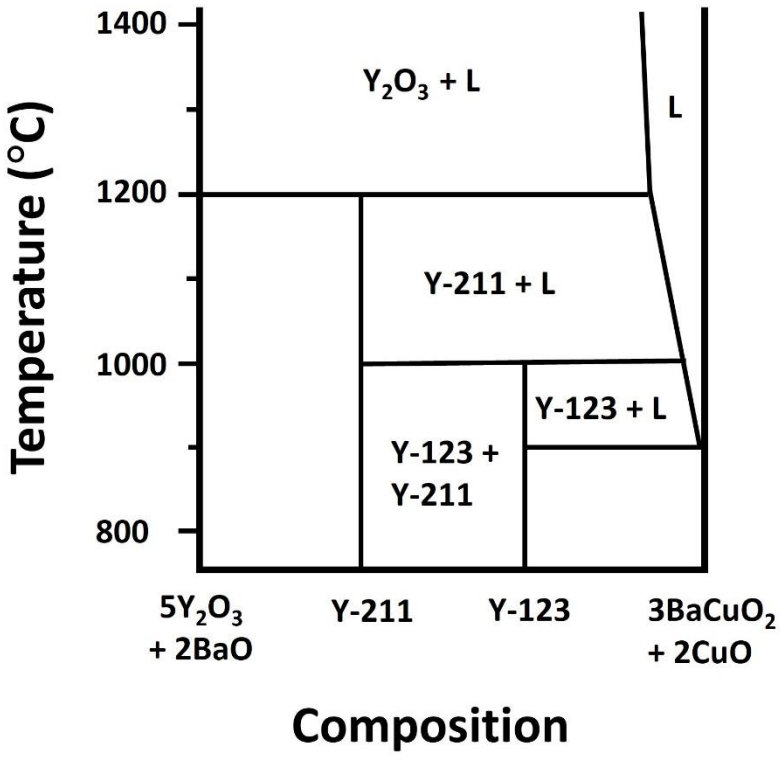

Figure 1.6 Pseudo-binary phase diagram for the Y-123 system [49, 50]

Table 1.1 Peritectic decomposition temperatures (T_P) of the various RE-123 superconductors

Peritectic temperature (°C), Error: ±5°C								
Nd	Sm	Eu	Gd	Dy	Y	Ho	Er	Yb
1068	1054	1046	1030	1010	1005	1005	990	960

1.4.2 Crystal structure

Most of the RE-123 superconductors family showed high T_c, layered crystallographic structure and they contain CuO planes (with the CuO_2 stoichiometry), normal to the [00*l*] direction that enable mobile charge of cooper pairs or electrons. For example, if we consider $YBa_2Cu_3O_y$ superconductor, its lattice structure is classified as a triple distorted perovskite formed by stacking two BaO planes with a layer of CuO chain in between two superconducting CuO_2 planes and a Y plane (see in fig. 1.7 (a)) [52]. The as-grown RE-123 bulks exhibit a tetragonal structure (oxygen-deficient & non-superconducting) which changes to an orthorhombic structure (oxygen sufficient & superconducting). The added O is positioned in the lattice such a way that it changes to an orthorhombic structure as seen in Fig.1.7 (b) and results in form of CuO chains. The oxygen content not only affects to the structure but affects to the magnetic and electrical properties. For example, in $YBa_2Cu_3O_y$ system, when the lattice has low oxygen content ($y \sim 6$: tetragonal structure) the material behaves as an insulator. Systematic change in lattice parameters in $YBa_2Cu_3O_y$ system, with increase in oxygen content is summarized in table 1.2 [53]. With slight increase in oxygen content such as $6 < y < 6.5$, the material's behavior changes to metallic. With further increase in oxygen content i.e. $y > 6.64$, the material starts exhibiting superconductivity and when $y = 7$ the material becomes a good superconductor with T_c = 93 K [54, 55], According, T_c changes with "y", since superconducting transition temperature is thought to be significantly dependent on the carrier concentration as shown in Fig 1.8 [33].

Table 1.2 Lattice parameters and unit cell volume of $YBa_2Cu_3O_y$ [53]

Sample composition	a (Å)	b (Å)	c (Å)	Volume (Å^3)
$YBa_2Cu_3O_7$	3.8154	3.8811	11.6701	172.8093
$YBa_2Cu_3O_{6.79}$	3.8252	3.8871	11.7162	174.2070
$YBa_2Cu_3O_{6.54}$	3.8323	3.8746	11.7311	174.1917
$YBa_2Cu_3O_{6.33}$	3.8396	3.8678	11.7576	174.6089

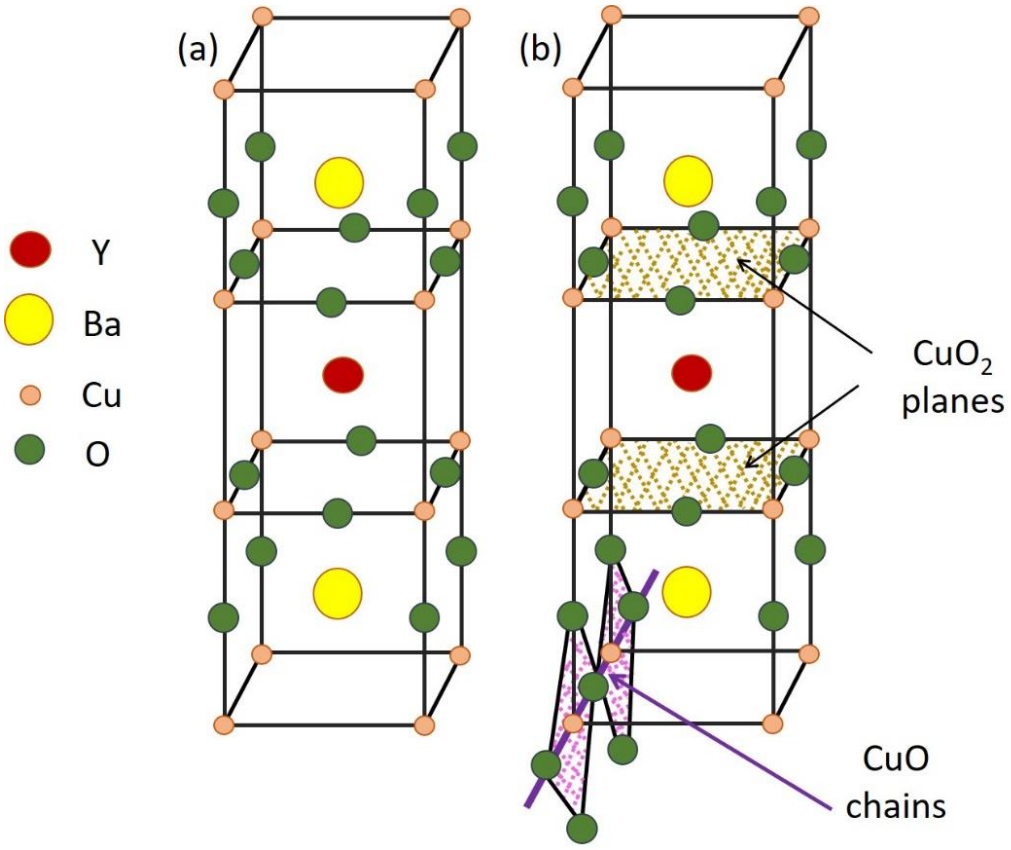

Figure 1.7 Crystal structure of Y-123 (a) a tetragonal structure, and (b) the CuO chains introduces an orthorhombic structure

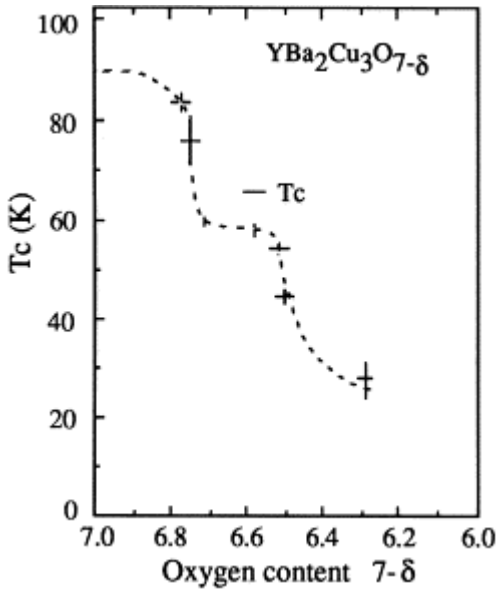

Figure 1.8 Dependence of T_c on oxygen content (y: $7-\delta$) in $YBa_2Cu_3O_y$ [33]

1.4.3 Processing

Various processes have been employed for the fabrication of oxide superconductors. The compound can be produced by solid-state reaction with a well-controlled heat process. However, J_c values are very small in the sintered bulk (5 A/cm^2 at 77 K, self-field), due to the grain boundary problem [15]. Jin S. et.al. [56] proposed the melt growth (MG) process to overcome those problems and achieves high J_c values. The fundamental melt growth process involves heating upto melting stage and slowly cooled in the special thermal gradient that was optimized based on the peritectic reaction. The bulk grown this way exhibited J_c of 17 kA/cm^2 at 77 K, self-field. The peritectic reaction of Y-123 (Y-123 (S) ⇌ Y-211 (S) + Ba-Cu-O (L)) at T_p ~ 1000°C, and the schematic illustration of the MG process are shown in Fig. 1.9.

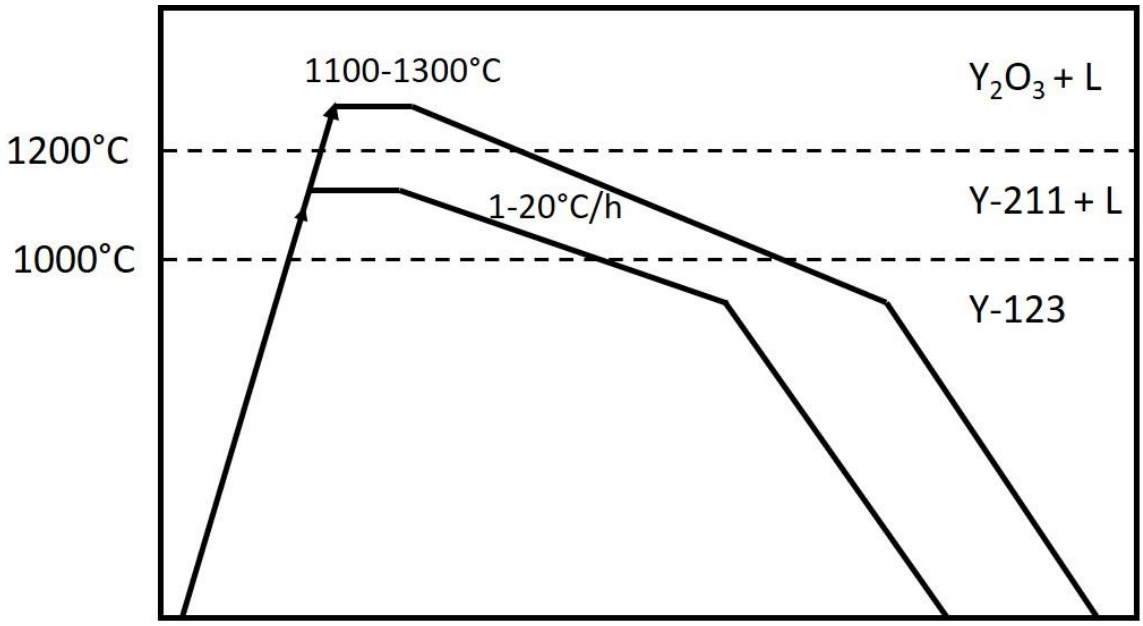

Figure 1.9 Schematic illustration of MG process [15]

Later several other techniques based on MG were devised such as modified melt growth [57, 58], quench and melt growth (QMG) [59], melt powder melt growth (MPMG) [60], powder melting (PMP) [61], oxygen-controlled melt growth (OCMG) [62, 63], top-seeded melt growth (TSMG) [64, 65] , buffer-aided top-seeded melt growth (BA-TSMG) [66, 67], and infiltration growth (IG) [68-70]. These general processes involve the textured growth of the RE-123 phase from the peritectic reaction.

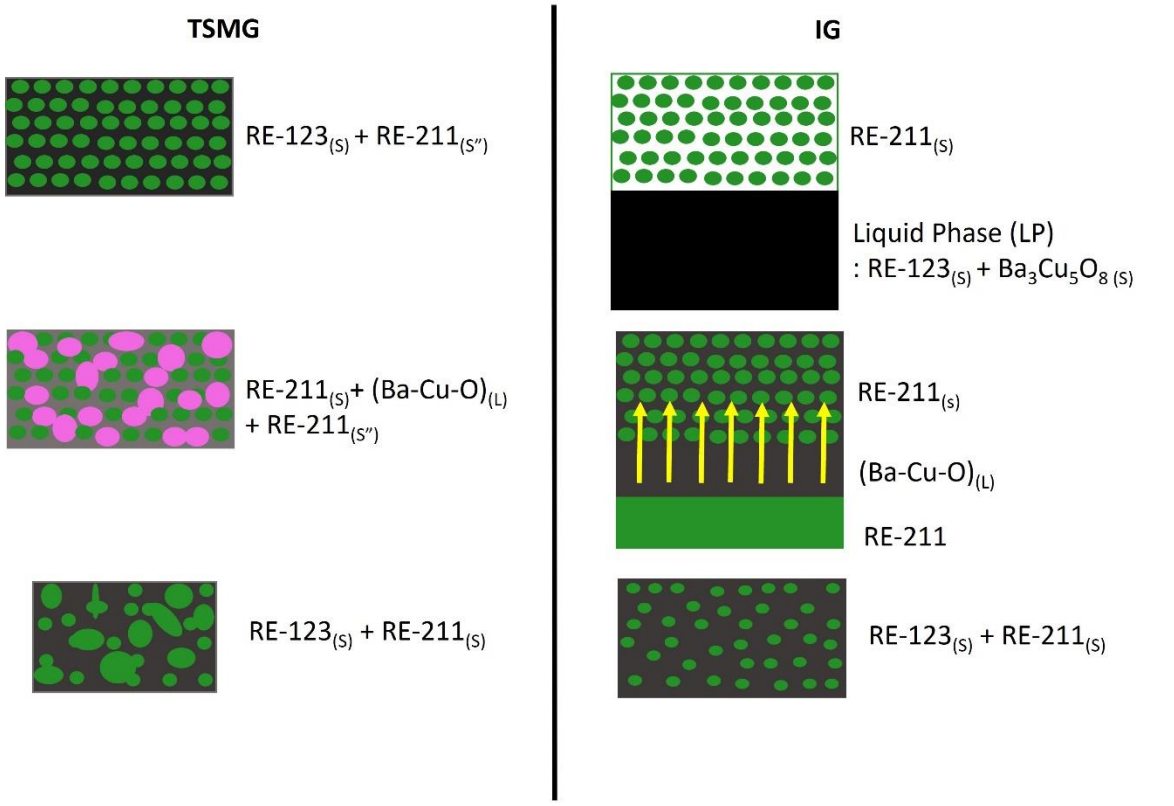

Figure 1.10 Comparison between TSMG and IG process for bulk RE-123 superconductor

Nowadays, the fabrication techniques often used to produce large single grain RE-123 are TSMG and IG process that are superior compared to sintering. The comparison of TSMG and IG processes for fabricating RE-123 superconductor along with resulting final microstructure are presented as a schematic diagram shown in Fig. 1.10. The TSMG process starts with a preform pellet of RE-123 or RE-123 + RE-211 phase whereas the IG process starts with RE-211 pellet and liquid phase (LP) pellet. The preforms of both TSMG and IG processes will be heated to a temperature above peritectic temperature. While the mixture in TSMG will follow the peritectic reaction and result in RE-123 formation. On the other hand, in the IG case, RE-123 is formed via reaction between infiltrated Ba-Cu-O liquid and RE-211 pellet at a temperature close to the peritectic temperature [70, 71].

1.4.4 Seeding techniques

To promote heterogeneous grain nucleation and single grain growth in TSMG and IG process, a seed crystal is used to control and overcome the multi-nucleation. The RE-123 grows in accordance with the lattice orientation of seed. A seed selected should be a perfect single crystal with a similar crystal structure and a higher melting temperature than RE-123 preform to ensure phase stability during the fabrication process [71, 72]. Single crystal such as Nd-123 (T_p ~1080°C) [73, 74], Sm-123 (T_p ~1100°C) [75, 76], and Nd-123/MgO thin film (T_p ~1200°C) [77, 78] serves as an effective seed for RE-123 single grain growth. Usually, a crystal cleaved from big bulk with perfect *a/b* crystallographic plane is chosen as seed and is placed on the top sample surface. If the seed is used from the beginning of heat cycle at room temperature i.e. before the melt process is started, then it is called as cold seeding [79, 80]. However, if the seed is placed on the preform when the reaction temperature reaches higher than T_p during melt process it is referred as hot seeding [74, 78] as shown in Fig. 1.11 (a). During the process, the RE-211 and liquid are in the contact with the (001) surface of the seed and on the (100)/(001) surfaces at the border of the crystal seed then crated a sympathetic nucleation. Then subsequently a facet development and continuous growth process. The as-growth sample generally grow in a parallelepipedal form with (001), (010) and (001) crystal planes (see Fig. 10(b) and (c)) that a five-domain different growth sectors can be grown. The domains are usually separated by boundaries [81].

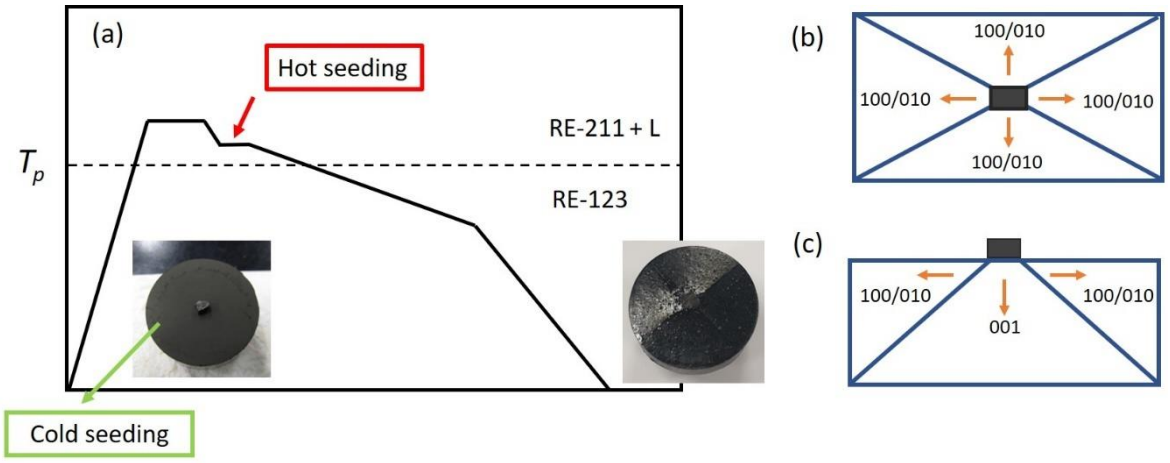

Figure 1.11 (a) Schematic illustration of cold and hot seeding techniques, and top surface of (Gd,Y,Er)-123 sample single from which can be seen growth lines from the seed, and schematic of five-domain morphology (b) in the (001) plane and (c) along the (001) direction.

1.5 Research objectives

Due to the superior superconducting properties of the bulk RE-123 superconductors, the material shows potential for the various applications and attained great excitement and interest from researchers. Especially, the large single grain bulk RE-123 superconductors have considerable potential for trapping magnetic field higher than the permanent magnets (by over 100 times) [82]. However, the fabrication processes are complicated and have significantly hindered the development of batch production. Many processing parameters, such as the suitable temperature profile, appropriate RE element, the homogeneity of powders, the furnace, and the precursor powders, etc., must be optimized. The key factor of the superconducting properties is the microstructure, which can be controlled via optimizing fabrication process to improve flux pinning. Thus, the objectives of this study are as follows:

- To control the microstructure by using small RE-211 in the precursor, we proposed a technique that uses high-power ultra-sonic waves to control and refine the secondary particles. This ultra-sonication technique to refine Y-211 secondary phase particles provide improvement with cost-efficiency and less contamination.

- In order to improve the flux pinning by using ternary bulk RE-123 system, it is essential to explore the new ternary bulk RE-123 (RE: Gd, Y, Er) and enhance critical current density (J_c) as well as trapped field performance.

References

1. Onnes, K., *Leiden Comm.* 1911. **120b, 122b, 124c**
2. Ramakrishnan, D. *Superconductivity of Mercury*. 2016 21 January [cited 2021 15 Febuary]; Available from: https://infofavour.blogspot.com/2016/01/short-note-on-superconductivity-and.html.
3. John K. Hulm, J. Eugene Kunzler, and B.T. Matthias, *The road to superconducting materials.* Physics Today, 1981. **34**.
4. Meissner, W. and R. Ochsenfeld, *Naturwissenschaften.* Naturwissenschaften, 1933. **21**(44): p. 787-788.
5. Rose-Innes, A.C. and E.H. Rhoderick, *Introduction to Superconductivity.* American Journal of Physics, 1970. **38**(8): p. 1048-1049.
6. Bardeen, J., L.N. Cooper, and J.R. Schrieffer, *Theory of superconductivity.* Physical review, 1957. **108**(5): p. 1175.
7. Milošević, M.V. and R. Geurts, *The Ginzburg–Landau theory in application.* Physica C: Superconductivity, 2010. **470**(19): p. 791-795.
8. Kittel, C., P. McEuen, and P. McEuen, *Introduction to solid state physics*. Vol. 8. 1996: Wiley New York.
9. Owens, F., *Dc and ac magnetic field dependence of electromagnetic absorption in HgPbBaCaCuO, 133 K, superconductor.* Journal of Physics and Chemistry of Solids, 1997. **58**(9): p. 1481-1486.
10. London, F. and H. London, *The electromagnetic equations of the supraconductor.* Proceedings of the Royal Society of London. Series A-Mathematical and Physical Sciences, 1935. **149**(866): p. 71-88.
11. Cooper, L.N., *Bound Electron Pairs in a Degenerate Fermi Gas.* Physical Review, 1956. **104**(4): p. 1189-1190.
12. Shrivastava, S.K., *Measurement Methods for Determination of Transition Temperature of High-T_c*. 2018.
13. Takizawa, T., M. Murakami, and M. Saito, *Critical Currents in Superconductors.* Default journal, 2005.

14. Bean, C.P., *Magnetization of High-Field Superconductors.* Reviews of Modern Physics, 1964. **36**(1): p. 31-39.
15. Murakami, M., *Melt Processed High-Temperature Superconductors*. Melt Processed High-Temperature Superconductors. 1992.
16. Weinstein, R., et al., *A significant advantage for trapped field magnet applications—A failure of the critical state model.* Applied Physics Letters, 2015. **107**(15): p. 152601.
17. Müller, K.-H., et al., *New permanent magnets.* Journal of Magnetism and magnetic materials, 2001. **226**: p. 1370-1376.
18. Peres, A., *Quantum limitations on measurement of magnetic flux.* Physical review letters, 1988. **61**(18): p. 2019.
19. Coskun, U.C., et al., *h/e magnetic flux modulation of the energy gap in nanotube quantum dots.* Science, 2004. **304**(5674): p. 1132-1134.
20. Koch, R.H., et al., *Experimental evidence for vortex-glass superconductivity in Y-Ba-Cu-O.* Physical Review Letters, 1989. **63**(14): p. 1511-1514.
21. Wright, A., T. Xia, and A. Erbil, *Phase-slip mechanism for dissipation in high-T_c superconductors.* Physical Review B, 1992. **45**(10): p. 5607.
22. Matsumoto, K. and P. Mele, *Artificial pinning center technology to enhance vortex pinning in YBCO coated conductors.* Superconductor Science and Technology, 2009. **23**(1): p. 014001.
23. Wright, A., K. Zhang, and A. Erbil, *Dissipation mechanism in a high-T_c granular superconductor: Applicability of a phase-slip model.* Physical Review B, 1991. **44**(2): p. 863.
24. Tarascon, J.-M., et al., *Superconductivity at 40 K in the oxygen-defect perovskites $La_{2-x}Sr_xCuO_{4-y}$.* Science, 1987. **235**(4794): p. 1373-1376.
25. Phelan, W.A., et al., *Stacking variants and superconductivity in the Bi–O–S system.* Journal of the American Chemical Society, 2013. **135**(14): p. 5372-5374.
26. Roessli, B., et al., *Combined Electronic-Nuclear Magnetic Ordering of the Ho^{3+} Ions and Magnetic Stacking Faults in the High-T_c Superconductor $HoBa_2Cu_3O_7$.* EPL (Europhysics Letters), 1993. **23**(7): p. 511.

27. Nakahara, S., et al., *Analysis of dislocations in Y-Ba-Cu-O superconductors.* Applied physics letters, 1989. **54**(19): p. 1926-1928.
28. Salama, K. and D.F. Lee, *Progress in melt texturing of $YBa_2Cu_3O_x$ superconductor.* Superconductor Science and Technology, 1994. **7**(4): p. 177.
29. Vinnikov, L.Y., et al., *Direct observation of the lattice of Abrikosov vortices in high-T_c superconductor $YBa_2Cu_3O_x$ single crystals.* Solid state communications, 1988. **67**(4): p. 421-423.
30. Muralidhar, M., et al., *Microstructure of (Nd,Eu,Gd)-123 matrix with (Nd,Eu,Gd)-211 inclusions.* Journal of Materials Research, 2001. **16**(2): p. 407-412.
31. Setoyama, Y., et al., *Systematic change of flux pinning in (Dy,RE)123 and (Y,RE)123 melt-solidified bulks with unit cell orthorhombicity.* Superconductor Science and Technology, 2014. **28**(1): p. 015014.
32. Shi, Y., et al., *The growth and superconducting properties of RE–Ba–Cu–O single grains with combined RE elements (RE = Gd and Y).* Superconductor Science and Technology, 2020. **33**(3): p. 035003.
33. Shiohara, Y. and A. Endo, *Crystal growth of bulk high-T_c superconducting oxide materials.* Materials Science and Engineering: R: Reports, 1997. **19**(1-2): p. 1-86.
34. Kang, S., et al., *High-performance high-T_c superconducting wires.* Science, 2006. **311**(5769): p. 1911-1914.
35. Miki, M., et al., *Development of a synchronous motor with Gd–Ba–Cu–O bulk superconductors as pole-field magnets for propulsion system.* Superconductor Science and Technology, 2006. **19**(7): p. S494-S499.
36. Zeng, X., et al., *In situ epitaxial MgB_2 thin films for superconducting electronics.* Nature Materials, 2002. **1**(1): p. 35-38.
37. Rowell, J., *Superior thin films.* Nature Materials, 2002. **1**(1): p. 5-6.
38. Nakagawa, K., et al., *Study on Magnetic Drug Delivery System Using HTS Bulk Magnet.* IEEE Transactions on Applied Superconductivity, 2012. **22**(3): p. 4903804-4903804.
39. Nakamura, T., et al., *Development of a superconducting bulk magnet for NMR and MRI.* Journal of Magnetic Resonance, 2015. **259**: p. 68-75.

40. Gavaler, J., M. Janocko, and C. Jones, *The Preparation of Thin Films of B-1 Structure Superconducting Ternary Compounds.* Journal of Vacuum Science and Technology, 1973. **10**(1): p. 17-19.
41. Bednorz, J.G. and K.A. Müller, *Possible high T_c superconductivity in the Ba−La−Cu−O system.* Zeitschrift für Physik B Condensed Matter, 1986. **64**(2): p. 189-193.
42. Wu, M.-K., et al., *Superconductivity at 93 K in a new mixed-phase Y-Ba-Cu-O compound system at ambient pressure.* Physical review letters, 1987. **58**(9): p. 908.
43. Bordet, P., et al., *A note on the symmetry and Bi valence of the superconductor $Bi_2Sr_2Ca_1Cu_2O_8$.* Physica C: Superconductivity, 1988. **156**(1): p. 189-192.
44. Matsubara, I., et al., *Superconducting whiskers and crystals of the high T_c $Bi_2Sr_2Ca_2Cu_3O_{10}$ phase.* Applied physics letters, 1991. **58**(4): p. 409-411.
45. Sheng, Z.Z. and A.M. Hermann, *Superconductivity in the rare-earth-free Tl–Ba–Cu–O system above liquid-nitrogen temperature.* Nature, 1988. **332**(6159): p. 55-58.
46. Schilling, A., et al., *Physical properties of $HgBa_2Ca_2Cu_3O_8$ with $Tc \approx 133K$.* Physica C: Superconductivity, 1994. **235-240**: p. 229-232.
47. Scheel, H.J. and F. Licci, *Phase diagrams and crystal growth of oxide superconductors.* Thermochimica Acta, 1991. **174**: p. 115-130.
48. Krabbes, G., et al., *Improved HTSC bulk materials: a thermodynamic approach to processing.* Superconductor Science and Technology, 1998. **11**(1): p. 144-148.
49. Aselage, T. and K. Keefer, *Liquidus relations in Y–Ba–Cu oxides.* Journal of Materials Research, 1988. **3**(6): p. 1279-1291.
50. Desgardin, G., I. Monot, and B. Raveau, *Texturing of high-T_c superconductors.* Superconductor Science and Technology, 1999. **12**(7): p. R115-R133.
51. Cardwell, D.A. and N. Hari Babu, *Processing and properties of single grain (RE)–Ba–Cu–O bulk superconductors.* Physica C: Superconductivity and its Applications, 2006. **445-448**: p. 1-7.
52. Jorgensen, J.D., et al., *Oxygen ordering and the orthorhombic-to-tetragonal phase transition in $YBa_2Cu_3O_{7-x}$.* Physical Review B, 1987. **36**(7): p. 3608-3616.
53. Howe, B.A., *Crystal structure and superconductivity of $YBa_2Cu_3O_{7-x}$.* 2014.

54. Suyama, Y., et al. *Effect of Oxygen Deficiency on the Superconducting Properties of YBCO*. 1991. Tokyo: Springer Japan.
55. Manthiram, A., et al., *The influence of oxygen variation on the crystal structure and phase composition of the superconductor yttrium barium copper oxide ($YBa_2Cu_3O_{7-x}$).* Journal of the American Chemical Society, 1987. **109**(22): p. 6667-6669.
56. Jin, S., et al., *High critical currents in Y-Ba-Cu-O superconductors.* Applied physics letters, 1988. **52**(24): p. 2074-2076.
57. Salama, K., et al., *High current density in bulk $YBa_2Cu_3O_x$ superconductor.* Applied Physics Letters, 1989. **54**(23): p. 2352-2354.
58. Hojaji, H., et al., *A comparative study of sintered and melt-grown recrystallized $YBa_2Cu_3O_x$.* Journal of Materials Research, 1989. **4**(1): p. 28-32.
59. Morita, M., et al., *Quench and melt growth (QMG) process for large bulk superconductor fabrication*, in *Advances in superconductivity III*. 1991, Springer. p. 733-736.
60. Fujimoto, H., et al., *Melt processing of YBaCuO oxide superconductors*, in *Advances in Superconductivity II*. 1990, Springer. p. 285-288.
61. Lian, Z., et al., *The properties of YBCO superconductors prepared by a new approach: the'powder melting process'.* Superconductor Science and Technology, 1990. **3**(10): p. 490.
62. Muralidhar, M., et al., *Application of oxygen controlled melt growth (OCMG) in ternary RE123 systems.* Physica C: Superconductivity, 1997. **282**: p. 503-504.
63. Diko, P., H. Kojo, and M. Murakami, *Microstructure of NdBaCuO superconductors prepared by the oxygen-controlled-melt-growth method.* Physica C: Superconductivity, 1997. **276**(3-4): p. 185-196.
64. Kim, C.-J., et al., *Microstructure, microhardness, and superconductivity of CeO_2-added Y–Ba–Cu–O superconductors.* Journal of materials research, 1992. **7**(9): p. 2349-2354.
65. Nariki, S., et al., *High critical current density in RE–Ba–Cu–O bulk superconductors with very fine RE_2BaCuO_5 particles.* Physica C: Superconductivity, 2004. **412-414**: p. 557-565.

66. Devendra Kumar, N., et al., *Buffer Pellets for High-Yield, Top-Seeded Melt Growth of Large Grain Y–Ba–Cu–O Superconductors.* Crystal Growth & Design, 2015. **15**(3): p. 1472-1480.
67. Namburi, D.K., et al., *Control of Y-211 content in bulk YBCO superconductors fabricated by a buffer-aided, top seeded infiltration and growth melt process.* Superconductor Science and Technology, 2016. **29**(3): p. 034007.
68. Viswanath, N., et al., *Infiltration-growth processing of superconductor.* Superconductor Science and Technology, 1998. **11**(4): p. 420.
69. Muralidhar, M., et al., *Microstructure, critical current density and trapped field experiments in IG-processed Y-123.* Superconductor Science and Technology, 2016. **29**(5): p. 054003.
70. Reddy, E.S. and T. Rajasekharan, *Shape Forming Simultaneous with J_c Enhancement in $REBa_2Cu_3O_7$ Superconductors.* Journal of Materials Research, 1998. **13**(9): p. 2472-2475.
71. Cloots, R., et al., *From RE-211 to RE-123. How to control the final microstructure of superconducting single-domains.* Superconductor Science and Technology, 2004. **18**(3): p. R9-R23.
72. Leblond, C., et al., *Optimization of the texture formation and characterization of large size top-seeded-melt-grown YBCO pellets.* Physica C: Superconductivity, 1999. **311**(3): p. 211-222.
73. Nariki, S., et al., *Effect of Ag addition on cold-seeded melt-growth of Gd–Ba–Cu–O superconductor using Nd123 seed crystal.* Physica C: Superconductivity, 2003. **392**: p. 468-472.
74. Chauhan, H.S. and M. Murakami, *Hot seeding for the growth of c-axis-oriented Nd-Ba-Cu-O.* Superconductor Science and Technology, 2000. **13**(6): p. 672-675.
75. Bierlich, J., et al., *Growth and investigation of melt-textured SmBCO in air for preparation of Sm123 seed crystals.* Superconductor Science and Technology, 2005. **18**(2): p. S194-S197.
76. Jee, Y.A., et al., *Effect of resolidification nature of $SmBa_2Cu_3O_{7-y}$ seeds on the growth mode of $YBa_2Cu_3O_{7-y}$.* Physica C: Superconductivity, 1999. **314**(3-4): p. 211-218.

77. Cai, C. and H. Fujimoto, *Effects of Nd123/MgO thin film and MgO single-crystal seeds in isothermal solidification of YBaCuO/Ag.* Journal of Materials Research, 2000. **15**(8): p. 1742-1748.
78. Cardwell, D.A., et al., *Fabrication of large grain Nd-Ba-Cu-O by seeded melt growth.* Physica C: Superconductivity, 2000. **341-348**: p. 2297-2300.
79. Iida, K., et al., *Seeded infiltration and growth of single-domain Gd–Ba–Cu–O bulk superconductors using a generic seed crystal.* Superconductor Science and Technology, 2006. **19**(7): p. S478.
80. Muralidhar, M., et al., *Novel seed for batch cold seeding production of GdBaCuO bulks.* Physica C: Superconductivity and its applications, 2010. **470**(20): p. 1158-1163.
81. Delamare, M.P., et al., *Macrosegregation of Y_2BaCuO_5 particles in top-seeded melt textured monoliths.* Physica C: Superconductivity, 1999. **323**(3): p. 107-114.
82. Tomita, M. and M. Murakami, *High-temperature superconductor bulk magnets that can trap magnetic fields of over 17 tesla at 29 K.* Nature, 2003. **421**(6922): p. 517-520.

Chapter 2

Experimental Details

In this chapter, I have explained the synthesizing process for REBCO bulk superconductors and techniques used to investigate the superconducting performances. Preparation of precursors such as $REBa_2Cu_3O_y$ (RE: Gd, Y, Er) "RE-123", RE_2BaCuO_5 (Re: Gd, Y, Er) "RE-211" and Liquid Phase ($Ba_3Gu_5O_8$) "LP" powders for fabrication of bulk Y-123/(Gd,Y,Er)-123 superconductors were presented. Phase purity and chemical composition of those powders was examined. Details of Top Seeded Melt growth (TSMG) and Infiltration Growth IG) process used in the experiment as well as the importance of oxygen annealing process are explained. RE-211 secondary phase refinement techniques such as chemical doping and mechanical refinement were employed in the process. Finally, characterization techniques used to obtain particle size, microstructural and superconducting properties were discussed.

2.1 Synthesis

2.1.1 Powders preparation

This type II superconductor consists of superconducting phase (RE-123) and dispersed non-superconducting phase (RE-211). Hence, it is required to arrange or prepared both RE-123 and RE-211 powders along with liquid phase prior to experiment. There are two ways to go about this, one is to purchase commercial powders and the other is to synthesize the powder (self-made) from raw oxide powders such as RE_2O_3, BaO_2, and CuO. The commercial powders can be expensive as one can chose the purity and particle size. On the other hand, the self-made powders were synthesized by solid state reaction via calcination process of the initial raw oxide powders [1, 2]. The raw powders were mixed in stoichiometric ratio to obtain the $REBa_2Cu_3O_7$ (RE: Gd, Y, Er), RE_2BaCuO_5 (RE: Gd, Y, Er), and $Ba_3Cu_5O_8$ compositions as show below.

For $REBa_2Cu_3O_7$ powder:

$$0.5RE_2O_3 + 2BaO_2 + 3CuO \rightarrow REBa_2Cu_3O_7 + 0.75O_2 \quad (2.1)$$

For RE_2BaCuO_5 powder:

$$RE_2O_3 + BaO_2 + CuO \rightarrow RE_2BaCuO_5 + 0.5O_2 \quad (2.2)$$

For $Ba_3Cu_5O_8$ (“liquid” phase, L)

$$3BaO_2 + 5CuO \rightarrow Ba_3Cu_5O_8 + 1.5O_2 \quad (2.3)$$

The raw oxide powders were mixed in an alumina mortar using a pestle for 1 hours. The mixed powders were heated up to maximum temperature (T_m) at a heating rate of 100°C/h, held at T_m for 12 hours and then cooled to room temperature at cooling rate of -100°C/h as shown in Fig. 2.1. The maximum temperature was ranged between 800-940°C and several calcinations very done to ensure complete single-phase formation. In case of, RE-123 powder calcinations were carried at 860, 880, 900, and 920°C for 12 hours each. RE-211 powder was calcined at 820, 840, 860, and 880°C, while liquid phase

was calcined at 840 and 860°C (12 hours each). After every calcination, the powder was grinded for 2 h before next calcination process.

After first calcination, the color of mixed powders will turn into black color (for RE-123 and LP) and dark green color (for RE-211 powder). After completing single-phase formation, the RE-123 powder turns into complete black color, the RE-211 powder changes into light green color and liquid phase powder turn into black color. Systematic change in color of Y-123, Y-211 and $Ba_3Cu_5O_8$ powders with each calcination were as shown in Figs. 2.2 – 2.4, respectively.

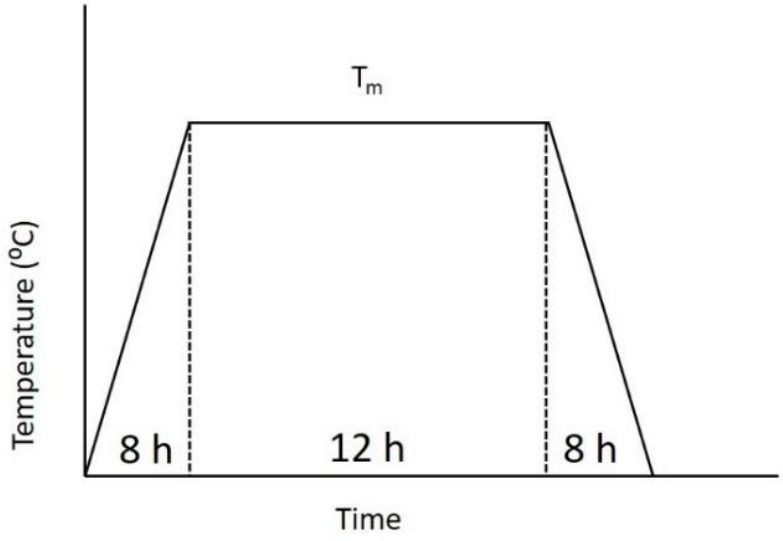

Figure 2.1 Temperature profile for calcination of RE-123, RE-211, and LP powders

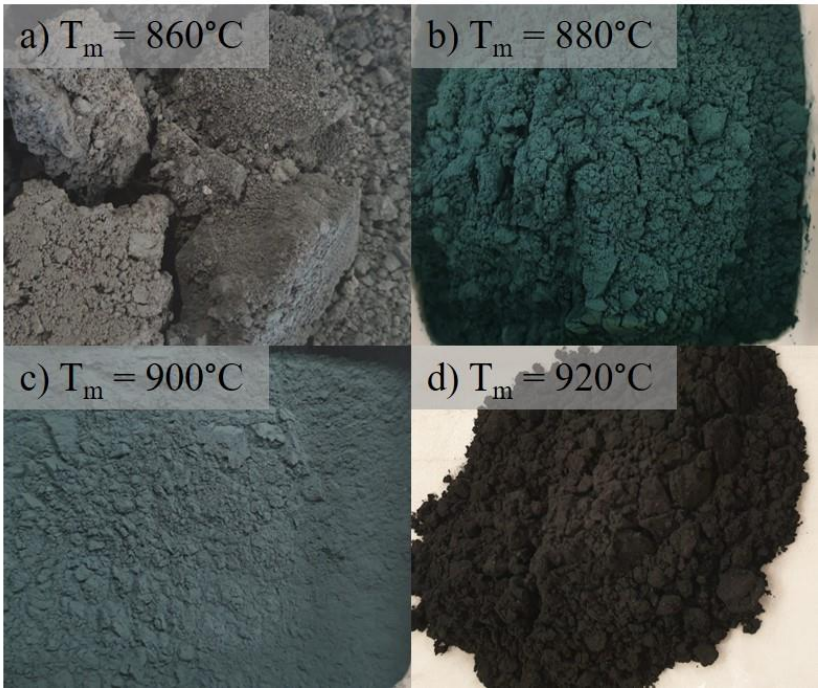

Figure 2.2 Y-123 powder after calcination at (a) 860°C, (b) 880°C, (c) 900°C, and (d) 920°C

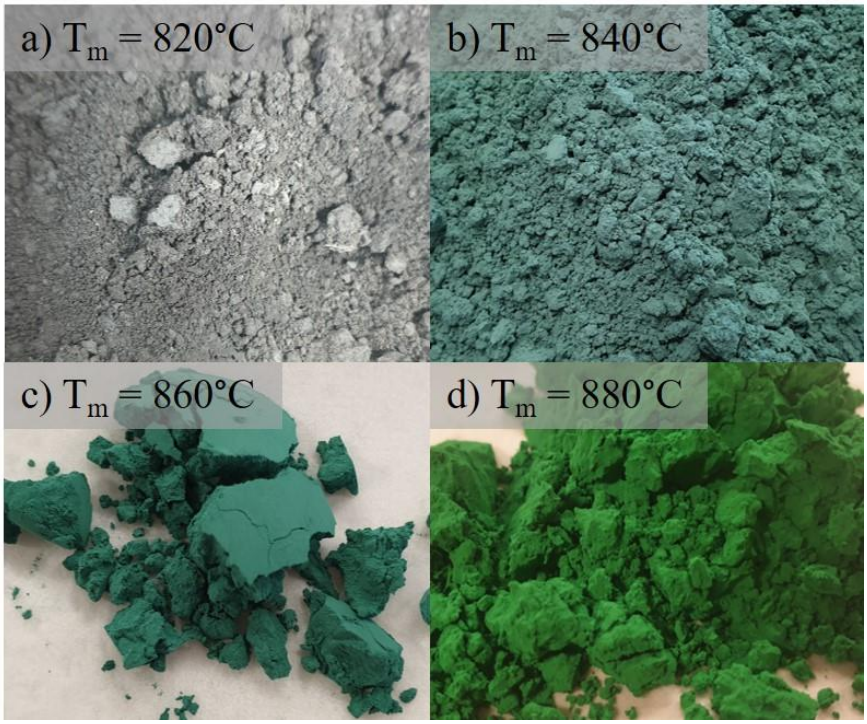

Figure 2.3 Y-211 powder after calcination at (a) 820°C, (b) 840°C, (c) 860°C, and (d) 880°C

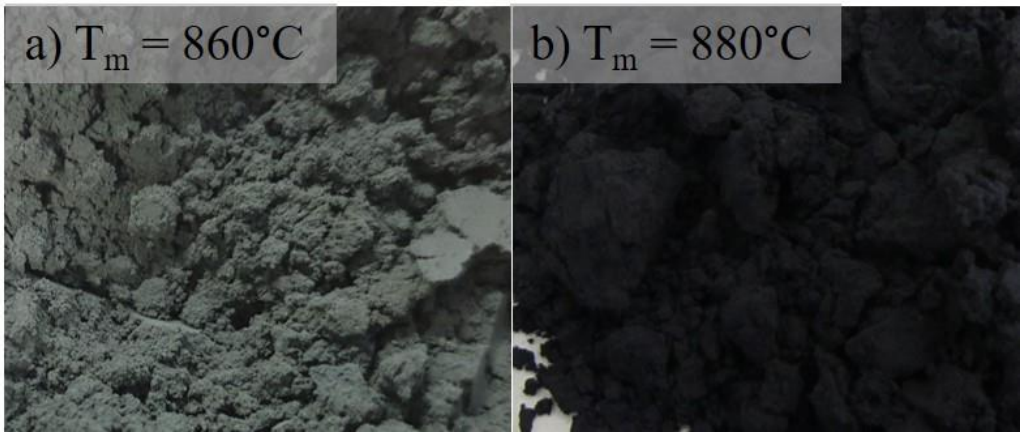

Figure 2.4 $Ba_3Cu_5O_8$ powder after calcination at (a) 860°C, and (b) 880°C

Visual evidence such as the color of powders, can be checked to keep track of each calcination process. Further, to confirm the phase purity of Y-123, Y-211 and $Ba_3Cu_5O_8$, the powders have been characterized by X-Ray Diffractometer (XRD) with CuKα radiation. The XRD results of Y-123 and Y-211 powder are shown in Figs. 2.5 and 2.6, respectively that are indexed with standard reference patterns i.e. powder diffraction file (PDF) no.01-085-1607 and 01-079-0697, respectively. Fig. 2.5(a) show the XRD result with the gray color of Y-123 powder that reflects incomplete formation of single-phase Y-123 powder. The diffraction peaks corresponding to Y_2O_3, BaO_2 and CuO phases appear in the XRD pattern, which clearly indicates the need to increase the number of calcination steps as well as calcination temperature. The process is repeated until the powder becomes to single phase Y-123 (see Fig. 2.5(b)). Similar process was adapted to produce the Y-211 powder. The third calcination at T_m = 860°C resulted in dark green color and the result was not in match with the standard pattern as shown in the Fig. 2.6(a). Hence in the fourth calcination we increased T_m to 880°C for 12 hours. The complete calcined Y-211 powder showed light green color and the XRD results are presented in Fig. 2.6 (b). Note that the diffraction data matches well with JSPDS file no. 01-085-1607 and 01-079-0697.

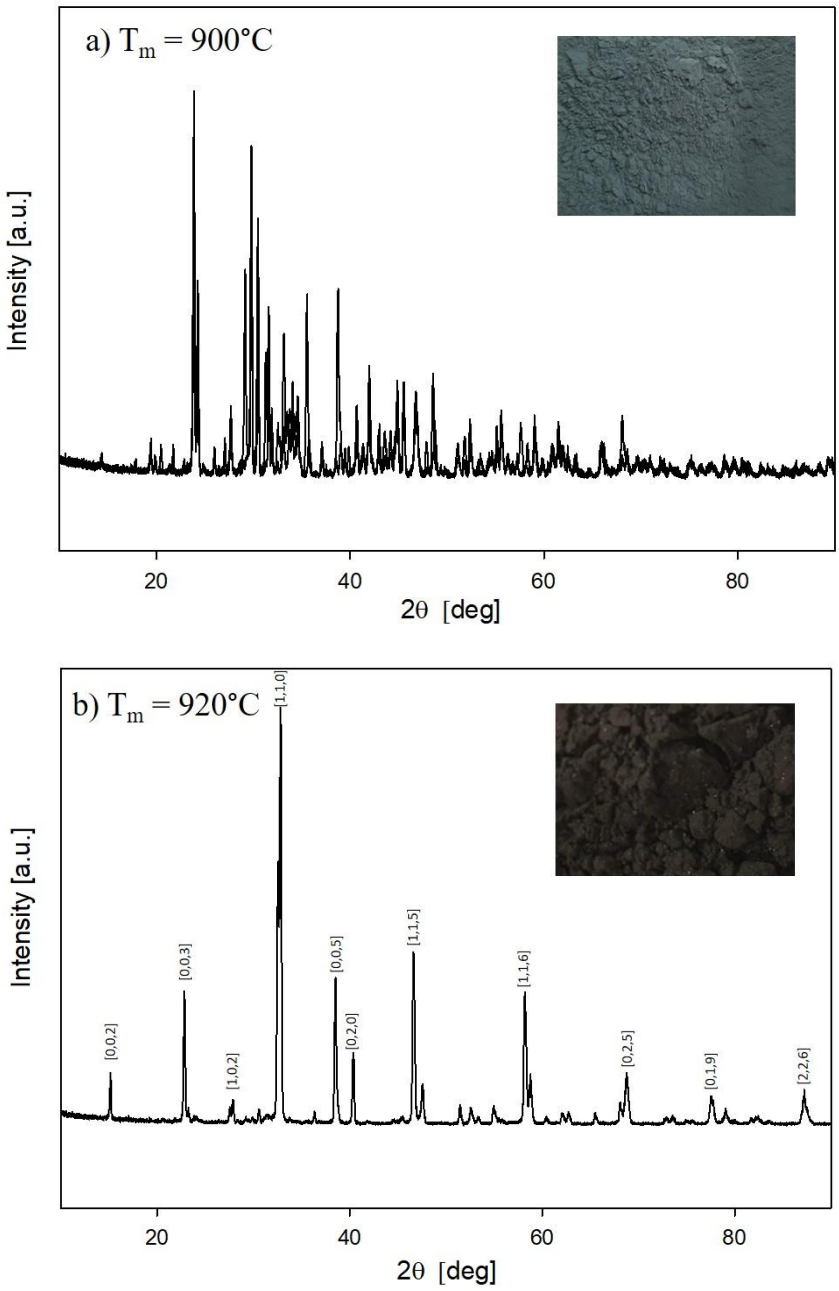

Figure 2.5 XRD result of calcined Y-123 powder; (a) third calcination at T_m = 900°C, and (b) fourth calcination at T_m = 920°C

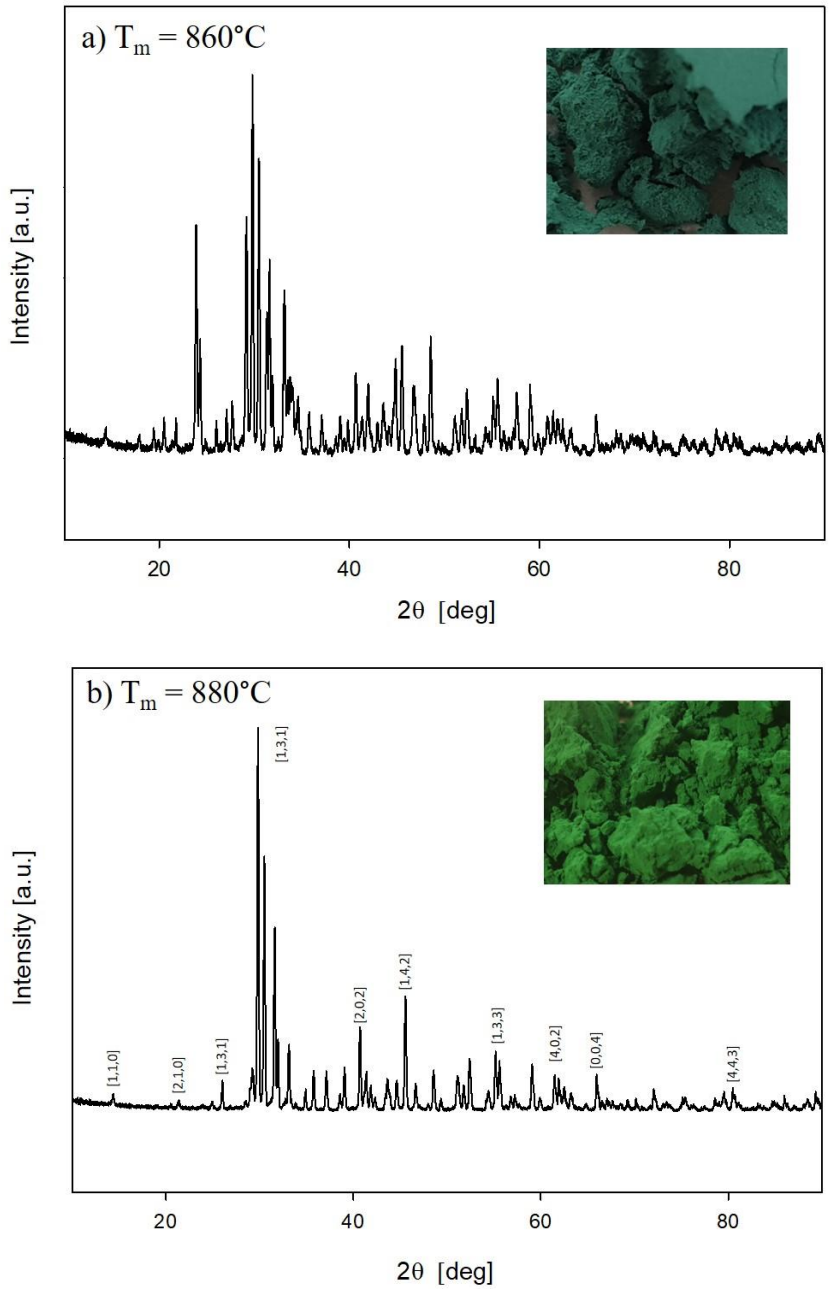

Figure 2.6 XRD result of calcined Y-211 powder; (a) third calcination at T_m = 860°C, and (b) fourth calcination at T_m = 880°C

2.1.2 Melt growth process

REBCO bulk superconductors can be synthesized by several process as discussed in chapter 1. In this study, we used top seeded melt growth (TSMG) and infiltration growth (IG) process [3, 4] for fabricating single domain bulk Y-123 and (Gd,Y,Er)-123 superconductors.

2.1.2 (a) Top seeded melt growth (TSMG)

In the TSMG process, the precursor is normally heated around 50 ^{o}C above the peritectic temperature (T_p). At this temperature, the RE-123 decomposes into RE-211 and liquid (comprised of $BaCuO_2$ and CuO) and when slowly cooled through $T_{P,}$ the RE-211 reacts with liquid to from RE-123 phase. While any unreacted RE-211 remains trapped in the matrix as inclusions.

We fabricated bulk $YBa_2Cu_3O_y$ (YBCO) superconductor via TSMG using self-made precursor powders. Calcined Y-123 and Y-211 powders were mixed in 1:0.5 molar ratio and pulverized for 2 h. The mixture was then pressed into pellets of 20 mm diameter using a uniaxial hydraulic press, with a applied pressure of 70 MPa. An Nd-123 melt-textured seed was placed at the center of the top surface of the Y-211 pre-form to grow bulk Y-123 before melt process (cool seeding technique) as shown in Fig. 2.7(a). Eventually, the pellet was placed on the small Y-211 pellets for prevent contamination from the furnace as shown in Fig. 2.7(b). Temperature profile can be varied depending on the sample size and furnace condition. as shown in Fig. 2.8 was employed. The holding time, cooling rate and other parameters

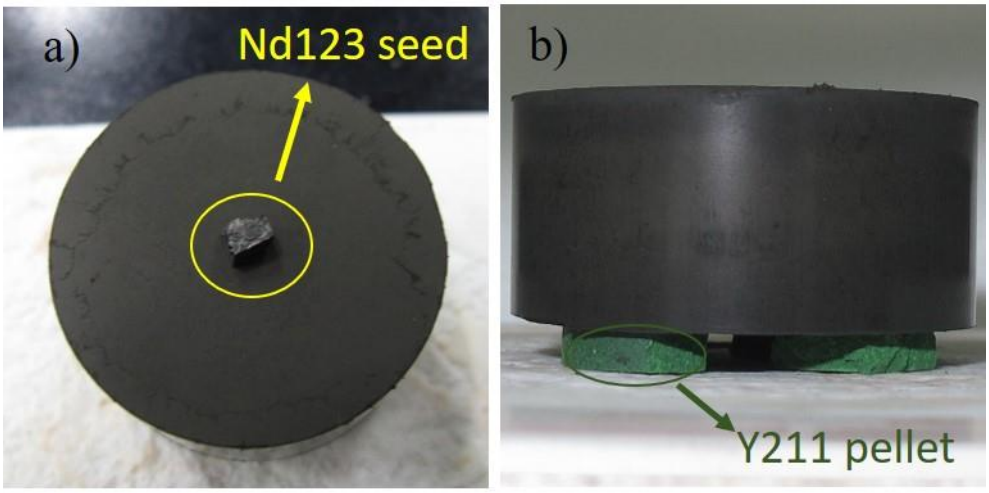

Figure 2.7 Sample assembly to fabricating Y-123 bulk superconductors by TSMG process; (a) top-view, and (b) side-view of the precursor

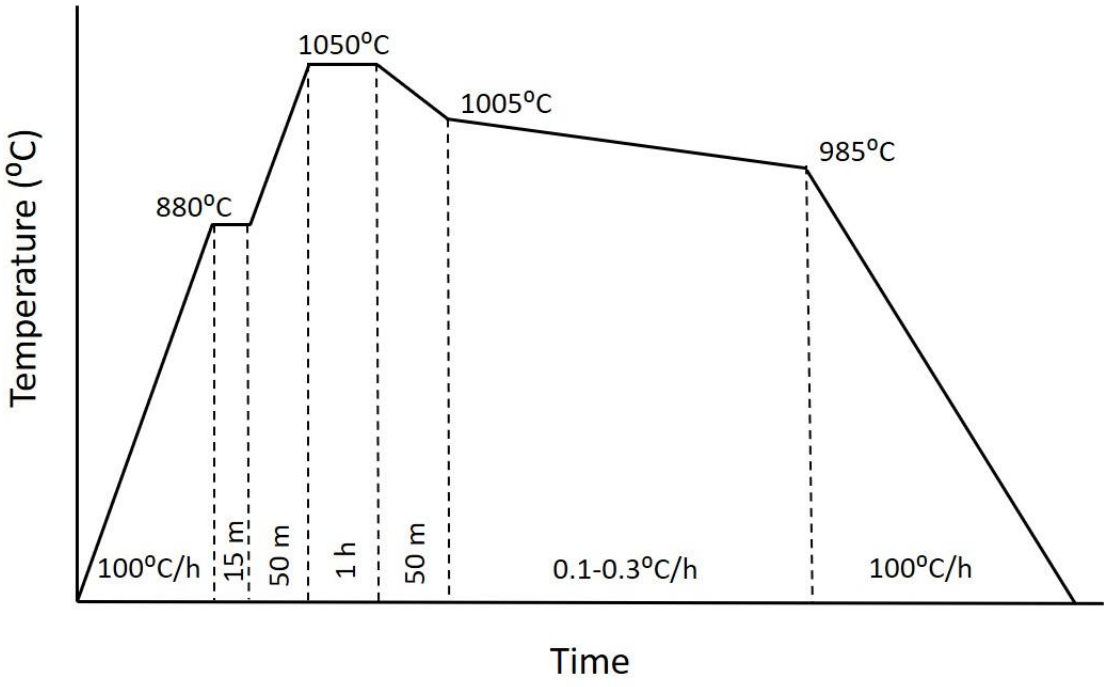

Figure 2.8 Temperature profile for the TSMG process of bulk Y-123 superconductor

2.1.2 (b) Infiltration growth (IG)

The IG process was employed to fabricate bulk (Gd,Y,Er)$Ba_2Cu_3O_y$ superconductor. This process is based on infiltration of LP into rigid porous RE-211 preform at T_p of the compound. We had utilized a new liquid phase source such as Er-123 and $Ba_3Cu_5O_8$ mixture of in a ratio of 1:1.4. RE-211 preform was made up of Gd-211, Y-211 and Er-211. More $Ba_3Cu_5O_8$ was taken in the LP mixture to ensure better and sufficient supply of LP to (Gd,Y,Er)-211 preform. (Gd,Y,Er)-211 preform and LP (Er-123 and $Ba_3Cu_5O_8$) were each pressed under a pressure 10 MPa 20 mm in diameter. A thin layer (2-3 mm) of Y_2O_3 and MgO crystal were used to support and to prevent liquid loss during the IG process. Melt textured Nd-123 seed was placed at the center of the top surface of the (Gd,Y,Er)-211 preform to promote single grain growth. The assembly for IG processing is as shown in Fig. 2.9. Temperature profile as shown in Fig. 2.10 was employed. Holding time at maximum temperature is longer than TSMG process because LP need sufficient time to infiltrate into RE-211 preform.

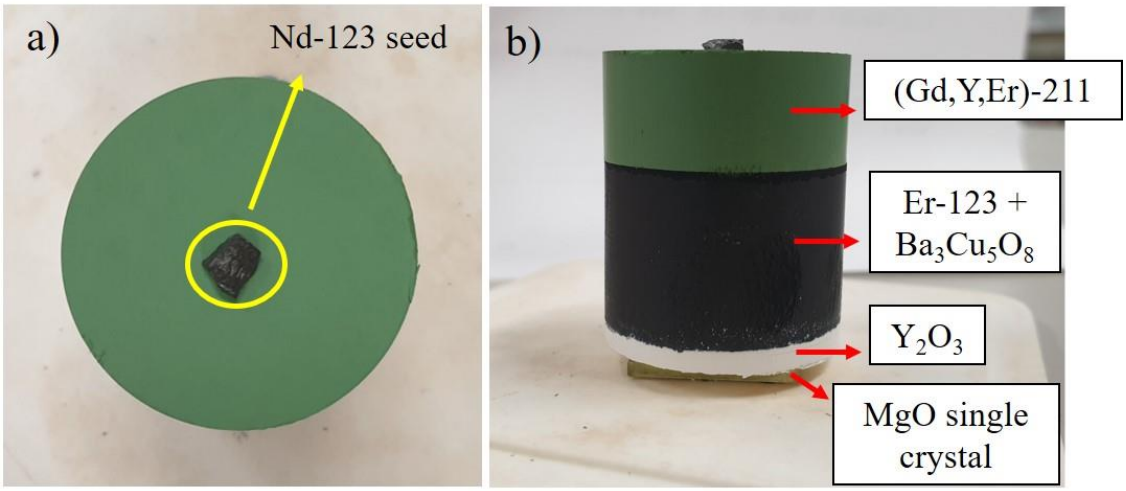

Figure 2.9 Arrangement of the sample assembly for fabricating (Gd,Y,Er)-123 bulk superconductors by IG process (a) top-view, and (b) side-view of the precursor

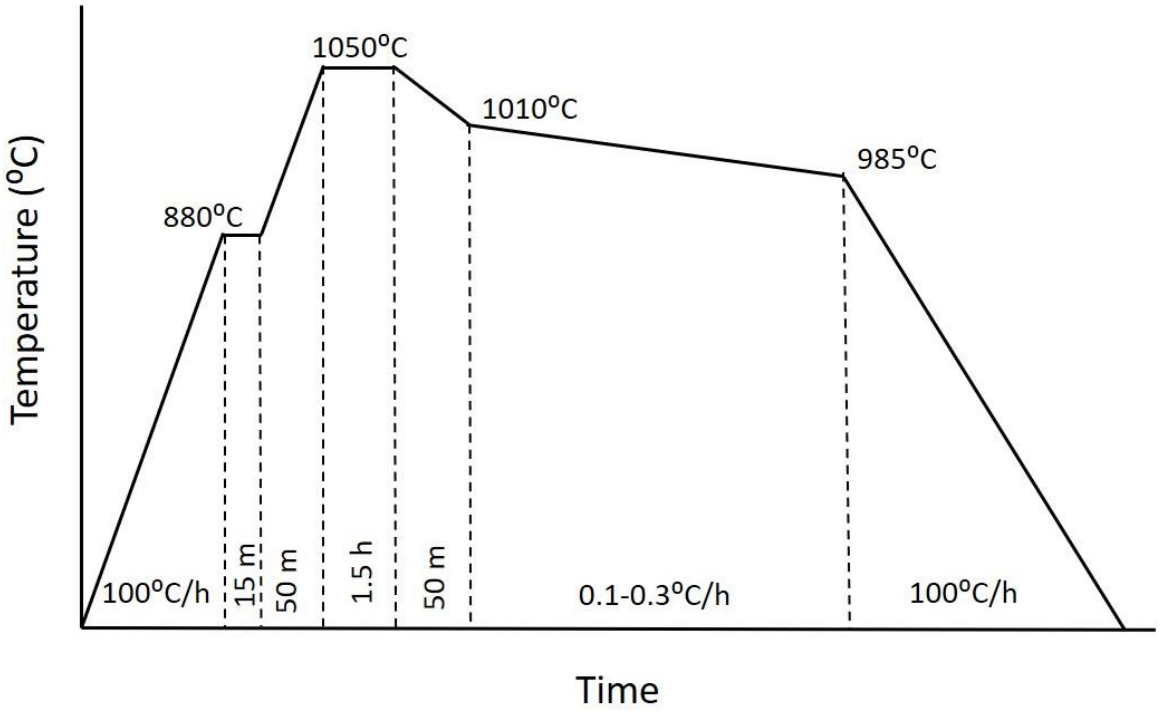

Figure 2.10 Temperature profile for the IG process of (Gd,Y,Er)-123 bulk superconductor

2.1.3 Oxygen annealing

The oxygen content is crucial to the superconducting properties, but sufficient oxygen content will not be present in the bulk RE-123soon after the fabrication. An annealing step is required to incorporate oxygen into the bulk. Annealing time and temperature can be varied depending on compound, fabrication process and size of bulk RE-123sample. The subscript "y" in bulk $YBa_2Cu_3O_y$ and bulk $(Gd,Y,Er)Ba_2Cu_3O_y$ superconductors specify the oxygen content, that can be varied between 6.2 to 7. All the as-grown RE-123bulks prepared by TSMG and IG processes are annealed in flowing 100% oxygen atmosphere at rate of 300 ml/min. for seven to ten days. Figs. 2.11(a) and (b) show oxygen annealing program employed for oxygenating $YBa_2Cu_3O_y$ and $(Gd,Y,Er)Ba_2Cu_3O_y$ bulk superconductors.

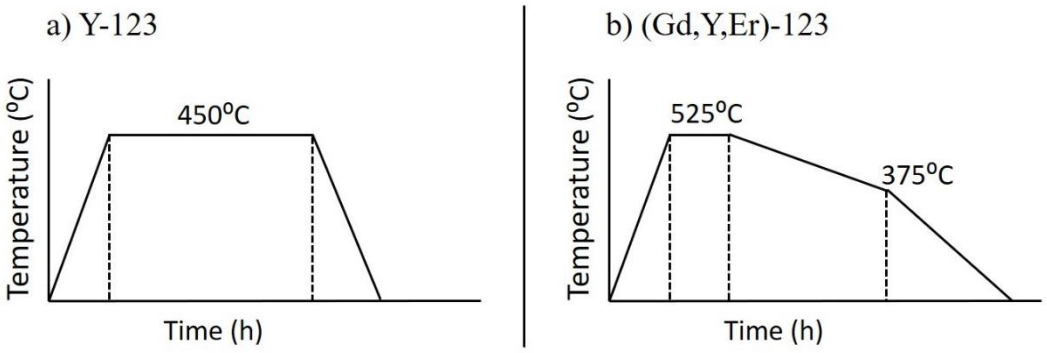

Figure 2.11 Temperature profile for oxygen annealing of bulk (a) Y-123, and (b) (Gd,Y,Er)-123

2.1.4 Refinement techniques

To improve J_c, it is necessary to control RE-211 secondary phase which can be done by using refinement technique or add chemical agents to control the morphology of RE-211 particles during melt process.

2.1.4 (a) Ultra-sonication technique

Ultra-sonication is a common technique used to disperse nanometer-sized powders. This technique when used with high energy can generate enough power to break the particles. Hence, when employed, the high energy from ultrasonic probe pass through the medium (ethanol) and creates powerful turbulence that result in violent clashes between RE-211 secondary phase particles. In detail, effective refinement of particles is obtained by cavitation phenomenon which lead to formation of small bubbles that release high energy when they pop [5]. In our work, ultra-sonication was carried by Mitsui UX-300 Ultrasonic Homogenizer with constant power (300 W) and frequency (20 kHz). Fig. 2.12 shows schematic diagram of ultra-sonication process.

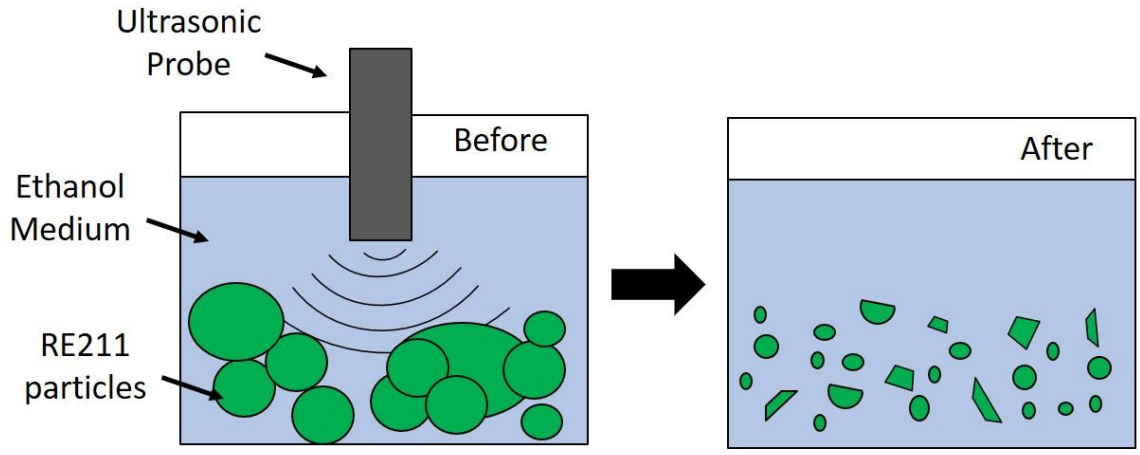

Figure 2.12 Refinement of RE-211 particles via ultra-sonication technique

2.1.4 (b) PtO_2 addition

Another way usually used for reducing the RE-211 is adding coarsening inhibitors such as PtO_2, Pt and CeO_2 [6-8]. These additives change the morphology of RE-211 particle in the RE-123 matrix. Pt-bearing compound can be formed via solid state reaction during melt process, which suppresses the RE-211 growth in the matrix [9].

In this study, 0.5 wt% of PtO_2 is added in precursors of TSMG samples and (Gd,Y,Er)-211 preform of IG samples.

2.2 Characterization techniques

2.2.1 X-ray diffraction (XRD)

X-ray diffraction analysis is one of analysis methods used for phase identification of crystalline material based on their diffraction pattern. This technique is a common tool for study of crystal structure and atomic spacing. X-ray diffractometers consist of an x-ray tube, a sample holder and x-ray detector. X-rays are generated in cathode tube by bombarding electrons created from heating a filament with a target by applying a voltage. Characteristic x-ray spectra are produced. The detector is rotated, and intensity

of diffracted x-rays is continuously recorded. The pattern is material intrinsic which generates peaks with various intensities at different angle (θ) based on the lattice planes and *d*-spacing. Bragg's law is used to explain the relationship as shown in equation 2.4

$$n\lambda = 2d\sin\theta \quad (2.4)$$

The x-ray beam at certain angles (θ) reflect the cleavage faces of crystal. λ is the beam wavelength. The variable *d* is distance between atomic layers in crystal, n is an integer. Typically, this is clarified by comparison of d-spacing with standard pattern on powder diffraction file (PDF) of each compound [10, 11]. X-ray diffractometer (Smart Lab, Rigaku Co.) was operated at 40 kV and 30 mA with Cu-K_α radiation, λ = 1.5404 Å

2.2.2 Differential thermal analysis (DTA)

DTA is a technique for identifying and quantitatively analyzing the chemical compound by thermal behavior. During a thermal cycle, the reaction and phase changes that involves absorption or emission of heat can be detected relative to the reference sample [12].

In this study, we must design temperature and time profile for TSMG and IG processing, the decomposition temperature of materials mush be determined precisely. It is necessary to use DTA to determine the temperature. We used Thermal Analysis, TG-DTA2020SA model by Bruker AXS and Al_2O_3 as a reference material.

2.2.3 Field emission scanning electron microscopy (FESEM) and energy dispersive x-ray (EDX) analysis

The microstructure and chemical analysis were observed by a Field Emission Scanning Electron Microscope (FE-SEM, model JSM-7610F and JSM-7100F, JEOL). FESEM provides topographical and element information at different magnifications. A field-emission cathode in the electron gun provides narrower probing beams at low as well as

high electron energy and then projected on the sample surface. The image for observation is formed by secondary electrons which were reflected or generated from the surface of the specimen. The advantage of FE-SEM is the ability to examine smaller-area, high-quality and low voltage images with negligible electrical charging of samples.

Energy Dispersive X-Ray (EDX), equipped with FE-SEM, was technique to identify chemical composition of material. This is a function to obtain a spectrum of the energy intensity of x-ray using a combination of semiconductor detector and spectrum analyzer [13].

2.2.4 Superconducting quantum interference device (SQUID)

For magnetization properties, a superconducting quantum interference device (SQUID, MPMS5) is used. The magnetic measurement can be determined critical current density (J_c) based on Bean extended critical state model and critical temperature (T_c) [14]. A SQUID magnetometer is extremely sensitive field sensor to measure magnetic field. The principle of SQUID as a field sensor based on Josephson effect [15, 16].

Critical current density (J_c) is the maximum current that can flow along the material under various conditions of external applied magnetic field and temperature without resistance. J_c can be obtained from the difference in the magnetization between increasing and decreasing fields at a constant temperature or the width of magnetic hysteresis loop (ΔM) at given field. In this work, magnetic moment of tiny specimen was measured during magnetic field sweep at -5 to +5 tesla. J_c was calculated by Bean extended critical state model,

$$J_C = \frac{20\Delta M}{a^2 c(b - \frac{a}{3})} \qquad (2.5)$$

where *a*,*b* are cross sectional dimensions, $b > a$ and *c* is thickness of the specimen (*a*, *b*, and *c* in mm). The specimen for measuring should be approximately 1.5 x 1.5 x 0.5 mm^3 in dimensions.

Critical temperature (T_c) was measured with applied magnetic field of 1 mT. Magnetic signal was detected with decreasing temperature. $T_{c,onset}$ occurs when the sample reaches superconducting state. $T_{c,offset}$ is temperature at which the bulk completely reaches superconducting state, usually estimated at 90% of susceptibility value. ΔT_c ($T_{c,onset}$ - $T_{c,offset}$) is superconducting transition width. Normally, if ΔT_c < 1 K, then it is assumed that a good quality bulk superconductor is fabricated.

2.2.5 Hall probe scanning

The trapped field measurements on the RE-123bulk were carried out using a Hall probe (MAGNA, MG-701). In the first step, the RE-123bulk specimen was cooled under a field of 1 T up to 77.3 K and left there for 15 min, this type of magnetization is usually termed as field cooling (FC). Note that we have 2 kind of magnetic field generators, which are permanent magnet (0.45T) and electromagnet (1 T). After removing the applied field, we waited for 30 s and then the trapped field distribution was measured by scanning the surface with Hall sensors at the distance of 1.3 mm. The field distribution is used to prove the prefect single domain nature of the bulk, absence of any large cracks and field symmetry of the sample [17].

References

1. Chin, T.S., et al., *The Formation of Y-Ba-Cu-O Phases During Solid State Reaction.* MRS Proceedings, 1987. **99**: p. 261.

2. Huang, T.W., et al., *The formation of superconducting $YBa_2Cu_3O_{7-x}$ through solid state reaction.* Journal of Crystal Growth, 1988. **91**(3): p. 402-409.

3. Jin, S., et al., *High critical currents in Y-Ba-Cu-O superconductors.* Applied Physics Letters, 1988. **52**(24): p. 2074-2076.

4. Chen, Y.L., et al., *A new method for net-shape forming of large, single-domain $YBa_2Cu_3O_{6+x}$.* Physica C: Superconductivity, 1994. **234**(3): p. 232-236.

5. Brennen, C.E., *Cavitation and Bubble Dynamics*. 2013, Cambridge: Cambridge University Press.

6. Riches, J.D., J.A. Alarco, and J.C. Barry, *Effects of PtO_2 and CeO_2 additives on the microstructures of the quenched melts of Y–Ba–Cu–O materials.* Physica C: Superconductivity, 2000. **336**(1): p. 43-56.

7. Diko, P., et al., *The influence of starting particle size and Pt/Ce addition on the microstructure of melt processed bulks.* Superconductor Science and Technology, 1998. **11**(1): p. 49-53.

8. Varanasi, C., M.A. Black, and P.J. McGinn, *A comparison of the effects of PtO_2 and $BaSnO_3$ additions on the refinement of Y_2BaCuO_5 and magnetization of textured $YBa_2Cu_3O_{6+x}$.* Superconductor Science and Technology, 1994. **7**(1): p. 10-16.

9. Kim, C.-J., et al., *Role of PtO_2 on the refinement of Y_2BaCuO_5 second phase particles in melt-textured Y-Ba-Cu-O oxides.* Physica C: Superconductivity, 1997. **281**(2): p. 244-252.

10. Allardice, L.D.W.W.R., *X-Ray Diffraction Techniques*, in *Methods of Soil Analysis*, W.R.A. L. D. Whittig, Editor. 1986. p. 331-362.

11. Azároff, L.V., et al., *X-ray Diffraction*. Vol. 3. 1974: McGraw-Hill New York.

12. Jose Chirayil, C., et al., *Chapter 1 - Instrumental Techniques for the Characterization of Nanoparticles*, in *Thermal and Rheological Measurement Techniques for Nanomaterials Characterization*, S. Thomas, et al., Editors. 2017, Elsevier. p. 1-36.

13. Ltd., J. *Scanning Electron Microscopes (SEM)*. JEOL 1996-2021 [cited 2021 10 January]; Available from: https://www.jeol.co.jp/en/science/sem.html.

14. Bean, C.P., *Magnetization of High-Field Superconductors.* Reviews of Modern Physics, 1964. **36**(1): p. 31-39.

15. Josephson, B., *The discovery of tunnelling supercurrents. Rev. Mod.* 1974.

16. Josephson, B.D., *Coupled Superconductors.* Reviews of Modern Physics, 1964. **36**(1): p. 216-220.

17. Ren, H.T., et al., *The fabrication and properties of single domain YBCO disk.* Physica C: Superconductivity, 1997. **282-287**: p. 485-486.

Chapter 3

Bulk $YBa_2Cu_3O_y$ Superconductors with Ultra-sonicated Y_2BaCuO_5 Secondary Phase Particles

3.1 Introduction

High temperature bulk superconductors are specifically attractive for various engineering applications, like magnetic shielding in electric machines and high-field devices [1], high-field magnet systems for medical devices with drug delivery [2], flux trapped field magnets for replacing conventional permanent magnets [3]. The $REBa_2Cu_3O_y$ (RE: rare earth element such as Y, Gd, Sm, Dy, Nd, etc.) is a special class of high temperature bulk superconductors, with the broadest range of operating temperatures. At present, the most effective way for synthesizing the bulk $REBa_2Cu_3O_{7-\delta}$ superconductors is the melt-growth process. The precursor is heated above a peritectic temperature depending on combination of rare earth elements and carefully cooled to achieve the single-grain growth. The

$REBa_2Cu_3O_{7-\delta}$ decomposes forming RE_2BaCuO_5 and liquid phase (Ba-Cu-O) and then it is slowly cooled through peritectic temperature to re-form to the $REBa_2Cu_3O_y$ superconducting phase [4]. Top-seeded melt-growth (TSMG), especially with cold seeding technique, is widely used to fabricate high performance $YBa_2Cu_3O_y$ (Y-123) in batch production [5]. Critical current density (J_c) and trapped flux field (B_T) in Y-123 bulk superconductors can be improved by reducing the size of secondary phase (Y_2BaCuO_5, Y211) in the superconducting matrix. A fine and homogeneous Y-211 secondary phase contributes to J_c enhancement [6, 7]. This is because of increase of interface between Y-123 and Y-211 phases that enables an effective magnetic flux pinning. Microstructural defects, such as oxygen vacancies, micro-cracks, stacking faults, impurity phase precipitates, contribute to the enhancement of J_c, too [8]. Other techniques to control the Y-211 particles are chemical doping by Pt, PtO_2 or Ce and the mechanical refining of Y-211 particles by ball milling, micro-emulsion method, or solution blow spinning technique [9-13]. The ball milling is an effective way to refine and control shape of Y-211 particles. But the limitation of this technique is that it introduces small quantity of ZrO_2 (from planetary milling balls) into the powder, which degrades the superconducting properties [14]. The microemulsion method can produce Y-211 particles with a size smaller than 500 nm. The drawback of this method is that the reaction time and heat treatment parameters are very difficult to control and there is possibility of a chemical inhomogeneity in the final powder [12]. Another innovative technique is solution blow spinning technique, by which nano Y-211 whiskers less than 500 nm can be produced. Recent studies of using solution blow spinning technique and the buffer-aided top seeded melt growth of Y-123 bulk (diameter 20 mm, CeO_2 added) resulted in 39 kA/cm^2 in self-field at 77 K [13]. We tried to find an alternative technique to reduce processing time, avoid contamination, and to hassle free effectively refine the Y-211 powder. We employed a new technique of "high energy ultra-sonication" and studied its effect on the Y-211 particle size and shape, as well as on the final bulk Y-123 's superconducting properties. Ultra-sonication is a clean well-established technique for sludge attrition [15]. During ultra-sonication, high energy waves are generated at high frequency from an ultrasonic probe. They break and

agglomerate the particles via cavitation [16, 17]. In detail, small bubbles generated during ultra-sonication effectively accumulate the widespread energy passing through the liquid and directly impact the particles [18]. The particles size is refined in various amount by tuning power and frequency of the instrument. The particles edges and surfaces are destroyed via shearing and bombardment from the ultra-sonication technique [19].

In this study, we investigated the purity and particle size of Y-211 when subjected to ultra-sonication. Y-123 sample was fabricated by TSMG process using the ultrasonically refined Y-211. The effect of grain refining agent was also studied by doping 0.5Wt% of PtO_2 additives in the precursor and without PtO_2 additive. Y-123 single grain superconductors of 20 mm were fabricated by Top-seeded melt growth. Systematic study was done by varying the ultra-sonication time and superconducting properties were compared to highlight the best processing conditions.

3.2 Experimental details

To reduce the particle size of the calcined Y-211 powder, we used Mitsui ultrasonic homogenizer UX-300, while keeping constant power (300 w) and frequency (20 kHz). Y-211 powder was dissolved into ethanol and ultra-sonicated systematically for various durations such as 0-100 minutes at 20 minutes interval. The dried Y-211 powders after ultra-sonicated were analyzed by field-emission scanning electron microscope (FESEM). To compare the effect of ultra-sonication, we were synthesized bulk Y-123 sample with ultra-sonicated Y-211 powder which will be referred to as Y0, Y20, Y40, Y60, Y80, and Y100 respectively of without PtO_2 additive condition and YPt0, YPt20, YPt40, Y60, Y80, and YPt100 referred with 0.5 wt% PtO_2 additive. The Y-211 and Y-123 powders were mixed in 1:2 ratio and was pulverized for 2 hours, which were then pressed into several pellets of 20 mm diameter. Nd-123 seed was placed on the top of pelletized precursor mixture. The temperature profile used for fabricating samples for TSMG is given in Fig. 2.8. After melt processing, the Y-123 samples were annealed at 450ºC for 400 h in controlled oxygen atmosphere for oxygenation [20, 21].

For The phases present in the bulk were identified by X-ray diffraction (XRD) using Rigaku X-ray diffractometer with 2θ from 10° to 80°. The superconducting performances were discussed. Trapped field measurements, we used permanent magnet of 0.45 and electrical magnet 1 T to activate Y-123 bulk superconductor. Field distribution was measured by automatic scanning Hall probe sensor at a distance of 0.3 mm (surface touched) and 1.3 mm (1 mm above surface) above the superconductor surface. The microstructures were studied with a FESEM. For magnetic measurements, samples were cut 2 mm below the seed along the *c*-axis from the bulk samples 1.5 x 1.5 x 0.5 mm^3 in dimension. Superconducting transition temperature (T_c) and magnetization loops in field from 0-5 T were measure at 77 K using a commercial SQUID magnetometer (model MPMS5). Superconducting critical current density (J_c) were estimated by the extended Bean's model [22].

3.3 Results and discussion

3.3.1 Ultra-sonicated Y_2BaCuO_5 secondary phase particle analysis

Y-211 secondary phase particles in bulk YBCO superconductors acts as a non-superconducting phase and is crucial in the growth and improving the superconducting properties of bulk. The ultra-sonication technique in this experiment resulted in refined Y-211 particles and distorted surface Y-211 particles. The fine ultra-sonicated Y-211 particles at various time depicted in Figs. 3.1(a)-(f) by FESEM observation. Their size was at 72.32% bigger than 5 μm as in Fig. 3.1(a). After employing ultra-sonication, the Y-211 secondary phase particles became smaller with increasing ultra-sonication time. For Y-211 powders ultra-sonicated at 20, 40 and 60 minutes, the percentage of particles smaller than 2 μm was 8.87%, 18.51%, and 34.32%, respectively. In the cases of Y-211 powder ultra-sonicated for 80 and 100 minutes, more than 90% of the particles were smaller than 2 μm, along with 1.25% and 8.05% of particles smaller than 500 nm, respectively. The rate of particles refinement reduced as the ultra-sonication time

increased, indicating that the technique reaches saturation after a certain duration. High magnification FESEM images of Y-211 ultra-sonicated at 0, 80, and 100 minutes shown on Figs. 3.2(a)-(c), respectively. It can be observed that the size of Y-211 particles down to several nanometers when the Y-211 powder was ultra-sonicated for 80 and 100 minutes. The pristine Y-211 powder before ultra-sonication comprised particles rough, of irregular shapes, clustered to form large particle as show in Fig. 3.2(a). In addition to the breakdown of clusters, the individual particles were also damaged resulting in different shapes and damaged surfaces as shown in Figs. 3.2(b) and (c). The probability of Y-211 consumption in the peritectic reaction is significantly higher for smaller particles than larger ones. In previous studies where ball milling was employed, size refinement less than 0.1 μm was observed [23, 24]. However, the technique is expensive and there are several cases where contamination from the ceramic balls used for milling was observed. Although the contamination mostly has negative effects, fortunately in some cases, these contaminations can act as nano pinning centers that can enhance critical current density such as in case of zirconia balls. When zirconia balls were used for long durations of ball milling, Zr based contaminations are formed and helped in improving the performance [25]. Hence, we think that the ultra-sonication technique employed into Y-211 particles, refines the particles to submicron sizes cost effectively with nearly no contamination.

To verified purity for ultra-sonicated powder of Y-211 at various time, XRD analysis were examined. Fig. 3.3 show the XRD patterns, there were not changed when employed the high energy ultrasonic wave to the Y-211 powder as compared to the XRD pattern of Y-211 at 0 minute. All peaks corresponding to the Y-211 single phase and ultra-sonication have no contamination into the Y-211 powder and also the crystallinity.

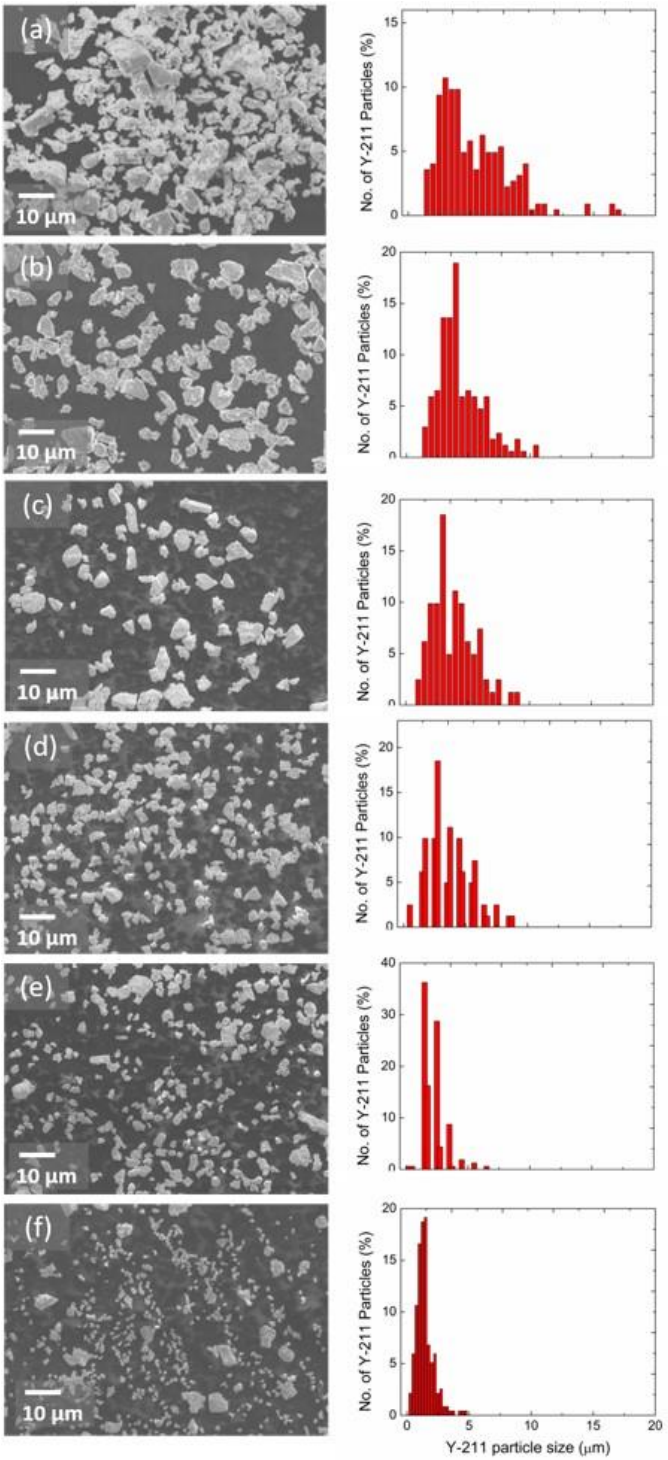

Figure 3.1 FESEM images and histograms of Y-211 powder of ultra-sonication for (a) 0, (b) 20, (c) 40, (d) 60, (e) 80, and (f) 100 minutes

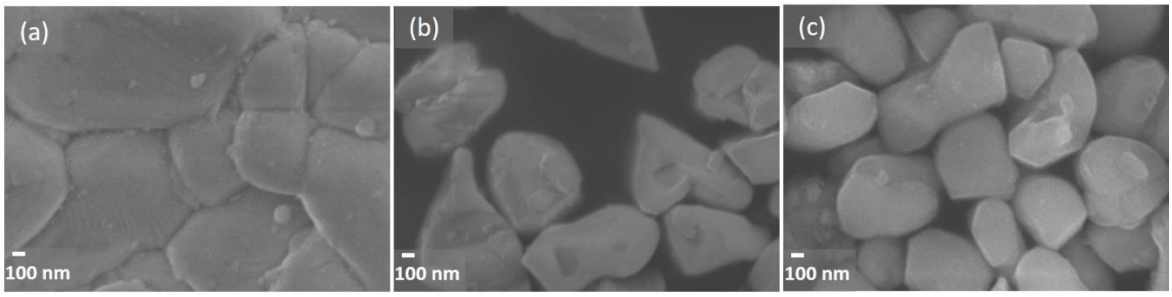

Figure 3.2 High magnification FESEM images of Y-211 ultra-sonicated at (a) 0, (b) 80, and (c) 100 minutes

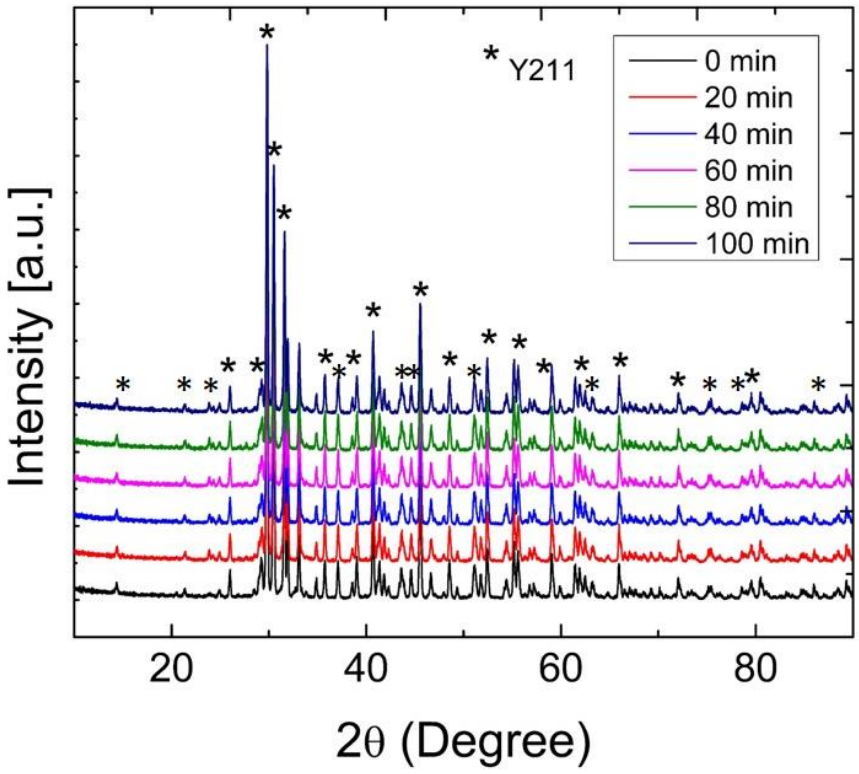

Figure 3.3 X-Ray diffraction patterns for Y-211 ultra-sonicated at 0-100 minutes

3.3.2 Fabrication of bulk Y-123 superconductors without PtO_2 addition

3.3.2 (a) Fabrication of bulk Y-123

The bulk Y-123 superconducting materials were synthesized using optimal temperature profile for TSMG process. The top surface of all samples of bulk Y-123 produced with Y-211 ultra-sonicated powders are shown in Figs. 3.4 (a)-(f). The dimensions of final samples were around 17.5 - 18 mm in diameter slightly less than 20 mm (initial size), which is expected in the as-grown sample by TSMG process [6]. All samples show four-fold growth from seed in the form of a single grain bulk sample and this growth extends from top surface to bottom surface giving proof of a good *c*-axis growth. We confirmed the phase purity of bulk Y-123 samples using X-Ray diffraction (XRD) via Rigaku-SmartLab. Fig. 3.5 shows all (*00l*) peaks corresponding to the orthorhombic *ab* planes of bulk Y-123 superconductor, which indicates a proper texturing and pure single grain nature of the bulk [26]. This clearly proves that there are no contaminations or degrading effects upon using the ultra-sonicatedY-211 powders to synthesize Y-123 bulk.

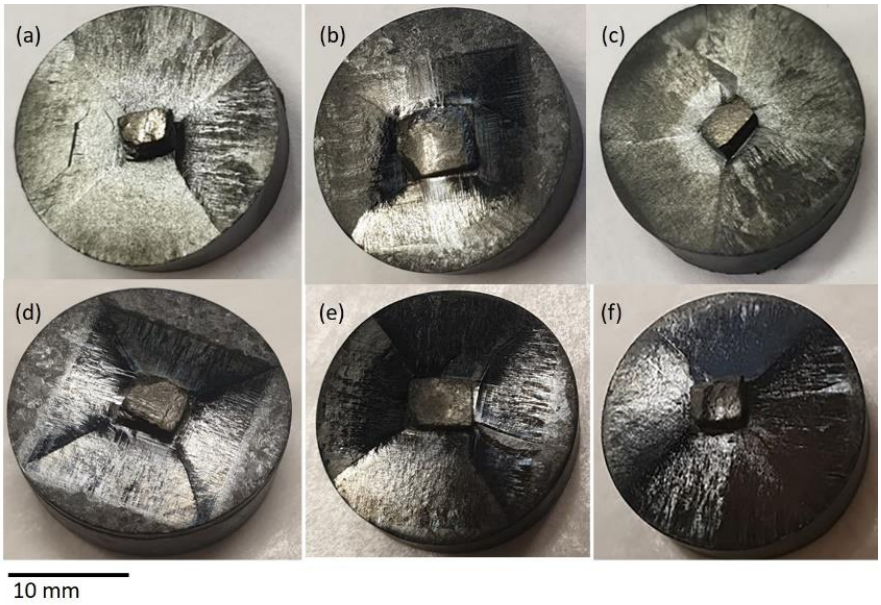

Figure 3.4 Top view of as-grown (a) Y0, (b) Y20, (c) Y40, (d), Y60, (e) Y80, and (f) Y100 bulk samples

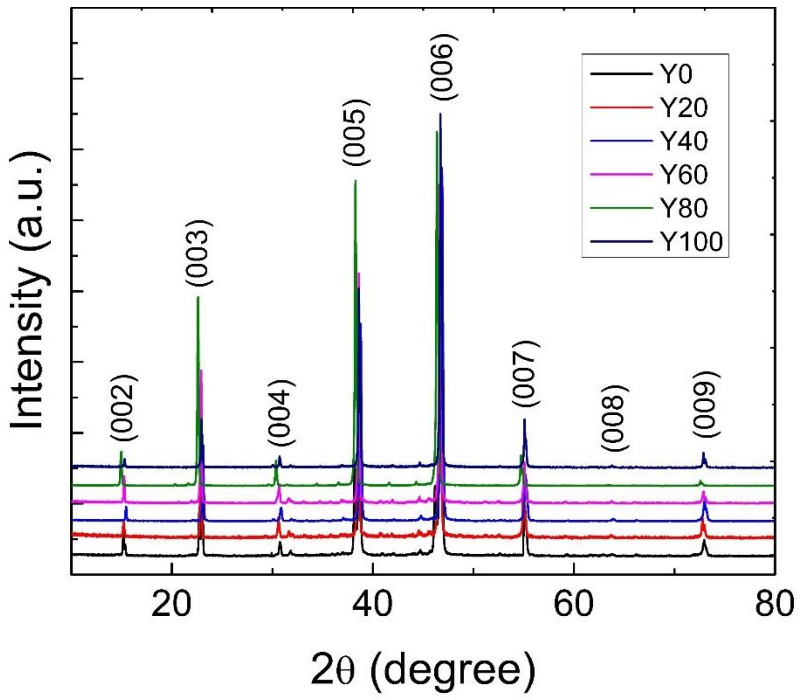

Figure 3.5 X-Ray diffraction patterns for bulk Y-123 samples fabricated with ultra-sonicated Y-211 for 0-100 minutes

3.3.2 (b) Trapped field experiments

Trapped field is one of the most important parameters to justify the performance of the superconducting bulk. For measuring trapped field distribution, all the samples were field cooled by liquid nitrogen (77.3 K) under an applied magnetic field of 0.45 (via permanent magnet) and 1 T (via electro-magnet). Hall sensor was placed 0.3 and 1 mm above the surface of bulk samples and the trapped field distribution was measured. The trapped field values at 0.3 mm above the surfaces of Y0 and Y20 samples with the applied magnetic field of 1 T reached 0.22 T, while that of Y40, Y60 and Y80 samples reached ~ 0.27 T, and for the Y100 sample it reached 0.29 T. This trapped field can be further improved by increasing the sample size, and by making microstructure more uniform [27]. In Fig. 3.6, the trapped field profile of Y100 sample measured at 77.3 K with applied magnetic field of 0.45 T was depicted. It reached 0.19 T. The single cone peak distribution confirmed the

single-grain character without cracks in the bulk. In addition, alternative techniques such as infiltration growth or buffer layer melt process can also result in a large, high quality single-grain bulk [9, 28]. The trapped field values of other samples with various ultra-sonication times, measured at 77.3 K at an applied magnetic field of 1 T, are displayed in Fig. 3.7. It is evident that the superconducting performance depends on the Y-211 particle size. This is because the trapped field performance of bulk superconductors is related to flux pinning. The trapped field values slightly increase with increase in the ultra-sonication duration. The highest value was achieved in Y100 sample and the lowest value was recorded in Y0 and Y20 samples. This evidence shows the improvement of trapped field value with achieving smaller and more uniform Y-211 secondary phase particles in the Y-123 matrix. The final particles size of Y-211 secondary phase in the bulk Y-123 matrix depends on the initial Y-211 powder size, reduction of which can be achieved by means of ultrasonic technique.

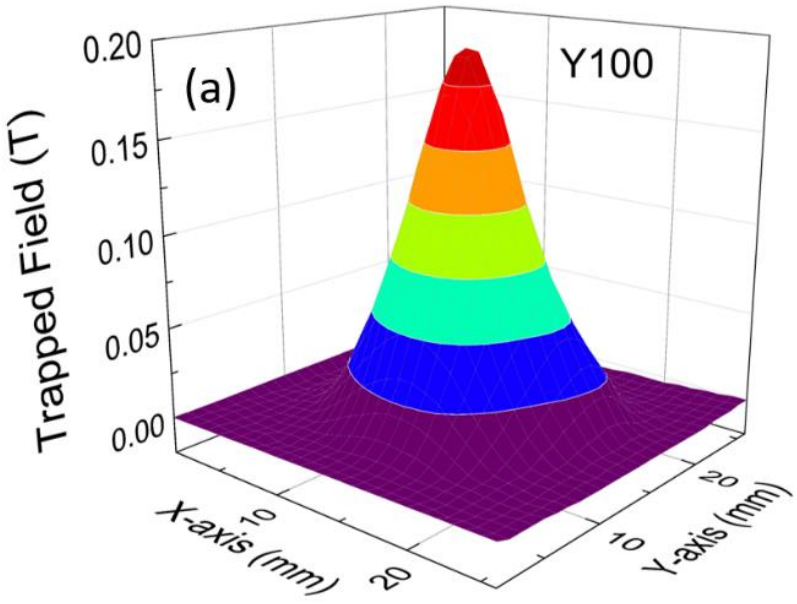

Figure 3.6 The trapped field distribution under an applied magnetic field of 0.45 T at 77.3 K and 1.3 mm above the top surface for Y100 sample

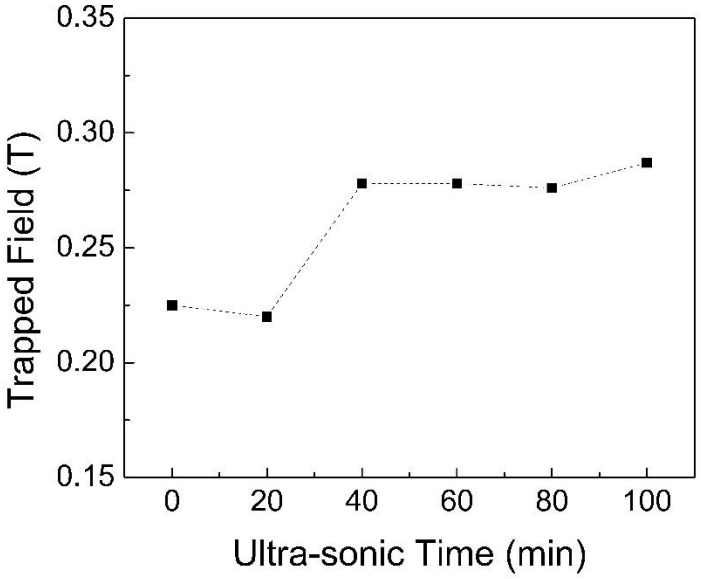

Figure 3.7 Trapped field values Y-123 sample without PtO_2 addition under an applied magnetic field of 1 T at 77.3 K and 0.3 mm above the top surface as a function of ultra-sonication times

3.3.2 (c) Superconducting properties

Fig. 3.8 shows superconducting transition temperature of bulk Y-123 superconductors determined from measuring temperature dependence of DC susceptibility. All samples exhibited $T_{c,onset}$ between 91 and 92 K with superconducting transition width less than 1.5 K, similar to $T_{c,onset}$ of bulk Y-123 superconductors [29]. These results prove that the ultra-sonication technique does not affect quality of the samples, always reflected in the superconducting transition temperature and width. The high purity of Y-211 powder after ultra-sonication, implies that the technique is much safer, unlike ball-milling, which introduces impurities into the Y-211 powder [30].

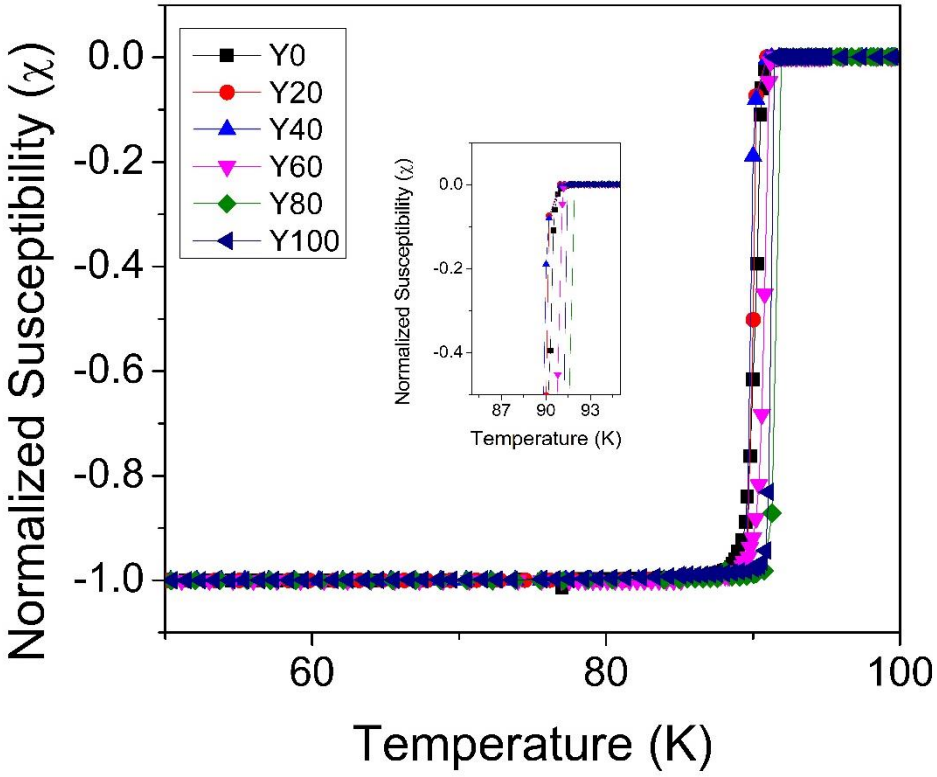

Figure 3.8 The temperature dependence of DC susceptibility measurements of bulk Y-123 material fabricated with Y-211 ultra-sonicated

The critical current density (J_c) was measured with magnetic field parallel to the *c*-axis at 77 K on small platelet Y-123 samples. The highest J_c values were observed in Y100 sample, 38 kA/cm^2 at self-field (H//*c*-axis) and 13 kA/cm^2 at the peak position, at 1.5 T (H//*c*-axis) as presented in Fig. 3.9. This result is in accordance with the trapped field measurements. It is known that J_c of Y-123 bulk superconductor depends on the microstructural features such as secondary phase inclusions trapped in the Y-123 matrix [9, 14]. The peak effect can be observed at 1.5 T in Y60, Y80 and Y100 samples with J_c reaching 8.17, 9.4 and 13 kA/cm^2, respectively, and then decreases with increasing applied field. The Y0 sample showed the lowest self-field J_c value which was around 29 kA/cm^2 at 77 K (H//*c*-axis). The secondary-peak J_c at 1.5 T increased systematically with increasing ultra-sonication time. It implies that J_c value of Y-123 samples increases with decreasing size of the precursor Y-211 powder.

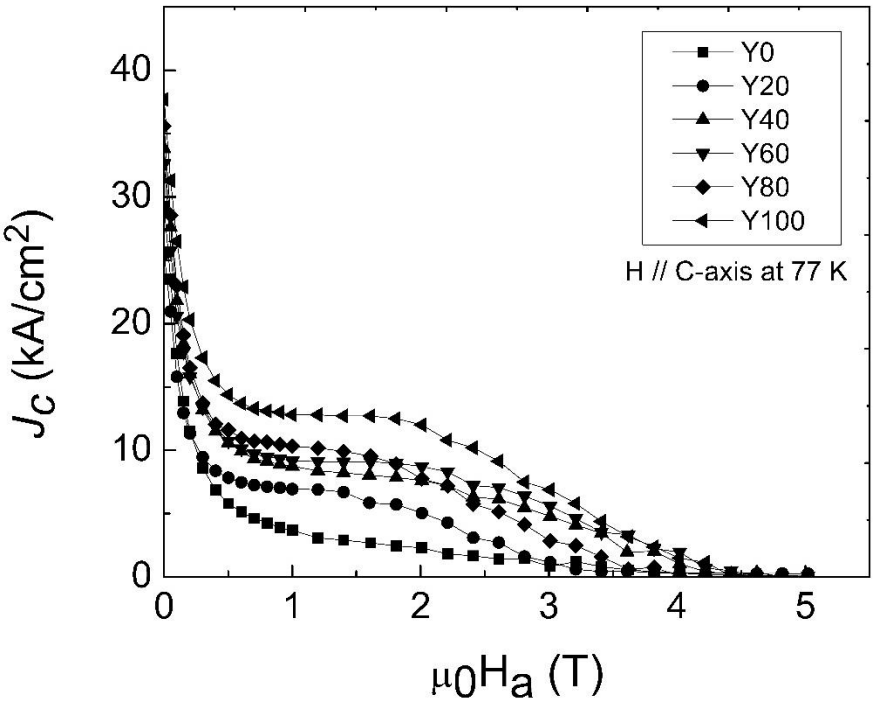

Figure 3.9 Field dependences of the critical current density of bulk Y-123 samples at 77 K, H//*c*-axis

From the above results it follows that ultra-sonication, a low cost and time conserving technique, is a promising route for enhancing flux pinning by controlling Y-211 secondary phase in Y-123 superconductor, better than other methods, like solution blow spinning or ball milling techniques [9, 13].

The pinning mechanism was interpreted in terms of Dew-Hughes equations i.e. the normalized flux pinning force density curve against reduced magnetic field. The flux pinning force density, F_p was estimated using the expression of $F_p = J_c \times B$ from measurements of the superconducting critical current density. The normalized pinning force is denoted by $f_p = F_p/F_{p,max}$, where $F_{p,max}$ is the maximum pinning force density. The reduced field along *c*-axis is $h = H_a / H_{irr}$, where H_a is the applied field and H_{irr} is irreversibility field obtained from the J_c-H curve as the field, where J_c reaches 100 A/cm^2.

The peak on the f_p-h curves at h_0 = 0.3 corresponds to vortex core pinning by small size normal defects [31, 32]. Fig. 3.10 presents the normalized volume pinning force as a function of the reduced field, h, at 77 K for Y0 and Y100 samples. Peak position, h_0, of Y0 and Y100 samples was located at 0.38 and 0.49, respectively. The peak shifted to higher fields with increasing ultra-sonication time. The Y-211 particles treated by the ultra-sonication technique create evidently a strong pinning structure in the matrix. The peak position above 0.33 can be attributed to fine Y-211 particles and oxygen deficient clusters in the Y-123 matrix, which cause a variation of the transition temperature (δT_c pinning) [33, 34]. They are also responsible for peak effect at high fields, which is desirable for engineering application.

3.3.2 (d) Microstructure analysis

Fig. 3.11 shows the FESEM images of Y0 and Y100 samples. One can see small Y-211 particles in the preform were consumed during the peritectic reaction and have grown into slightly larger Y-211 distributed all over the bulk Y-123 matrix. The average size of the 211 phases in Y0 and Y100 was less than 2 μm and the volume fraction was 28.17% and 58.62%, respectively. In addition, volume fraction of the particles smaller than 1 μm in the Y100 sample was 22.41%. In any case, the density of small Y-211 phase particles was in the Y100 sample higher than that of Y0 sample. Accordingly, the Y100 sample exhibited a higher J_c and trapped field compared to other samples.

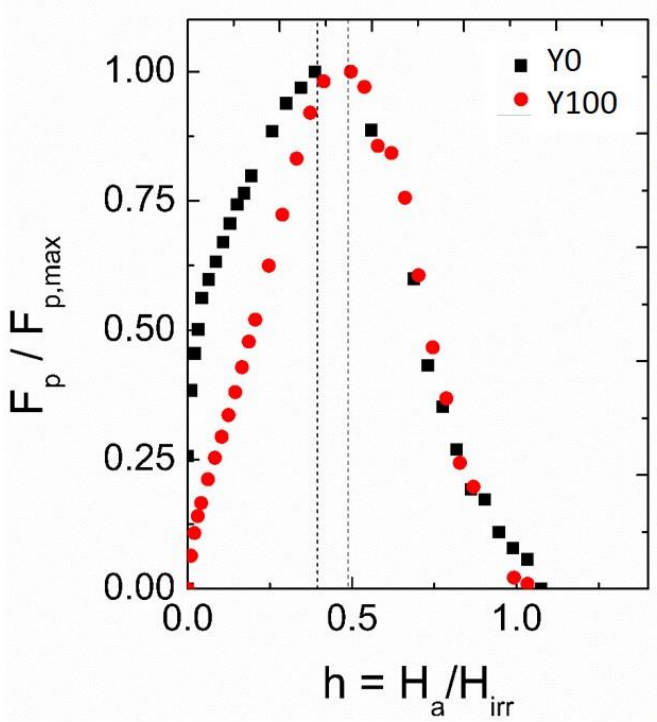

Figure 3.10 The normalized flux pinning curve, $F_p / F_{p,max}$ as a function of the reduced field, $h = H_a / H_{irr}$ for Y0 and Y100 samples.

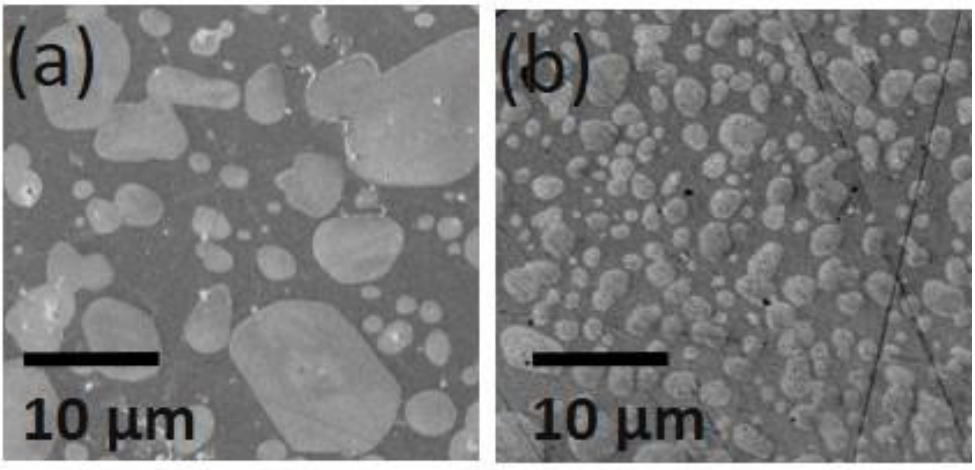

Figure 3.11 FESEM images of a) Y0, and b) Y100 samples

The Y-211 secondary phase particles created via ultra-sonication, led to an improvement in superconductive properties of melt grown bulk Y-123 without a grain refining agent. Optimum sized and uniformly shaped Y-211 secondary phase particles were prepared by 100 minutes of ultra-sonication with optimum frequency and power. FESEM micrographs were used to estimate particle size distribution which revealed that in the sample Y100, 90% of the particles were less than 2 μm and 8.05% of them were less than 500 nm. The original Y-211 secondary phase particles were scattered into much smaller individual particles with sharp edges. In the final Y-123 bulk samples, fine 211 secondary phases were observed, uniformly dispersed over the bulk. All samples showed a sharp superconducting transition at T_c ~ 91-92 K (ΔT < 1.5 K). Among all the sample, Y100 sample showed the best superconducting performance. J_c at self-field and 77 K was 37 kA/cm^2 and trapped field profile exhibited a single cone shape with the maximum value of 0.29 T at the center and 77.3 K.

3.3.3 Fabrication of bulk Y-123 superconductors with PtO_2 addition

3.3.3 (a) Fabrication of bulk Y-123

The top-view photograph of Y-123, 20 mm in diameter samples with Y-211 refined via ultrasonic time of 0-100 minutes were displayed in Figs. 3.12(a)-(f) respectively. Fully four-fold growth was seen without any spontaneous nucleation from the seed crystal and growing on four sectors to the edge of samples along *ab*-plane and the top to the bottom along *c*-axis, represent the samples are growing in form of a single grain.

Single grained samples were prepared by implementing the optimized temperature profile with TSMG process. In addition, this technique in conjunction with batch processing can aid in mass production of high-quality bulk YBCO superconductors at low costs.

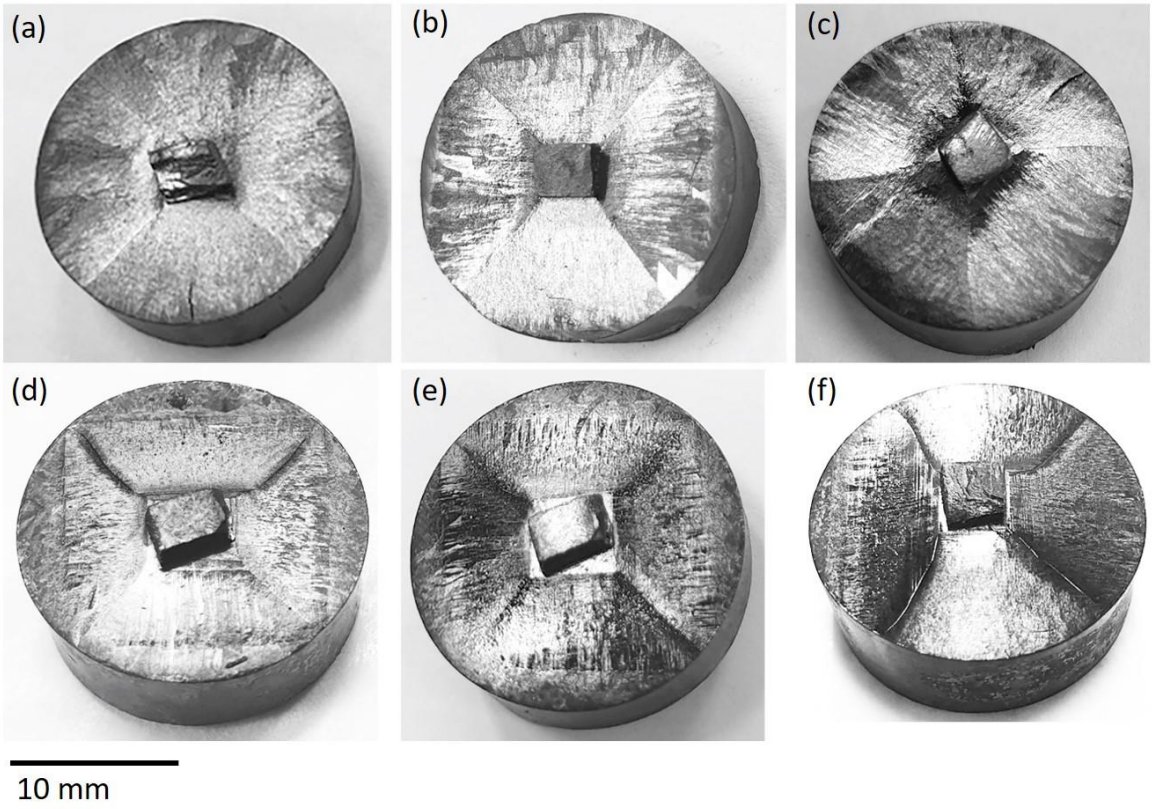

Figure 3.12 Top view of as-grown (a) YPt0, (b) YPt20, (c) YPt40, (d), YPt60, (e) YPt80, and (f) YPt100 samples

To examine the texturing information and phase purity of melt grown bulk Y-123, we performed X-Ray diffraction on flakes cleaved from YPt0, YPt40, and YPt80 samples. Fig. 3.13 shows all (*00l*) peaks corresponding to the orthorhombic *ab* planes, which indicates a proper texturing and pure single grain nature of Y-123 formed [26].

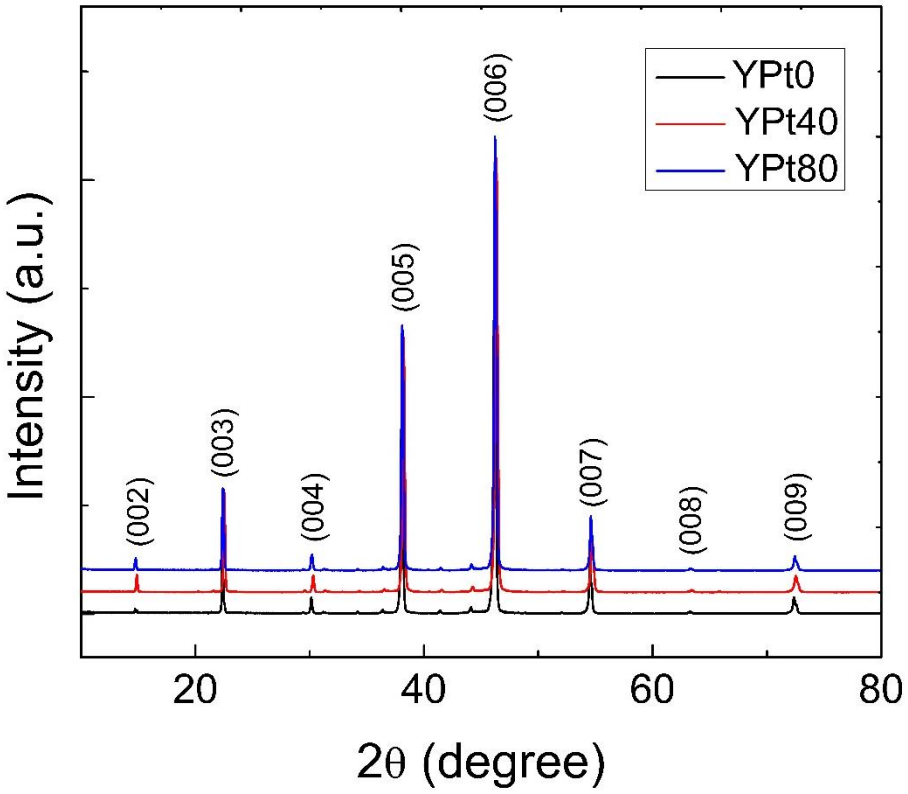

Figure 3.13 X-Ray diffraction patterns for YPt0, YPt40 and YPt80 samples

3.3.3 (b) Trapped field experiments

Trapped field of the samples was measured at 77.3 K after field-cooling in magnetic field of 0.45 and 1 T. High trapped field of 0.42 T at 77.3 K was observed in sample YPt80 at 0.3 mm distance from the top surface sample when field-cooled in presence of 1 T. More results of trapped field distribution of YPt80 sample under a magnetic field of 0.45 T were presented in Fig. 3.14. The profile was showing a uniform single cone curve in the center, indicating that the sample has uniform single grain growth without cracks and underwent good oxygen treatment. Fig. 3.15 represents the trapped field (0.3 mm away from the top surface) against ultra-sonication time, for all samples that are field-cooled with 1 T at 77.3 K. Effect of ultra-sonication time with trapped filed measurement relate with the J_c results and show the highest value in Y-211 with 80 minutes' ultra-sonication.

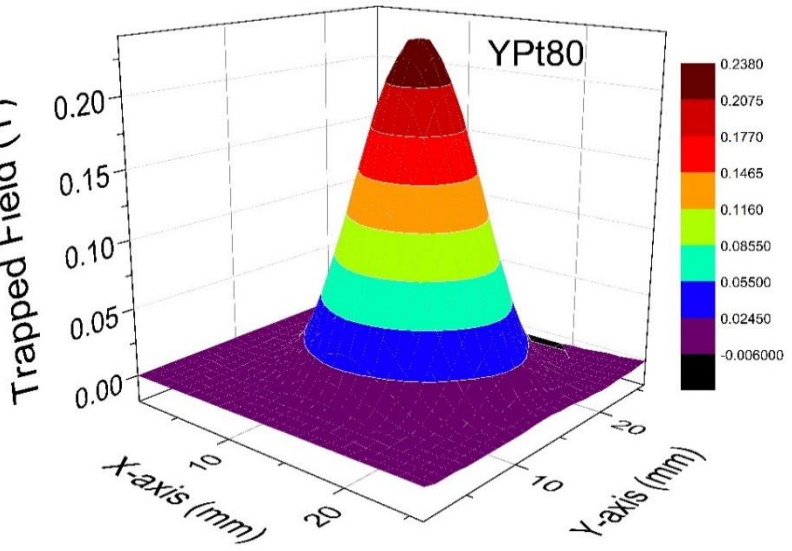

Figure 3.14 The trapped field distribution under an applied magnetic field of 0.45 T at 77.3 K and 1.3 mm above the top surface for YPt80 sample

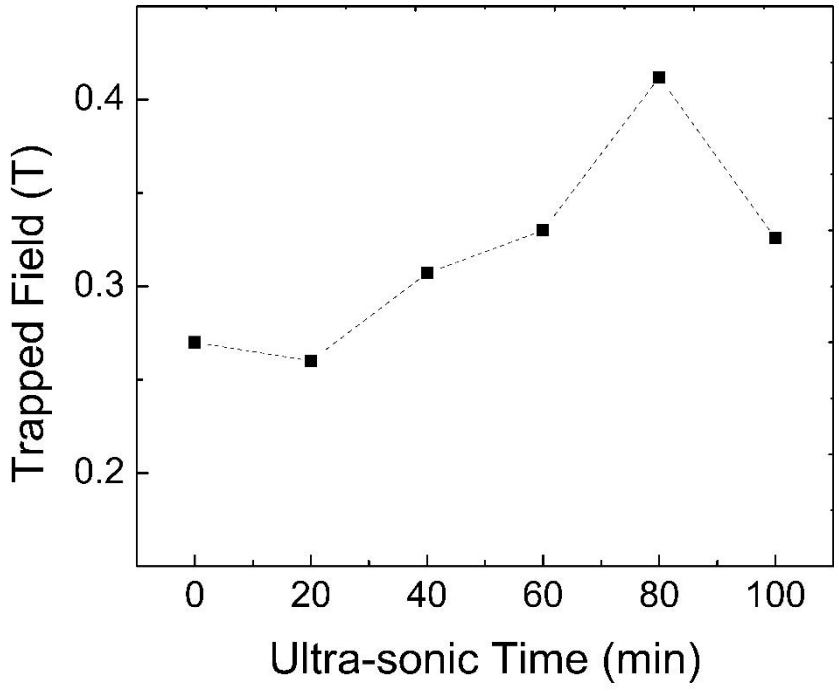

Figure 3.15 Trapped field values of Y-123 sample with PtO_2 addition under an applied magnetic field of 1 T at 77.3 K and 0.3 mm above the top surface as a function of ultra-sonication times

3.3.3 (c) Superconducting properties

The small pieces with dimensions of about 1.5x1.5x0.5 mm^3 were cut 2 mm under seed crystal along *c*-axis from YPt0, YPt40 and YPt80 samples. The temperature dependence of normalized dc susceptibility was estimated using SQUID magnetometer in both zero-field cooled (ZFC) and field cooled (FC). All samples exhibited a sharp superconducting transition around 91-93 K that implies. The YPt0 sample show s highest $T_{c,on\ set}$ at 92.8 K compare with samples YPt40 and YPt80. The $T_{c,on\ set}$ values are close to standard critical temperature value of bulk Y-123 superconductor [30]. The transition temperature width of YPt40 and YPt80 samples are wider than YPt0 sample as the ultra-sonicated time increase and less than 1.5 K as presented in Fig. 3.16, which indicates that all samples were high-quality. However, the YBCO bulk made from refined Y-211 showed a slight drop in superconducting transition temperature which is better than that of what we observed in samples prepared from ball-milled Y211powder [9, 35].

The critical current density (J_c) was calculated using the extended Bean's critical state formula for a rectangular sample. The highest self-field J_c value was observed in YPt80 sample that was around 47 kA/cm^2 and J_c at 1 T reached 10 kA/cm^2 at 77 K, higher than that of what the Y0 sample exhibited. The critical current density at self-field was showing an increment with increase in the ultra-sonication time, till 80 min. In addition, at high fields, we can see a peak effect which is proportional to ultra-sonication time. This result gets support from the very fine particles that regular particles bombard each other or shear along surfaces and also oxygen deficient in the structure. Detailed J_c profile can be seen in Fig. 3.17.

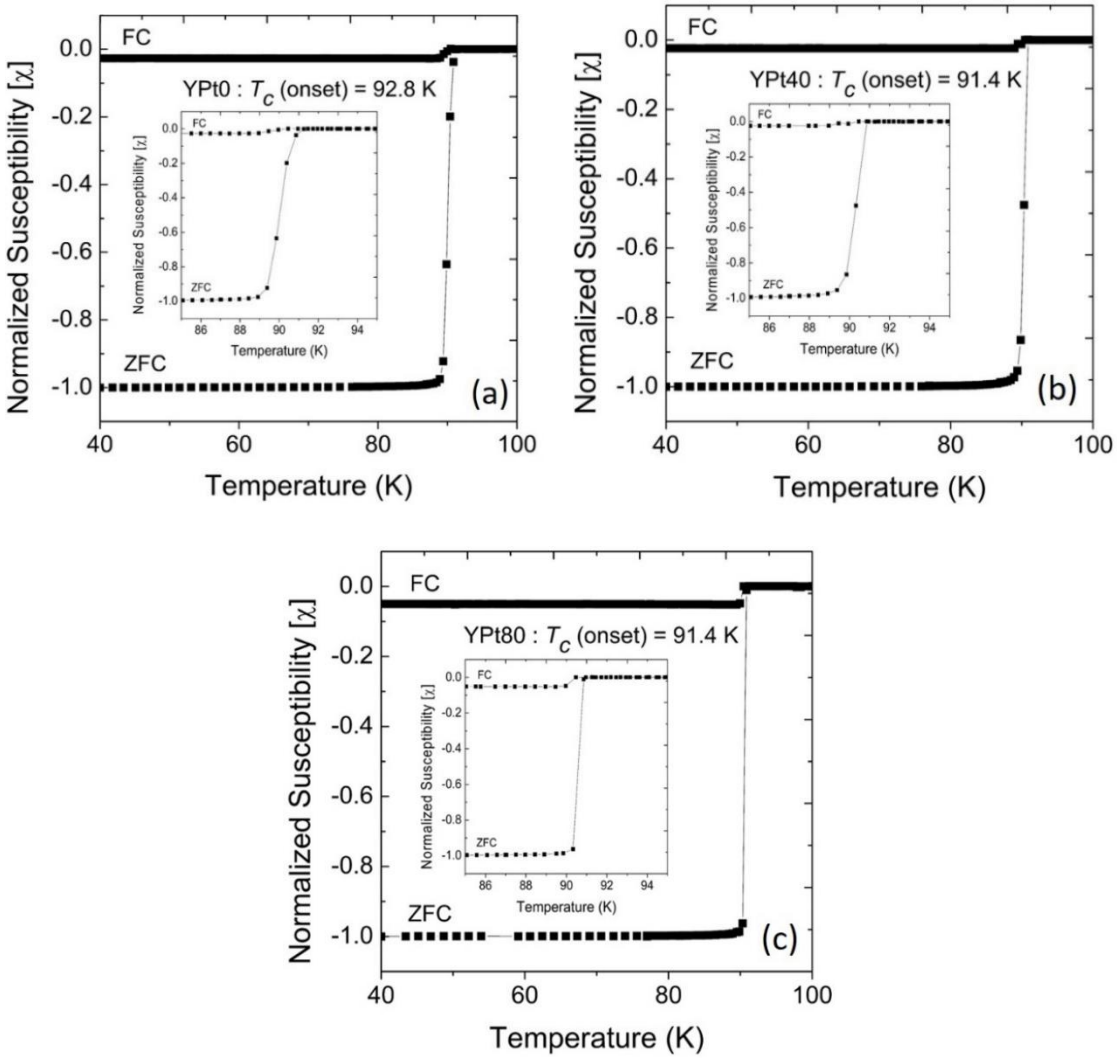

Figure 3.16 The temperature dependence of the normalized DC susceptibility measurements of (a) YPt0, (b) YPt40, and (c) YPt80 samples

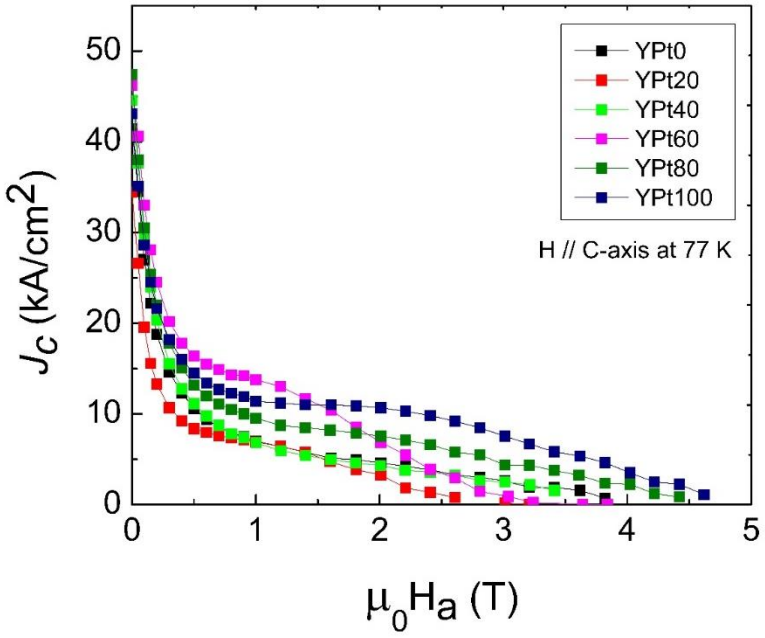

Figure 3.17 Field dependences of the critical current density (J_c) at 77 K, *H//c*-axis of Y-123 with PtO_2 addition samples

3.3.3 (d) Microstructure analysis

The microstructure of samples prepared with different ultra-sonicated Y-211 secondary phase particle embedded in the Y-123 matrix were analyzed by FESEM and particle size analysis from image processing system the results show in Figs. 3.18(a)-(b). Microstructure reveals that the Y-211 secondary phase particles were finely dispersed inside the Y-123 matrix of both ultra-sonicated and not ultra-sonicated samples. As observed Y-211 secondary phase particles in sample YPt0 were formed as large and irregular as shown in Fig. 3.18(a) with the average size of 2 and 4 µm and dispersed inhomogeneous. YPt80 sample show the Y-211 were finer and uniform in as depicted homogeneously in Fig. 3.18(b) with the average size 0.5-1 µm. the effect of ultra-sonication increases among of small particles resulted in a significant decrease of the average of the Y-211 secondary phase particle size in final samples. The

superconducting performance improvement as well as trapped field and critical current density enhancement in the ultra-sonicatedY-211 secondary phase based Y-123 bulk.

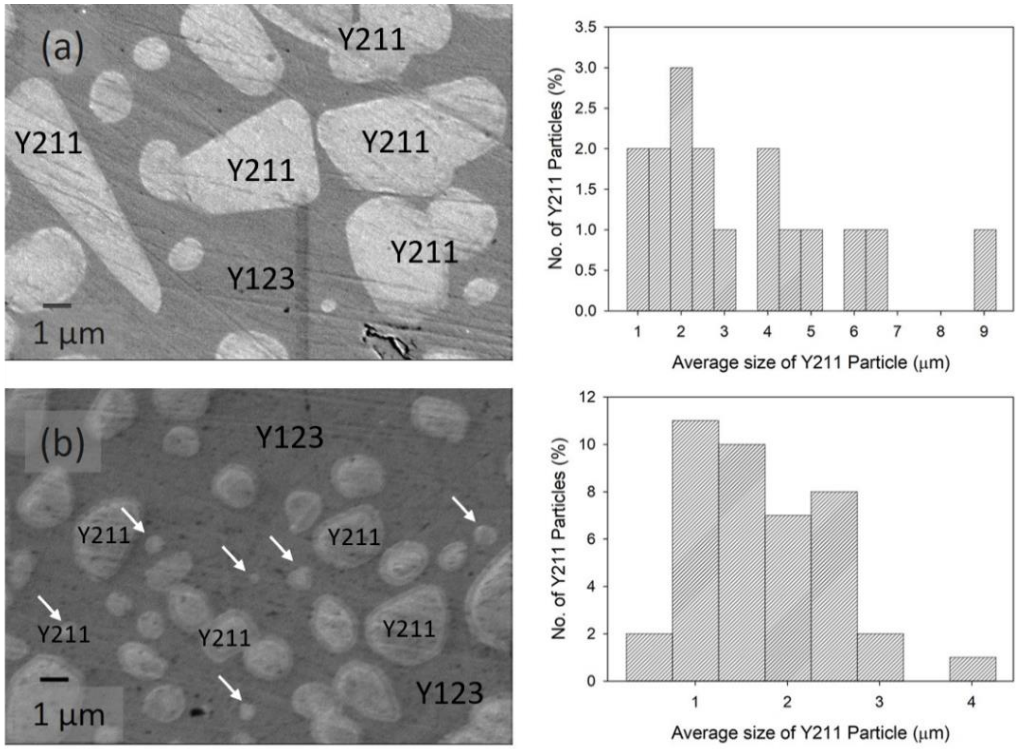

Figure 3.18 FESEM images of a) YPt0 and b) YPt100 samples

Among various durations, 80 minutes of ultra-sonication seemed to be the optimum for refining Y-211 powder based on the particles size and uniform shape of Y-211 powder. We have successfully prepared YBCO bulk consisting of Y-123 and Y-211 mixed in a molar ratio of 10:5 with 0.5 wt% Pt by TSMG processing. XRD clearly shows that all the bulk Y-123 samples have good texture and pure single grain nature. All samples exhibited superconductivity with $T_c \sim 92.8$ K and sharp superconducting transitions. The highest critical current density (J_c) was observed in 80-minute ultra-sonicated bulk which was measured to be 47 kA/cm^2 at self-field and 77 K. For the same bulk at 77.3 K, the trapped field measurements exhibited single uniform conical peak with the maximum value of 0.42 T at the center. SEM observations showed that the particle sizes of the most Y-

211 particles have reduced to 1-2 μm and uniformly dispersed within the final Y-123 matrix which led to improvement in the superconducting properties of bulk Y-123 superconductor. Results of J_c, T_c, trapped field value and refinement technique on bulk Y-123 superconductor are summarized in Table 3.1.

Table 3.1 Superconducting transition temperature, Critical current density (J_c) at self-field and 1T, trapped field at 77 K of the bulk Y-123 superconductor produced ultra-sonicated Y-211, compared to recent results reported in literature

Samples	Process	T_c and ΔT_c (K)	J_c at 77 K (kA/cm^2)		Trapp filed (T) at 77 K	Ref.
			Self-field	At 1 T		
Y-123 + Y-211 (Ultra-sonication, Y100 sample)	TSMG	91-92, 1.5	38	13	0.28 T (applied field 1 T)	Present work [20]
Y-123 + Y-211 + 0.5 wt% Pt (Ultra-sonication, YPt80 sample)	TSMG	92, 1	47	15	0.42 T (applied field 1 T)	Present work [21]
Y-123 + Y-211 (microemulsion technique) + 0.3 wt% Pt	TSMG	-	20	15	0.142 T (applied field 1.5 T)	[12]
Y-123 + Y-211 + 0.2 wt% Pt	TSMG	90, 4-5	28	14	-	[36]
Y-123 + Y-211 (solution blow spinning)	BA-TSMG	91, < 0.7	39	15	0.63 (applied field 1.4 T)	[13]
Y-123 + Y-211 (commercial powders)	IG	-	12	8.7	-	[37]
Y-123 + Y-211 + 0.5 wt% CeO_2	IG	89.5 – 91.5,	22	~ 0	-	[32]

3.3.4 Comparison of bulk Y-123 superconductors with and without PtO_2 addition

The ultra-sonication technique was employed to refine Y-211 particle [38]. The particle size of Y-211 as a function of ultrasonic time were displayed on Fig. 3.19. Majority of Y-211 particles were prepared as Y-211 powder were bigger than 5 µm (~48%) and also a few particles less than 2 µm (~7.5%). After we employed ultra-sonication, the Y-211 particles became smaller than before. With 40 minutes and 80 minutes of ultra-sonication, particles were less than 1 µm had been estimated to be 18.5% and 96.25%, respectively. For 80 minutes, the Y-211 particles were less than 500 nm estimated to be around 1.25%. The Y-211 particles were toning down with increasing ultra-sonication time as it can be seen in FESEM images on Fig. 3.20. The high energy wave from ultrasonic probe will disrupt segregated Y-211 particles into division of individual and small particles [16].

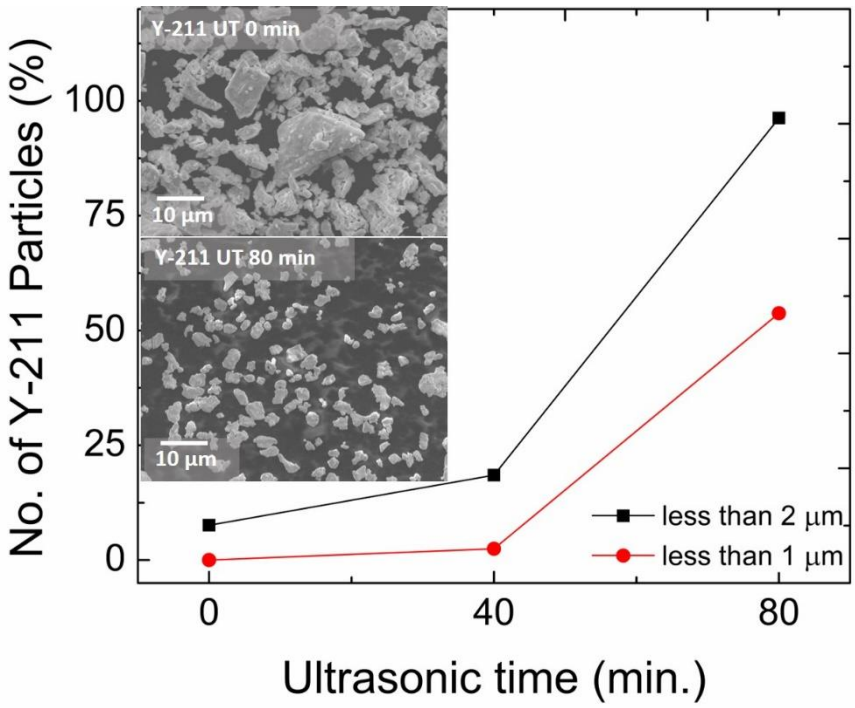

Figure 3.19 Average particles size of Y-211 powders as a function of ultra-sonic times along with inset FESEM images of Y-211 ultra-sonicated at 0 and 80 minutes

In this system, PtO_2 was considered as grain refiner and additive that improves superconducting properties of Y-123 bulk. For comparing the individual effects of ultra-sonication, we had synthesized bulk 123 samples with and without PtO_2 addition. After oxygenation of Y-123 bulks, trapped field distribution under an applied field of 1 T at 77.3 K at 0.3 mm above the top surface was measured with respect to ultrasonic time as shown in Fig. 3.20. The highest value was observed in sample with PtO_2 addition along with 80 minutes of ultra-sonicatedY-211 powder that had reached 0.42 T.

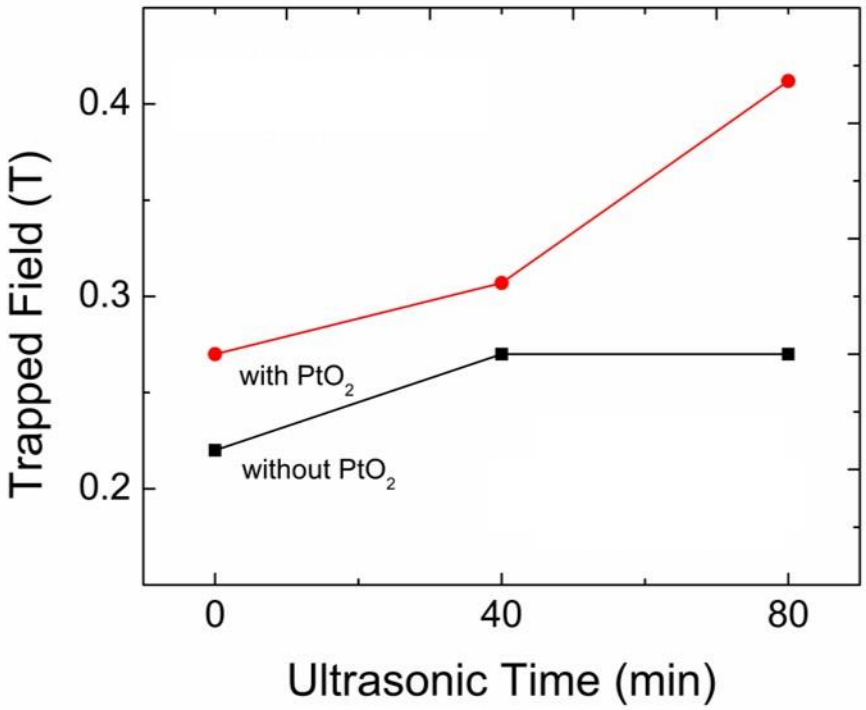

Figure 3.20 Trapped field value measured under a magnetic field of 1 T at 77.3 K as a function of ultra-sonic times

Fig. 3.21 shows superconducting transition temperature (T_c) of all samples exhibited $T_{c.onset}$ around 91 to 92 K with ΔT_c less than 1.5 K similar to nature of bulk Y-123 superconductors [30]. Critical current density (J_c) at 77 K (H//*c*-axis) shows higher value in sample with PtO_2 condition and Y-211 particles refined at 80 minutes of ultrasonic time.

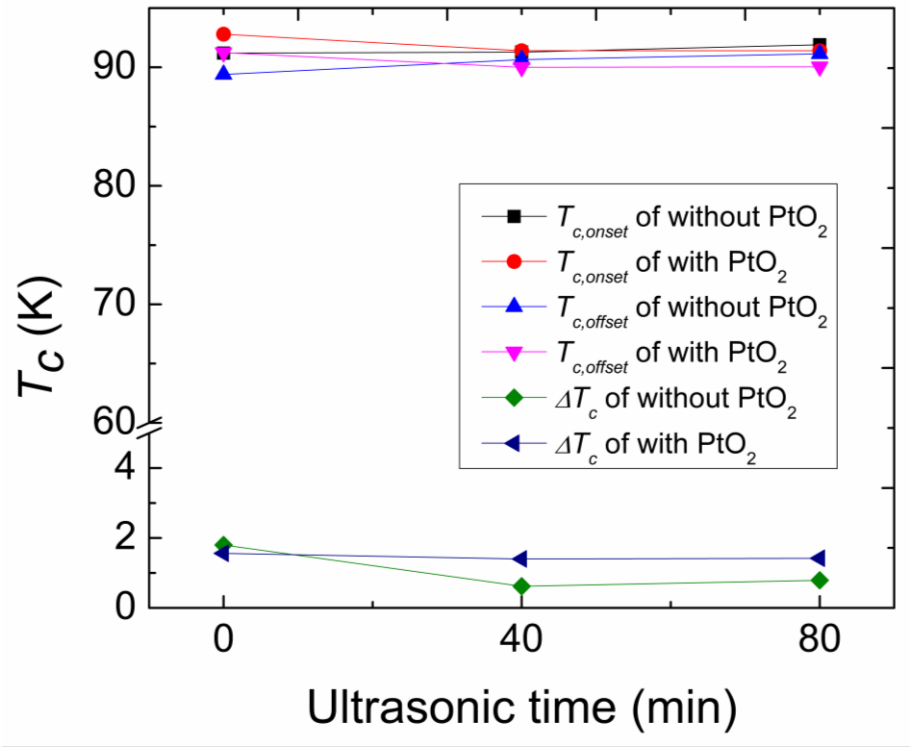

Figure 3.21 Critical temperature (T_c) as a function of ultra-sonic times

Fig. 3.22 shows J_c values as a function of ultrasonic time at self-field and 2 T at 77 K. High J_c, which is around 47.5 kA/cm^2 at self-field, was observed in the same sample similar to that of trapped fields results. In case of high field (2 T) J_c values, the samples exhibited very close performances both with and without PtO_2 added samples. Especially, the values were around 10 kA/cm^2 in 80 minutes. This indicates that for superior superconducting properties in bulk Y-123 superconductors, both PtO_2 addition as well as smaller initial Y-211 particles were crucial. The PtO_2 was observed for helping in containing/restricting sub micro size of Y-211 secondary phase in Y-123 matrix [10, 39]. From the present comparisons of superconducting performance, the highest value was exhibited in the sample with PtO_2 addition and Y-211 refined 80 minutes of ultra-sonication.

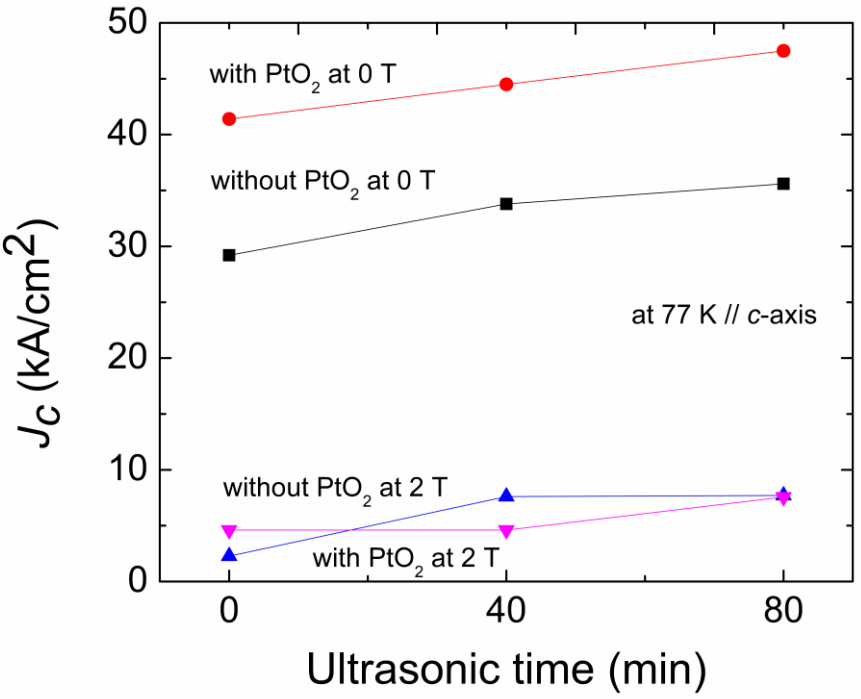

Figure 3.22 Critical current density (J_c) at 0 T and 2 T as a function of ultra-sonic times

3.4 Conclusions

In this chapter, an alternative ultra-sonication technique to refine Y-211 secondary phase particle was employed. We have presented the effect of ultra-sonication on particle size of Y-211 particles and superconducting properties of bulk Y-123 superconducting materials. Bulk Y-123 samples were fabricated by TSMG processing with and without PtO_2. The ultra-sonication technique appears to be an effective in refining the Y-211 secondary phase particles owing the evidence clearly shows the improvement of trapped field value and critical current density based on ultra-sonicatedY-211 particles at 80 minutes and PtO_2 addition condition. Compare with the ultra-sonication technique is a reliable applicable method to refine and control Y-211 particle size which is also quite a cost effective and a less contaminating in synthesizing bulk Y-123 superconductors. Moreover, ultra-sonication is reliable and reproducible because of the ability to control power and frequency precisely. The present work illustrates significant potential for batch

production of large single grain bulk Y-123 magnets for practical applications. Although the technique is robust.it can be further optimized via manipulating powder and frequency of ultrasonication.

References

1. Barna, D., *High field septum magnet using a superconducting shield for the Future Circular Collider*. Physical Review Accelerators and Beams, 2017. **20**(4): p. 041002.
2. Nakagawa, K., et al., *Study on Magnetic Drug Delivery System Using HTS Bulk Magnet.* IEEE Transactions on Applied Superconductivity, 2012. **22**(3): p. 4903804-4903804.
3. Durrell, J.H., et al., *Bulk superconductors: a roadmap to applications.* Superconductor Science and Technology, 2018. **31**(10): p. 103501.
4. Jin, S., et al., *High critical currents in Y-Ba-Cu-O superconductors.* Applied Physics Letters, 1988. **52**(24): p. 2074-2076.
5. Cardwell, D.A., *Processing and properties of large grain (RE)BCO.* Materials Science and Engineering: B, 1998. **53**(1-2): p. 1-10.
6. Murakami, M., *Melt Processed High-Temperature Superconductors*. Melt Processed High-Temperature Superconductors. 1992.
7. Muralidhar, M., M.R. Koblischka, and M. Murakami, *Embedding of 211 particles in NEG-123 superconductors.* Superconductor Science and Technology, 1999. **12**(8): p. 555.
8. Hamrita, A., et al., *Superconducting properties of polycrystalline $YBa_2Cu_3O_{7-d}$ prepared by sintering of ball-milled precursor powder.* Ceramics International, 2014. **40**(1, Part B): p. 1461-1470.
9. Muralidhar, M., et al., *Record critical current densities in IG processed bulk $YBa_2Cu_3O_y$ fabricated using ball-milled $Y_2Ba_1Cu_1O_5$ phase.* physica status solidi (a), 2016. **213**(2): p. 443-449.
10. Kim, C.-J., et al., *Role of PtO_2 on the refinement of Y_2BaCuO_5 second phase particles in melt-textured Y-Ba-Cu-O oxides.* Physica C: Superconductivity, 1997. **281**(2): p. 244-252.
11. Shlyk, L., et al., *Melt-processed YBCO with Pt or Ce additions: comparison of pinning behavior.* Physica C: Superconductivity, 2005. **423**(1): p. 22-28.

12. Li, F., et al., *Nanoscale Y_2BaCuO_5 particles for producing melt-textured YBCO large grains.* Superconductor Science and Technology, 2006. **19**(6): p. 589-595.
13. Rotta, M., et al., *Synthesis of Y_2BaCuO_5 nano-whiskers by a solution blow spinning technique and their successful introduction into single-grain, YBCO bulk superconductors.* Ceramics International, 2019. **45**(3): p. 3948-3953.
14. Nariki, S., et al., *Refinement of RE211 particles in melt-textured RE–Ba–Cu–O bulk superconductors.* Superconductor Science and Technology, 2002. **15**(5): p. 679.
15. Guangyin, Z. and Z. Youcai, *Chapter Five - Harvest of Bioenergy From Sewage Sludge by Anaerobic Digestion*, in *Pollution Control and Resource Recovery for Sewage Sludge*, Z. Guangyin and Z. Youcai, Editors. 2017, Butterworth-Heinemann. p. 181-273.
16. Qian, M., A. Ramirez, and A. Das, *Ultrasonic refinement of magnesium by cavitation: Clarifying the role of wall crystals.* Journal of Crystal Growth, 2009. **311**(14): p. 3708-3715.
17. Brennen, C.E., *Cavitation and Bubble Dynamics*. 2013, Cambridge: Cambridge University Press.
18. Bang, J.H. and K.S. Suslick, *Applications of Ultrasound to the Synthesis of Nanostructured Materials.* Advanced Materials, 2010. **22**(10): p. 1039-1059.
19. Franco, F., L.A. Pérez-Maqueda, and J.L. Pérez-Rodríguez, *The effect of ultrasound on the particle size and structural disorder of a well-ordered kaolinite.* Journal of Colloid and Interface Science, 2004. **274**(1): p. 107-117.
20. Pinmangkorn, S., et al., *Enhancing the superconducting performance of melt grown bulk $YBa_2Cu_3O_y$ via ultrasonically refined Y_2BaCuO_5 without PtO_2 and CeO_2.* Materials Chemistry and Physics, 2020. **244**: p. 122721.
21. Pinmangkorn, S., et al., *Effect of Ultra-sonicated Y_2BaCuO_5 on Top-Seeded Melt Growth $YBa_2Cu_3O_y$ Bulk Superconductor.* Journal of Superconductivity and Novel Magnetism, 2020: p. 1-7.
22. Chen, D.X. and R.B. Goldfarb, *Kim model for magnetization of type-II superconductors.* Journal of Applied Physics, 1989. **66**(6): p. 2489-2500.

23. Nariki, S., et al., *Processing of high-performance (Gd, Y)-Ba-Cu-O bulk superconductors with fine RE211 pinning centers.* IEEE Transactions on Applied Superconductivity, 2005. **15**(2): p. 3110-3113.
24. Muralidhar, M., et al., *Magnetic levitation in liquid oxygen and its applications.* Physica C: Superconductivity, 2004. **412-414**: p. 739-743.
25. Muralidhar, M., et al., *Vortex pinning by mesoscopic defects: A way to levitation at liquid oxygen temperature.* Applied Physics Letters, 2003. **83**(24): p. 5005-5007.
26. Foerster, C.E., et al., *Mechanical Properties of (RE)$Ba_2Cu_3O_{7-\delta}$ Superconductor With RE Obtained From Xenotime Mineral.* IEEE Transactions on Applied Superconductivity, 2011. **21**(2): p. 52-59.
27. Yeoh, W.K., et al., *Control of Y_2BaCuO_5 particle formation in bulk, single grain Y–Ba–Cu–O.* Superconductor Science and Technology, 2009. **22**(6): p. 065011.
28. Shi, Y.H., A.R. Dennis, and D.A. Cardwell, *A new seeding technique for the reliable fabrication of large, SmBCO single grains containing silver using top seeded melt growth.* Superconductor Science and Technology, 2015. **28**(3): p. 035014.
29. Koblischka-Veneva, A., et al., *Comparison of Temperature and Field Dependencies of the Critical Current Densities of Bulk YBCO, MgB_2, and Iron-Based Superconductors.* IEEE Transactions on Applied Superconductivity, 2019. **29**(5): p. 1-5.
30. Mahmood, A., Y.S. Chu, and T.H. Sung, *Enhancement of critical current density of liquid-infiltration-processed Y–Ba–Cu–O bulk superconductors using milled Y_2BaCuO_5 powder*. Superconductor Science and Technology, 2012. **25**(4): p. 045008.
31. Wen, H.h. and Z.x. Zhao, *Fishtail effect and small size normal core pinning in melt-textured-growth $YBa_2Cu_3O_{7-\delta}$ bulks.* Applied Physics Letters, 1996. **68**(6): p. 856-858.
32. Chen, S.-Y., et al., *Remarkable peak effect in $J_c(H, T)$ of Y–Ba–Cu–O bulk by using infiltration growth (IG) method.* Materials Science and Engineering: B, 2008. **151**(1): p. 31-35.

33. Koblischka, M.R., et al., *Analysis of pinning in $NdBa_2Cu_3O_{7-\delta}$ superconductors.* Physical Review B, 1998. **58**(5): p. 2863-2867.
34. Muralidhar, M. and M. Murakami, *Effect of matrix composition on the flux pinning in a (Nd,Eu,Gd)$Ba_2Cu_3O_y$ superconductor.* Physical Review B, 2000. **62**(21): p. 13911.
35. Muralidhar, M., et al., *Effect of nanoscopic ZrO_2 particles on flux pinning in (Nd,Eu,Gd)-123/Gd-211 composites.* Superconductor Science and Technology, 2004. **17**: p. 1129.
36. Jiao, Y.L., et al., *J_c–B characteristics for bulk single domain YBCO superconductors.* Physica C: Superconductivity, 2003. **386**: p. 266-270.
37. Mahmood, A., et al., *Pre-sintering effects on the critical current density of YBCO bulk prepared by infiltration method.* Physica C: Superconductivity, 2008. **468**(15-20): p. 1350-1354.
38. Pinmangkorn, S., et al., *Y_2BaCuO_5 Particle Size Control via Ultrasonication and its Effect on Bulk $YBa_2Cu_3O_y$ Superconductor.* IOP Conference Series: Materials Science and Engineering, 2020. **773**: p. 012017.
39. Chow, J.C.L., et al., *The influence of process parameters on the growth morphology of large-grain Pt-doped YBCO fabricated by seeded peritectic solidification.* Superconductor Science and Technology, 1997. **10**(6): p. 435-443.

Chapter 4

Development of Ternary Bulk $(Gd,Y,Er)Ba_2Cu_3O_y$ Superconductor

4.1 Introduction

Due to T_c lying above boiling point of liquid nitrogen (LN_2) and thus the ability to be cooled to the superconducting state by the cheap LN_2 instead of LHe, high-temperature superconductors (HTS), especially $(RE)Ba_2Cu_3O_y$ (RE means Y and/or rare earth element such as Gd, Er, Nd, Eu), have revolutionized the applicability of superconductivity in real life [1-5]. $(RE)Ba_2Cu_3O_y$ (RE-123) bulk superconductor has potential to be used in various engineering applications such as trapped field magnet for magnetic levitation, superconducting bearing, flywheel energy storage system, MRI, NMR, rotary motors etc. [1-5]. For that purpose, RE-123 bulk superconductors must be in the form of large single grain bulks to overcome the weak-link issue. For the above-mentioned applications,

trapped field is the most relevant parameter. It is directly related to critical current density (J_c) and diameter of the bulk [6-8]. In the current research, we focus on developing large single-grain bulk superconductors capable of trapping much higher magnetic field than conventional hard ferromagnets.

Various techniques have been utilized to fabricate single-grain (RE-123) bulks. For example, top seeded melt growth (TSMG) [7, 8], oxygen-controlled melt growth (OCMG) [9], and the latest method of infiltration growth (IG). TSMG process uses the peritectic solidification of the RE-211 phase and liquid phase (Ba-Cu-O) to form the single-grain RE-123 phase. The process proceeds at around 1000-1100°C, above the peritectic temperature, T_p, of the RE compound. During the following cooling, RE-123 matrix crystallizes with leaving microscopic RE-211 precipitates trapped in the RE-123 matrix. These RE-211 particles act as pinning centers, provided they are small and uniformly distributed in the RE-123 matrix. However, due to the incomplete peritectic reaction between RE-211 and liquid, unreacted large RE-211 particles along with pores, liquid segregation at grain boundaries, and cracks are formed, not desired in the final microstructure [9-13]. OCMG process is another technique designed for fabrication of LRE-123 superconductors, where oxygen amount is reduced, e.g. using a specific mixture of argon and oxygen gas continuously flowing in the process [14, 15]. This method is used to avoid substitution of LRE ions to Ba sites in the RE-123matrix that in an excessive amount reduces T_c of the final product. On the other hand, in a proper low concentration, this compositional fluctuation represents an arbitrary point-like defect disorder contributing to improvement of high field performance of bulk superconductor. Both these techniques are based on melt growth and thus are related to a peritectic reaction. Therefore, liquid losses appear in both and this leads to formation of numerous microstructural defects such as cracks, pores, inhomogeneous RE-211 distribution, shrinkage etc. To avoid the problems with liquid loss in MG based techniques, IG has been recently developed for fabrication of large bulk superconductors. In this technique, a RE-211 preform pellet is placed on the top of liquid phase preform, where it infiltrates into RE-211 preform and forms RE-123 matrix at peritectic temperature of the liquid

phase, which is lower than that of RE-211. Therefore, during the process, RE-211 retains in the solid form and reacts with Ba-Cu-O liquid phase to form RE-123 matrix. Nd-123 seed crystal is used to prevent a heterogeneous grain nucleation. The single grain RE-123 matrix grows by slow cooling from the seed crystal. This technique attains a uniform distribution of the RE-211 particles in the matrix, leads to pore reduction, and avoids shrinkage during the process. In the IG samples, fine RE-211 particles are trapped in the RE-123 matrix and a lower porosity than TSMG samples is observed [16-19]. To summarize, IG technique produces RE-123 bulks without inhomogeneities, it can be performed in air and therefore it can scale up to industrial level and help thus to the employment in various applications.

For improvement of superconducting properties, the interest has shifted from single element, such as Y-123, Gd-123, etc. bulk systems to binary and ternary systems of RE elements, such as (Y,Gd)-123, (Y,Sm)-123, (Nd,Eu,Gd)-123, (Nd,Sm,Gd)-123, (Sm,Eu,Gd)-123 [17, 20-24]. In case of a mixed RE system, RE site in the RE-123 is occupied by various RE elements, which causes a compositional inhomogeneity resulting in a significant enhancement of the superconducting properties. The differential RE elements distribution enables a significant enhancement of high field pinning and J_c [25]. The mixed binary RE system such as (Y,Gd)-123 showed higher J_c and trapped field values than single-element systems (Y-123 and Gd-123) [26, 27]. So far, the (Nd,Eu,Gd)-123 bulk superconductor prepared via OCMG keeps record in the self-field J_c, irreversibility field over 14 T at 77 K, and shows secondary peak effect at 4.5 T (by around 70 kA/cm^2 higher than Y-123 system at self-field). Nanometer-scale correlated pinning centers in the form of a lamellar nanostructure was created [22] in (Nd,Eu,Gd)-123 due to a proper ratio of individual rare earths. This type of nanostructure was exceptionally effective at high magnetic fields and significantly enhanced irreversibility field [23, 28]. In (Nd,Eu,Gd)-123 and (Sm,Eu,Gd)-123 systems, a positive effect of small Gd-rich secondary phase particles in the final microstructure was observed. Therefore, the proper amount of Gd-211 in the precursor was studied [29]. This research on ternary systems lead

us to the understanding that a low melting liquid phase in the preform can produce small RE-211 particles in the RE-123 matrix that are very effective flux pinning centers.

So far, several groups have studied mixed systems using IG process, however not many reports can be found on ternary systems. In this work, we performed a systematic study of the ternary mixed RE elements system (Gd,Y,Er) prepared by top seeded infiltration growth (TSIG) in air (to enable cheap processing unlike OCMG), which has not been studied until now. Further, we employed Er-123 (one of the lowest melting point RE-123 phases) as a part of precursor and probed the effectiveness of employing excess Er component in the ternary system. We optimized the composition of $(Gd_{0.33}Y_{0.33-x}Er_{0.33+x})$-123 bulk by varying ratio of Y and Er in the RE-211 preform. A thorough microstructural analysis was executed to study formation of Gd-211, Y-211, Er-211, and combination of these secondary phases along with measurement of electromagnetic and superconducting properties such as trapped field, critical current density and critical temperature.

4.2 Experimental details

To study the effect of RE elements on (Gd,Y,Er)-123 bulk superconductors, the secondary phase preforms were prepared via mixing the calcined Gd-211, Y-211, and Er-211 powders weighted in molar ratio of Gd-211 : Y-211 : Er-211 = 0.33 : 0.33-X : 0.33+X, where x = 0, 0.05, 0.1, 0.15, and 0.2, and 0.5 wt% PtO_2. The bulks are labelled as X0, X0.05, X0.1, X0.15, and X0.2 in accordance with X value, respectively. For optimization of temperature and time of IG process, differential thermal analysis (DTA) of $(Gd_{0.33},Y_{0.33-x},Er_{0.33+x})Ba_2Cu_3O_y$, [(Gd,Y,Er)-123], where X = 0, 0.05, 0.1, 0.15, and 0.2 in air were examined. The peritectic temperature (T_p) of each (Gd,Y,Er)-123 system was necessary to determine Fig. 4.1 shows the DTA analysis of $((Gd_{0.33},Y_{0.33-x},Er_{0.33+x})Ba_2Cu_3O_y)$, where x is 0, 0.05, 0.1, 0.15, and 0.2. DTA analysis revealed that the peritectic temperatures (T_p) of all the Er excess compositions are very close (around 1017°C), however slightly lower than X=0 (1018°C). This was expected as we added more Er-123 which has the lowest peritectic temperature, 990°C, compared to Gd-123 (1030°C) and

Y-123 (1005°C) [30, 31]. Hence, based on the DTA analysis, we concluded the growth temperature of all (Gd,Y,Er)-123 systems should be the highest T_p of all compositions, i.e. 1018°C.

The calcined powders were prepared similarly with previous work [32, 33]. Liquid phase (LP) preform was made up of Er-123 and $Ba_3Cu_5O_8$ mixed in 1:1 ratio. The mass ratio of secondary phase and LP preforms was maintained at 1:1.4. The preforms were prepared by pelletizing the mixtures by pressure of 20 kN in a 20 mm diameter die using a hydraulic press. The secondary phase preform was placed on the LP preform. After that, Nd-123 seed was placed at the top center of the secondary phase preform. The liquid phase preform was supported by Y_2O_3 and MgO single crystals to prevent liquid loss of LP during processing for achieving single-grain growth as shown in Fig 4.2(a).

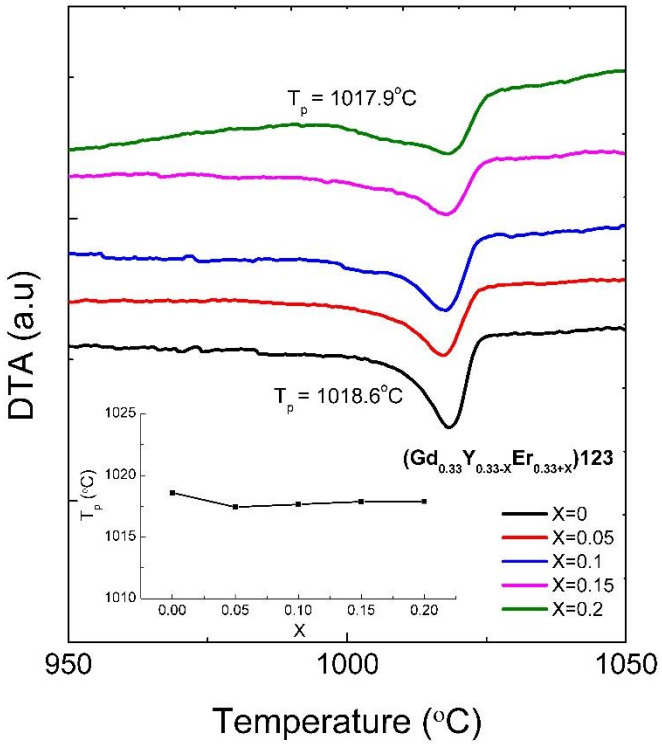

Figure 4.1 DTA results of $(Gd_{0.33}Y_{0.33-X}Er_{0.33+X})$-123 powders.

In detail, the temperature profile was depicted in Fig. 4.2 (b). The grown samples were oxygen annealed for 400 h at 500-375°C in oxygen flow rate 0.3 l/min. To investigate the superconducting phase, X-ray diffraction (XRD) was recorded. Later, superconducting properties such as the trapped field (TF), superconducting transition temperature (T_c), and critical current density (J_c) were estimated based on the extended Bean critical state model [34, 35]. To support the mechanisms behind the presented results, microstructural analysis was studied using field-emission scanning electron microscope (FESEM). The chemical composition was analyzed by energy dispersive x-ray spectroscopy (EDX).

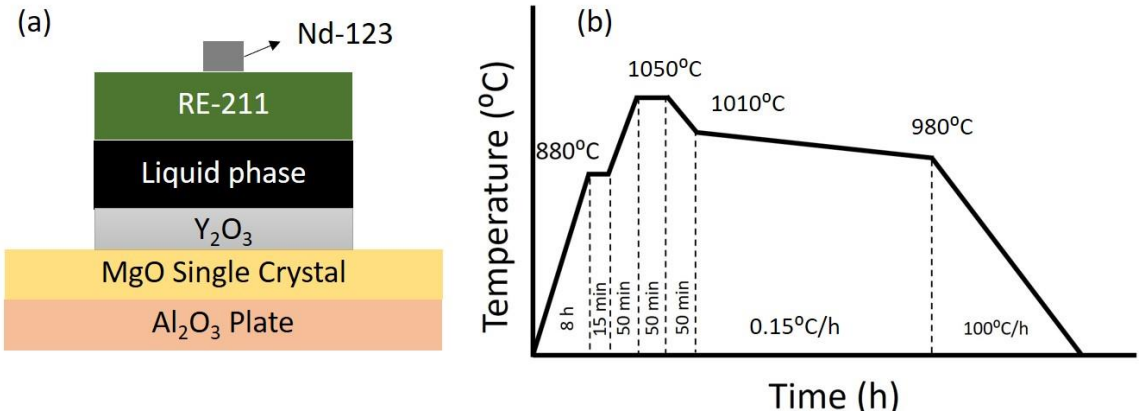

Figure 4.2 (a) Sample assembly, and (b) temperature and time program for fabricate $(Gd_{0.33}Y_{0.33-x}Er_{0.33+x})$-123 samples

4.3 Results and discussion

All samples showed a complete grain growth when heat-treated using the above-mentioned temperature profile (Fig. 4.2(b)). The photographs of completely grown bulk samples of 20 mm diameter can be seen in Figs. 4.3(a-e). These photographs demonstrate the main advantage of IG process, absence of any shrinkage in the final product. It stands in contrast to the conventional melt growth (MG) process leading to a shrinkage because of a liquid phase outflow. The evolution of gases during the decomposition and the corresponding porosity are avoided as well [36]. The four-fold facet growth from seed at the center on the top surface expands up to the edge of the sample in *ab* plane and a good

growth along *c*-axis can also be seen in all the bulks. Therefore, all the samples have been successfully prepared in air by IG process without any spontaneous nucleation. This gives evidence of a single-grain nature of these bulk superconductors. Fabrication of bulk (Gd,Y,Er)-123 superconductors with a slight excess in Er-concentration does not face any difficulties when using the same heat pattern.

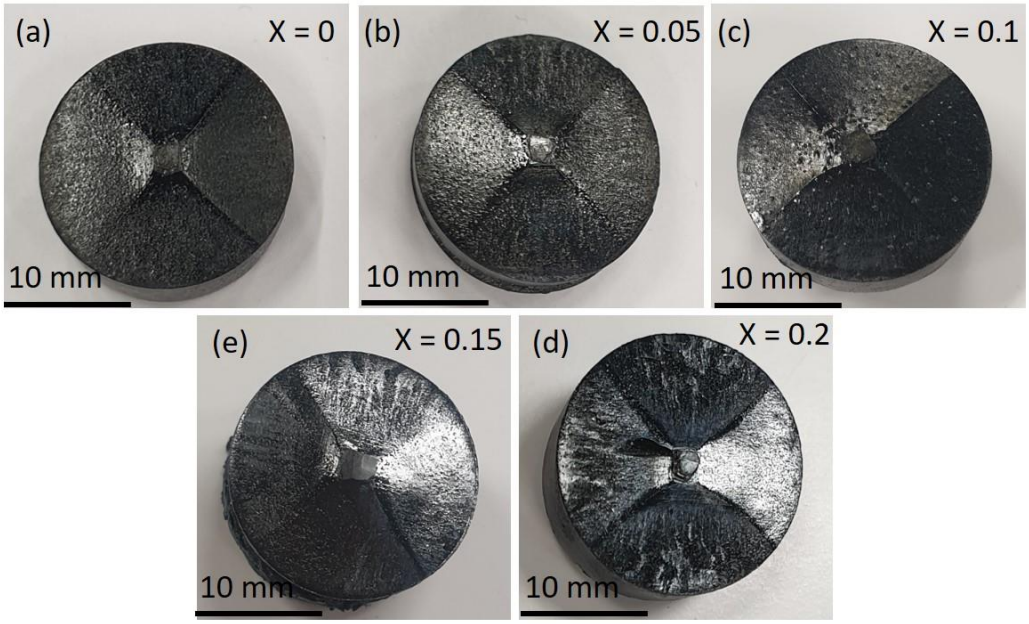

Figure 4.3 ($Gd_{0.33}$,$Y_{0.33-X}$,$Er_{0.33+X}$)-123 single grains growth samples (20 mm in diameter)

4.3.1 X-ray diffraction

The bulk (Gd,Y,Er)-123 superconductors with different Er concentration were investigated by XRD measurements to characterize the phases present in the bulk. The XRD diffraction patterns of all the samples are displayed in Fig. 4.4. The characteristic peaks corresponding to (*00l*) reflections of planes perpendicular to *c*-axis of the single crystal indicate that all samples possess orthorhombic structure of RE-123 [32, 37]. These data indicate that the Gd-211, Y-211, Er-211 powders are of high quality and the temperature and time employed for IG process and oxygen treatment for (Gd,Y,Er)-123 samples were well chosen.

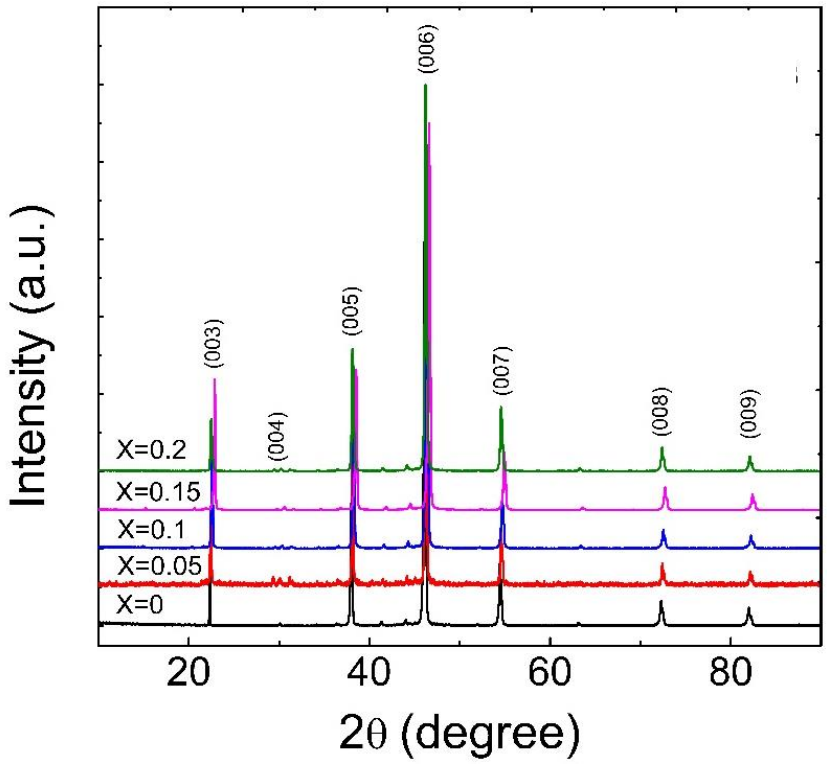

Figure 4.4 X-ray diffraction patterns for ($Gd_{0.33}$,$Y_{0.33-X}$,$Er_{0.33+X}$)-123 samples.

4.3.2 Superconducting properties

The perfect single-grain growth of a bulk sample reflects in the trapped field performance. The trapped field distribution of the (Gd,Y,Er)-123 samples was measured at liquid nitrogen temperature (77.3 K) in two applied fields of 0.45 T and 1 T directed parallel with *c*-axis. The TF value was measured by automatic Hall probe scanning 0.3 mm above the top surface (direct contact) to determine the maximum TF value and 1.3 mm above top surface to measure TF distribution profile. Figs. 4.5 (a-e) show the TF distribution profiles and contour maps of X0, X0.05, X0.1, X0.15, and X0.2 magnetized by applied magnetic field of 1 T. The peak TF values at 0.3 mm were 0.32, 0.38, 0.52, 0.50, and 0.52 T, respectively, while the maximum TF values at 1.3 mm were 0.22, 0.28, 0.40, 0.39, and 0.43 T, respectively. All TF profiles were uniform single peaks, with maximum at the center, indicating that all the samples were single grains, sufficiently oxygenated, without large cracks. These results show high quality of IG processed bulk (Gd,Y,Er)-123. Fig.

4.6 shows the comparison of TF values of all the bulks measured 0.3 mm above the top surface at the applied magnetic fields of 0.45 and 1 T. In both 0.45 and 1 T, maximum TF value was observed in X0.2 sample, 0.38 T and 0.52 T, respectively. The TF value of sample X0.2 is almost twice that of X0, which shows the effect of high Er concentration on bulk $(Gd_{0.33}Y_{0.33-x}Er_{0.33+x})$-123 samples.

These results also point out to high quality IG processed bulk fabrication. The present TF values are superior when compared to previous high TF values reported by Y. Shi et al in TSMG processed binary mixed (Y,Gd)-123 system with 30 mm diameter, which was around 0.3-0.35 T when magnetized to 1.4 T at 77.3 K [26]. The maximum TF value of (Gd,Y,Er)-123 prepared by IG in air was slightly lower than that of (NEG)-123 fabricated by OCMG process with 30 mm diameter reported by Muralidhar et al., around 0.1 T at 77 K, with the applied magnetic field 1 T [38].

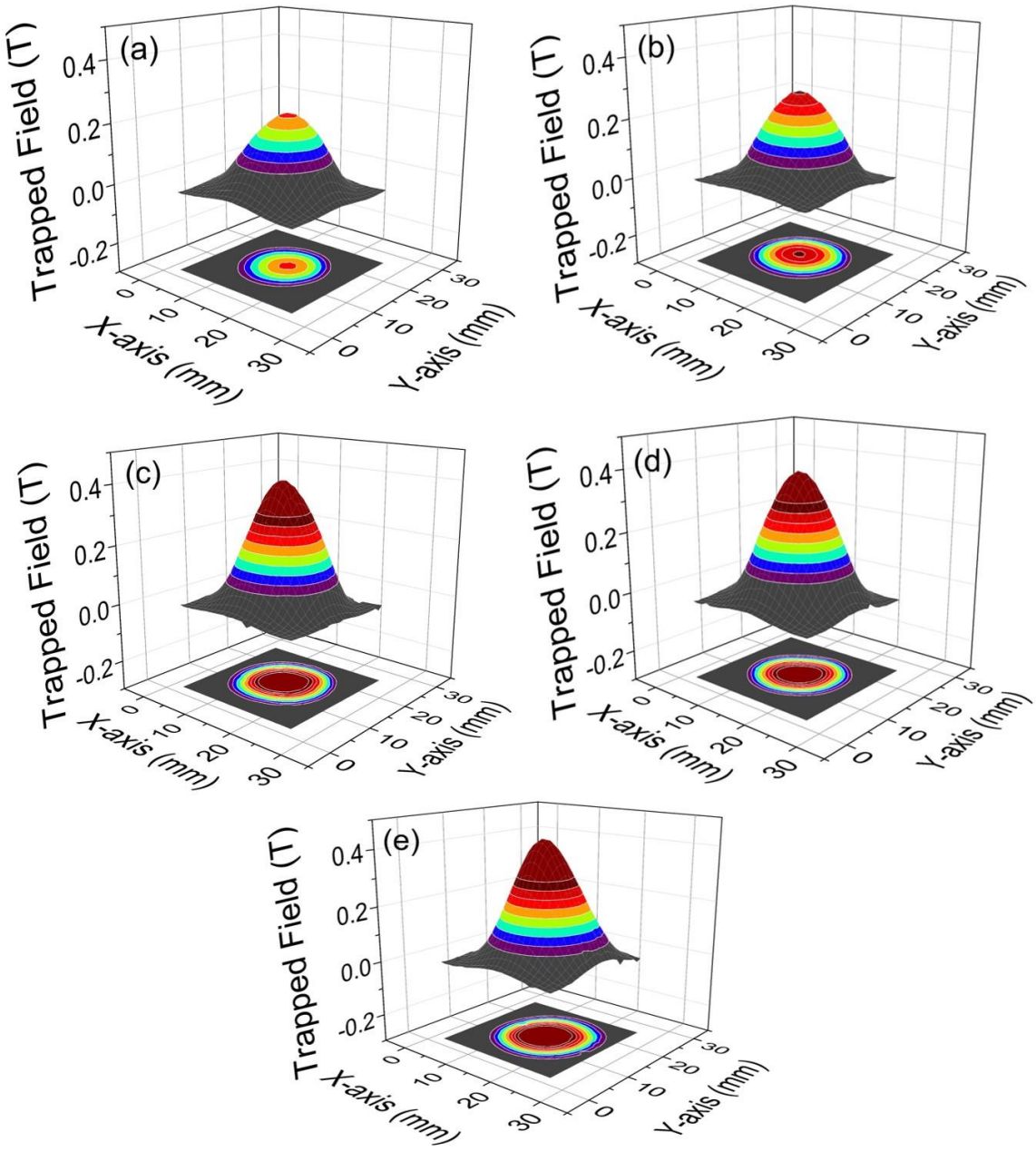

Figure 4.5 The trapped field distribution of (a) X0, (b) X0.05, (c) X0.1, (d) X0.15, and (e) X0.2 sample under an applied magnetic field 1 T at 77.3 K and 1.3 mm above top surface

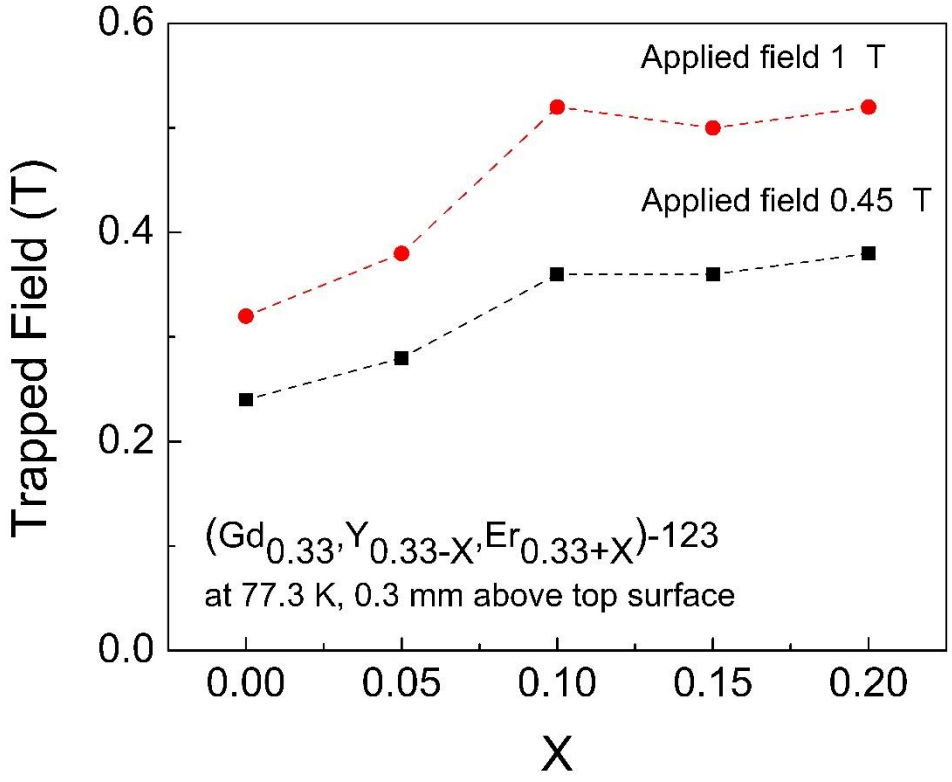

Figure 4.6 Trapped field values under an applied field 1 and 0.5 T at 77.3 K as a function of X for $(Gd_{0.33},Y_{0.33-X},Er_{0.33+X})$-123 samples

Fig. 4.7 shows temperature dependences of DC magnetic susceptibility in zero field cooled (ZFC) regime and following magnetic field 1 mT application along *c*-axis for the (Gd,Y,Er)-123 samples. It is clear that all the bulk (Gd,Y,Er)-123 samples exhibited the superconducting transition temperature ($T_{c,onset}$) at around 91.05 to 92 K. The superconducting transition width (ΔT_c), defined as the temperature difference between $T_{c,onset}$ and 90% of the T_c ($T_{c,offset}$), was less than 1 K. The T_c and ΔT_c results were similar to those reported for RE-123bulks, such as Gd-123 (T_c over 90 K) , Y-123 (T_c ~ 90-93 K), Er-123 (T_c ~ 90-93 K), (Gd,Y)-123 (T_c ~ 90-91 K), and (NEG)-123 (T_c ~ 93-93.9 K) [26, 32, 38-41]. No single or multiple RE group exhibited $T_{c,onset}$ higher than 90 K. The shape of superconducting transition curve did not change with varying Er and Y concentrations in the initial composition of (Gd,Y,Er)-123 system.

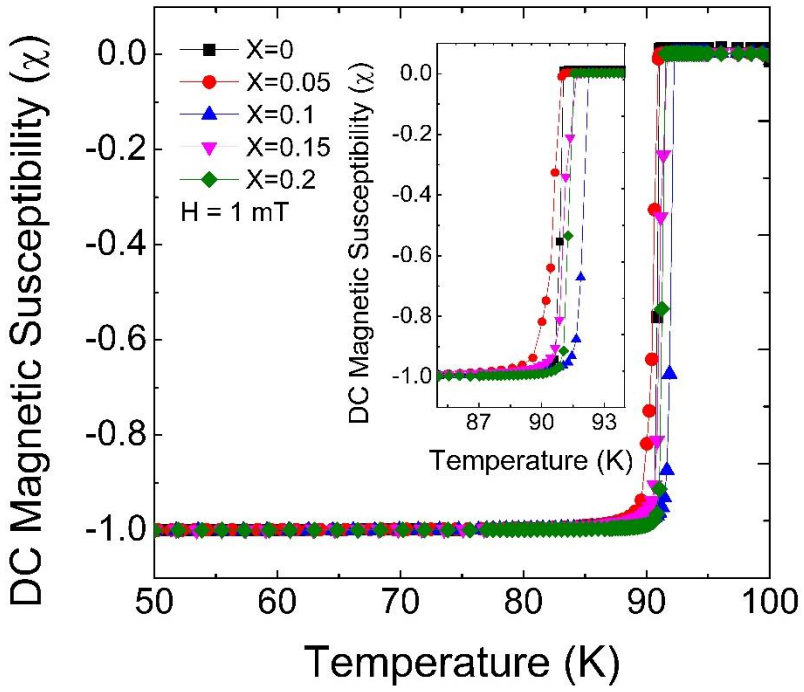

Figure 4.7 The temperature dependence of DC magnetic susceptibility measurements for $(Gd_{0.33},Y_{0.33-X},Er_{0.33+X})$-123 samples

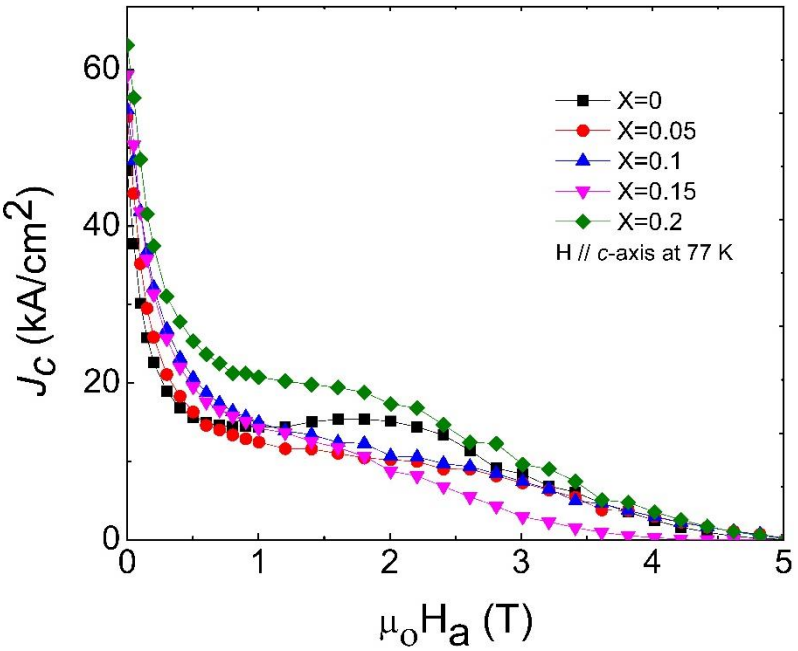

Figure 4.8 J_c values at 77 K, H // *c*-axis of $(Gd_{0.33},Y_{0.33-X},Er_{0.33+X})$-123 samples

Fig. 4.8 shows the field dependences of J_c for all the (Gd,Y,Er)-123 samples with different amounts of Er and Y obtained with SQUID. The *M-H* loops were measured at 77 K and J_c was calculated using the extended Bean model. The highest Er concentration in X0.2 sample showed the highest J_c values at 77 K (H// c-axis), 63.05 kA/cm^2 and 20.74 kA/cm^2 at self-field and 1 T, respectively. The J_c value of this system is higher than in (Y,Gd)-123 and Y-123 samples processed by IG process as reported by Das et al., where the highest J_c of around 47.8 kA/cm^2 was obtained at self-field and 77 K [42]. The J_c values of the (Y,Gd)-123 sample produced by TSMG process, and of (Nd,Sm)-123, (Sm,Eu)-123, and (Sm,Gd)-123 processed by OCMG in 0.1% O_2 + 99.9% Ar atmosphere reported by T. Saitoh et al. were less than 50 kA/cm^2 at 77 K, self-field [43]. On the other hand, ternary systems, like (Nd,Eu,Gd)-123 and (Sm,Eu,Gd)-123, processed by OCMG showed superior J_c values [29]. Excess of Gd-211 resulted in additional enhancement [44]. Similar results were observed in our system as well, with increase of Er content in the precursor. This is mainly due to the low T_m of Er-123.

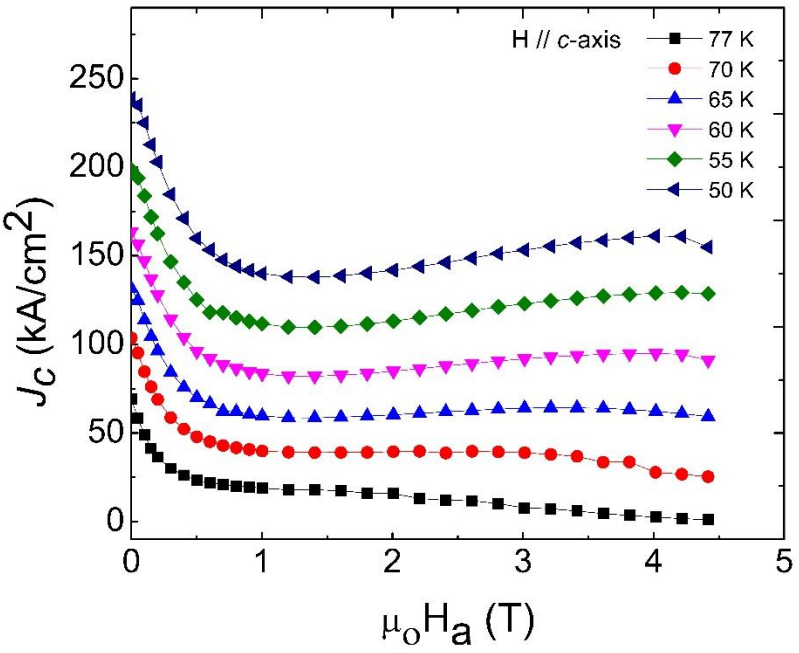

Figure 4.9 J_c values at 77, 70, 65, 60, 55, and 50 K, H // *c*-axis of ($Gd_{0.33}$,$Y_{0.13}$,$Er_{0.53}$)-123, (X = 0.2) sample

To confirm the suitability of X0.2 bulk for various applications, we estimated J_c at various temperatures. The J_c values at 50, 55, 60, 65, and 70 K at self-field were 238.86, 198.49, 163.63, 131.50, and 103.66 kA/cm^2, respectively, as shown in Fig. 4.9. Even at high field (4 T) and 50 K, J_c as high as 161.18 kA/cm^2 was observed. These results proved that the IG processed (Gd,Y,Er)-123 samples can be used also for high field applications at low working temperatures.

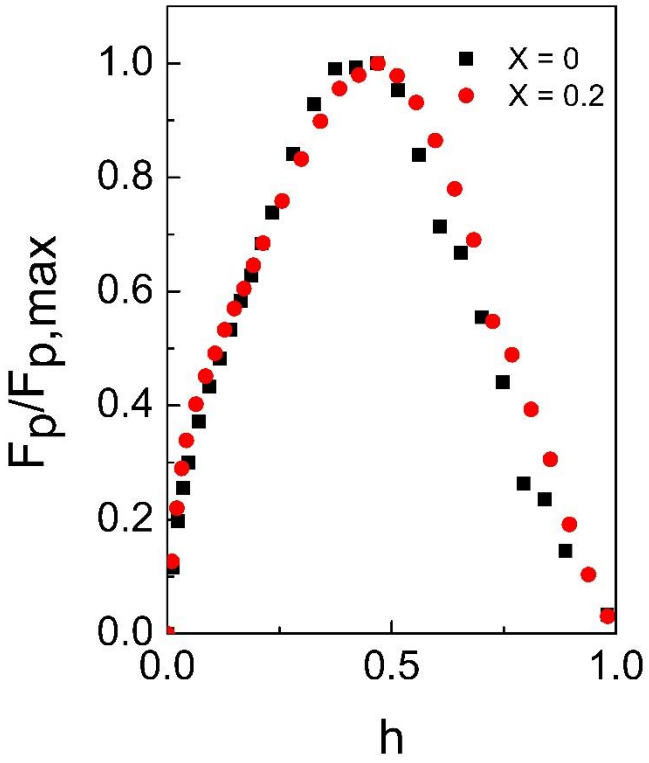

Figure 4.10 The normalized pinning force, $F_p/F_{p,max}$, as a function of the reduce field, h = H_a/H_{irr} for ($Gd_{0.33}$,$Y_{0.33-x}$,$Er_{0.33+x}$)-123 samples

To determine the prevailing pinning mechanism in the (Gd,Y,Er)-123 samples, we plotted the flux pinning diagrams known also as *f* vs *h* plots. Here $f = F_p/F_{p,max}$ and $h = H_a/H_{irr}$, where H_a is the applied field, H_{irr} is the irreversibility field determined as the field where J_c reached 100 A/cm^2. Pinning force density, F_p, is $F_p = J_c \times B$ and $F_{p,max}$ is pinning force density maximum. The model expression of pinning function is $f = Ah^p(1-h)^q$, where p and q are the characteristic pinning parameters. The peak position of the plot is then h_{max}

= $p/(p+q)$ [45]. Dew Hughes model ascribes different peak positions to different prevailing pinning mechanisms. For instance, if h_{max} ~ 0.2 the primary pinning is from grain boundaries, (e.g. the MgB_2 system) [46]. If h_{max} ~ 0.3, the majority of pinning is from normal conducting particles and obstacles, and h_{max} ~ 0.5 indicates pinning from δT_c phases, which can be usually observed in the mixed RE-123systems [42] (e.g. δT_c phases in Nd-123 single crystal that exhibited the enhanced fishtail effect [47]). In our case, we observed that the peak position of (Gd,Y,Er)-123 samples in flux-pinning diagrams was close to 0.4 as shown in Fig. 4.10. This indicates that the major pinning is from δT_c phases, similar to what was observed in (Nd,Sm,Gd)-123 and (Sm,Eu,Gd)-123 bulk superconductors [48]. Elsewhere, pinning from chemical composition fluctuation of matrix in the mixed (Y,Gd)-123 system resulted in peak position at more than 0.4 [42]. These chemical fluctuations cause phases with fluctuating critical transition temperature that resulted in δT_c pinning. Although in all these systems with h_{max} positioned around 0.5, the major pinning is from such δT_c phases, one should not ignore the normal pinning (δl) from 211 secondary phase. Hence, for enhancement of flux pining it is also important to control the secondary phase. Usually, one can achieve refinement of secondary phase via doping refining agents such as PtO_2 or ZrO_2 into the precursor and improve flux pinning performance [24, 47, 49]. In the current system, high h_{max} is a result of effective pinning from δT_c pinning and also δl from fine secondary phase.

4.3.3 Microstructure analysis

Figs. 4.11 (a-j) are the FESEM micrographs of the bulk samples X0, X0.05, X0.1, X0.15, and X0.2, respectively, which depict the (Gd,Y,Er)-211 particles along with the size analysis plotted as histograms. The (Gd,Y,Er)-211 particles size was estimated by *ImageJ* software. The size of the RE-211 particles present in the matrix ranged over a few micrometers. The distribution of RE-211 particles is much more uniform in X0.1, X0.15, and X0.2 samples than in X0 and X0.05, as show in Figs. 4.11 (f-j). The X0 sample showed large (Gd,Y,Er)-211 particles with average size 3-6 μm and smaller particles with

average size 0.75 – 1 μm with concentrations up to 13% and 46% of (Gd,Y,Er)-211 particles, respectively. The concentrations of (Gd,Y,Er)-211 particles with sizes less than 1 μm in X0.05, X0.1, X0.15, and X0.2 bulks were 38.18%, 51.85%, 60.14%, and 63.81%, respectively. Further, RE-211 particles with extremely small sizes such as 250-500 nm were also observed. The large particles were rod-like in shape, while the small ones were nearly spherical. Similar microstructures were observed in (Y,Gd)-123 bulks fabricated by TSMG process, with variation in shape (long rod and round) and size (large and small) of secondary particles [26, 50]. Small pores, cracks, and areas lacking liquid due to a liquid loss were also observed in our samples akin to previous reports of single element (Y-123) and mixed elements ((Y,Sm)-123) IG processed systems [21]. Even though, porosity can be controlled by sintering the 211 preform or by using finer RE-211 powder, the pores cannot be eliminated completely [51, 52]. The (Gd,Y,Er)-211 small particle count started growing with increase in Er-211 concentration, as shown on the histogram in Figs.11 (f-j). Hence, the high trapped field and J_c values of this system can be explained by increasing number of small secondary phase precipitates in the matrix with increasing Er-211 concentration in the RE-211 preform.

To confirm the chemical composition of matrix and secondary phase, EDX analysis was performed. Figs. 4.12(a) and (b) show the areas scanned on X0 and X0.2 samples, respectively, where the matrix is dark and secondary particles are bright. The spots 1, 2, and 3 in X0 sample correspond to large rod-like shaped secondary phase, while 4 is a large spherical 211 particle and 5 is a small spherical 211 particle. The compositional ratio of

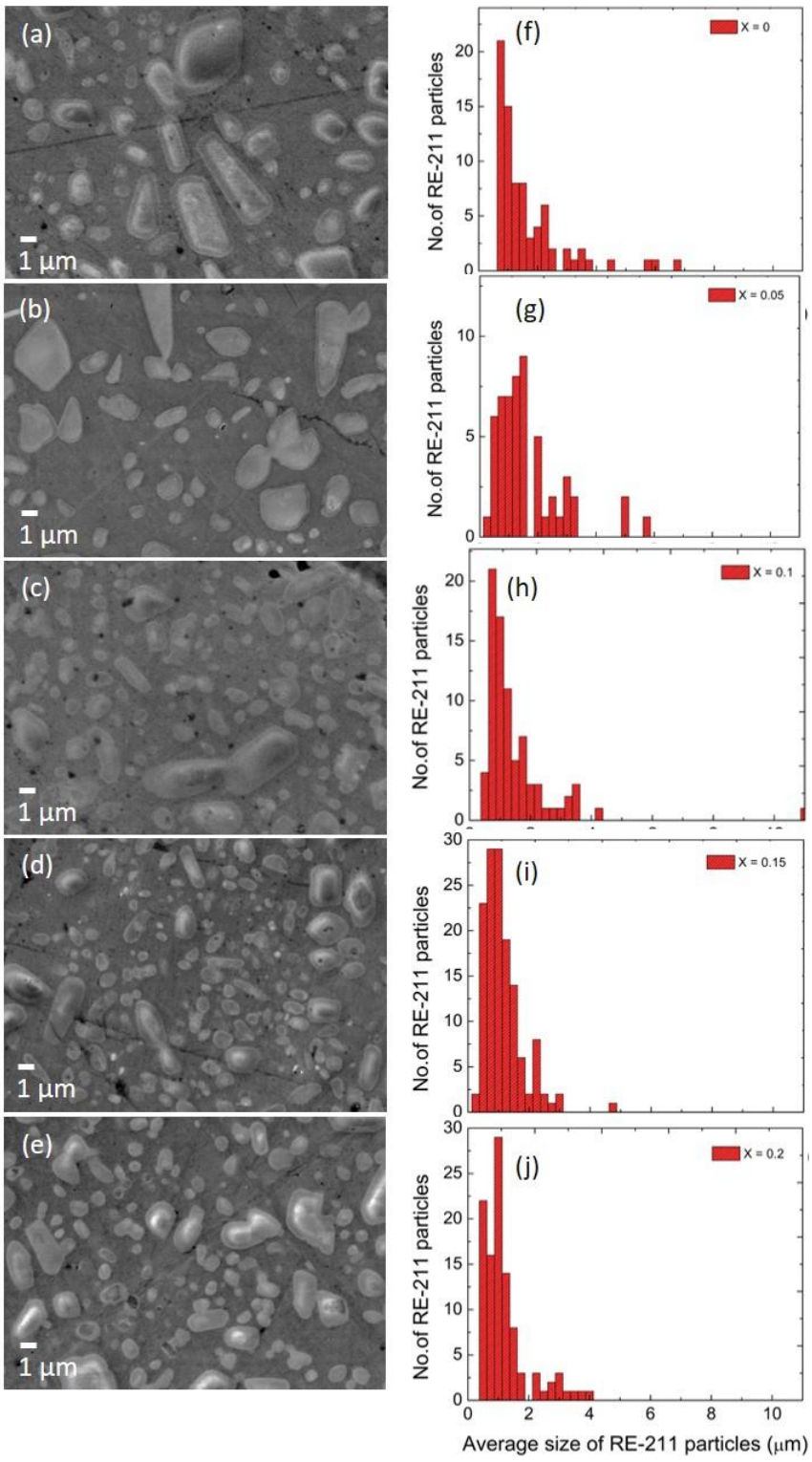

Figure 4.11 FESEM images of (a) X0, (b) X0.05, (c) X0.1, (d) X0.15, and (e) X0.2 samples

Gd, Y, and Er is shown in Table 4.1. In case of large particles such as 1, 2, 3 and 4, the composition tends to be rich in Y concentration. However, in small particles such as spot 5, the composition was rich in Er concentration. Spots 6, 7, and 8 correspond to the matrix at different positions exhibiting element ratio of 1:2:3 of RE:Ba:Cu, which is the RE-123 superconducting phase. Similarly, in X0.2 sample EDX analysis revealed that smaller particles were Er-rich, while the larger ones were Y-rich. Detailed compositions can be found in Table 4.2. We can conclude from the current analysis that small particles on X0 and X0.2 samples have a high Er content, which enhances the superconducting properties. Er-123 melts at a lower temperature compared to Gd-123 and Y-123, due to which it leaves residual RE-211 trapped in the matrix. The chemical fluctuation of secondary phase particles were observed in mixed systems such as (Y,Gd)-123, (Dy,Y)-123 etc. The elemental fluctuation in the ternary secondary phase was examined in terms of particles size and chemical analysis via EDX [26, 42, 50]. From the current work, it is clear that using high Er concentration leads to better superconducting properties in bulk (Gd,Y,Er)-123 superconductor fabricated via IG process [43]. Formation of complex secondary phases in mixed system tends to enhance superconducting performance in this high temperature superconductor.

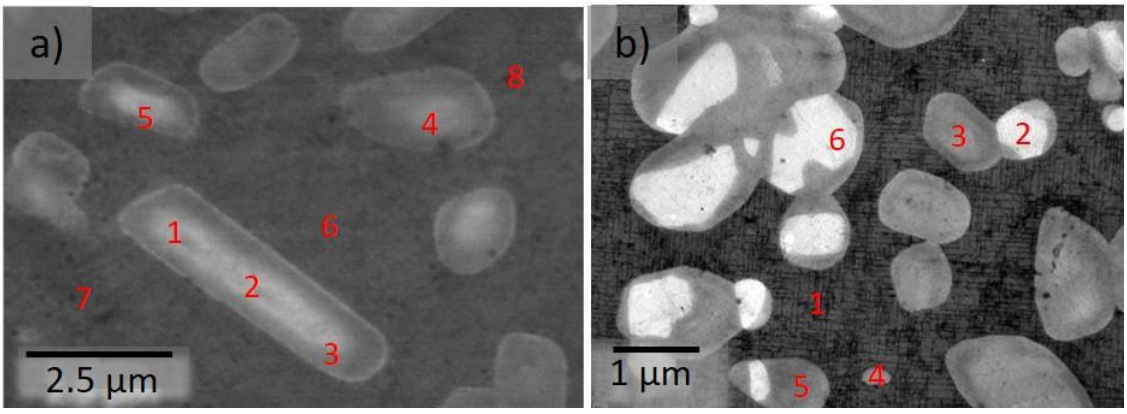

Figure 4.12 EDX area element analysis data for the bulk (a) X0, and (b) X0.2 samples

Table 4.1 EDX spectra of the X0 sample in Fig. 12(a)

Area	Gd (at%)	Y (at%)	Er (at%)	Ba (at%)	Cu (at%)	O (at%)
1	7.75	13.82	7.84	18.62	13.50	38.47
2	11.0	13.34	6.22	18.62	13.59	37.23
3	8.70	14.96	6.83	18.24	13.91	37.36
4	8.59	14.78	6.00	18.75	13.10	38.79
5	2.67	5.65	17.41	18.76	15.15	40.37
6	2.98	5.40	2.12	24.72	24.96	39.82
7	3.20	5.62	2.32	24.03	25.61	39.23
8	3.02	6.69	2.04	24.28	24.86	39.11

Table 4.2 EDX spectra of the X0.2 sample in Fig. 12(b)

Area	Gd (at%)	Y (at%)	Er (at%)	Ba (at%)	Cu (at%)	O (at%)
1	4.10	1.61	6.46	16.50	25.95	45.37
2	3.93	10.26	8.23	14.47	18.30	44.81
3	6.01	2.23	14.97	13.75	16.38	46.65
4	4.45	1.41	7.06	16.08	24.60	46.40
5	3.53	1.79	7.09	16.96	27.12	43.50
6	4.48	11.89	11.89	12.45	13.57	47.66

To understand the complex microstructure of ternary RE-123 bulk superconductors, the elemental mapping was carried out at different points of RE-211 secondary phase particles and RE-123 matrix. The energy dispersion spectroscopy (EDS) elemental analysis of (Gd,Y,Er)-123 samples is shown in Figs. 4.13 – 4.17. Gd, Y, and Er elements were distributed homogeneously in both RE-211 and RE-123 regions. However, different regions contained different types of RE-211 phases. Atomic percentage of each element is shown in Tables 4.3-4.7. Results are similar to those reported by Setoyama, et al and Das, et al [42, 50]. The reaction of RE ions entering RE-211 phase depended on the temperature during IG process and peritectic temperature, T_p, of each compound. First, RE-123 matrix started to form at the highest T_p, and then RE-211 boundaries were consumed. A chemical fluctuation of secondary phase and matrix occurred.

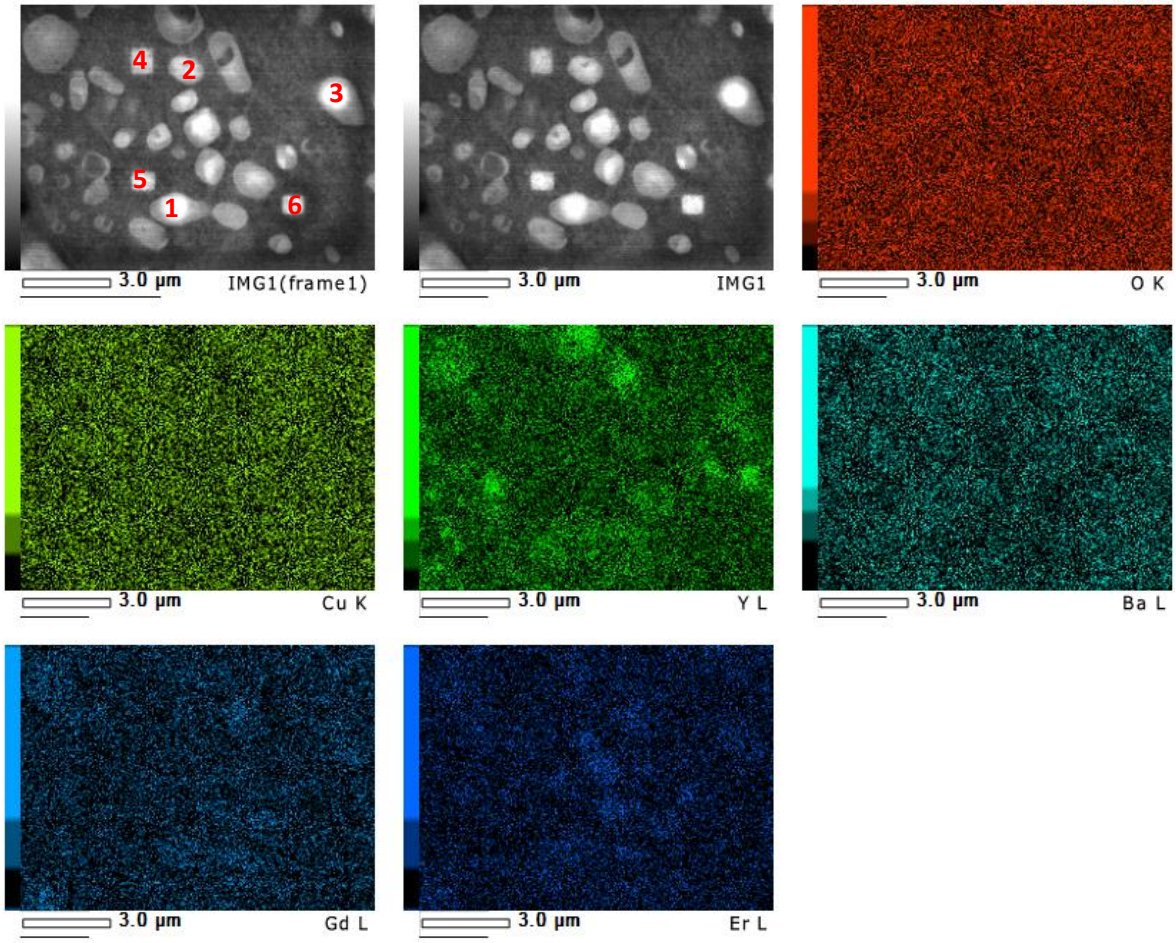

Figure 4.13 EDX mapping of X0 sample

Table 4.3 EDX mapping element analysis of the X0 sample in Fig 4.13

Area	Gd (at%)	Y (at%)	Er (at%)	Ba (at%)	Cu (at%)	O (at%)
1	10.65	13.01	6.20	20.14	14.65	35.35
2	5.14	12.59	4.16	23.65	20.82	33.63
3	9.47	14.56	7.25	19.89	14.52	34.32
4	3.04	5.81	2.36	26.33	26.60	35.95
5	3.05	5.61	2.45	26.09	26.84	35.97
6	3.22	5.84	2.57	26.03	26.28	36.07

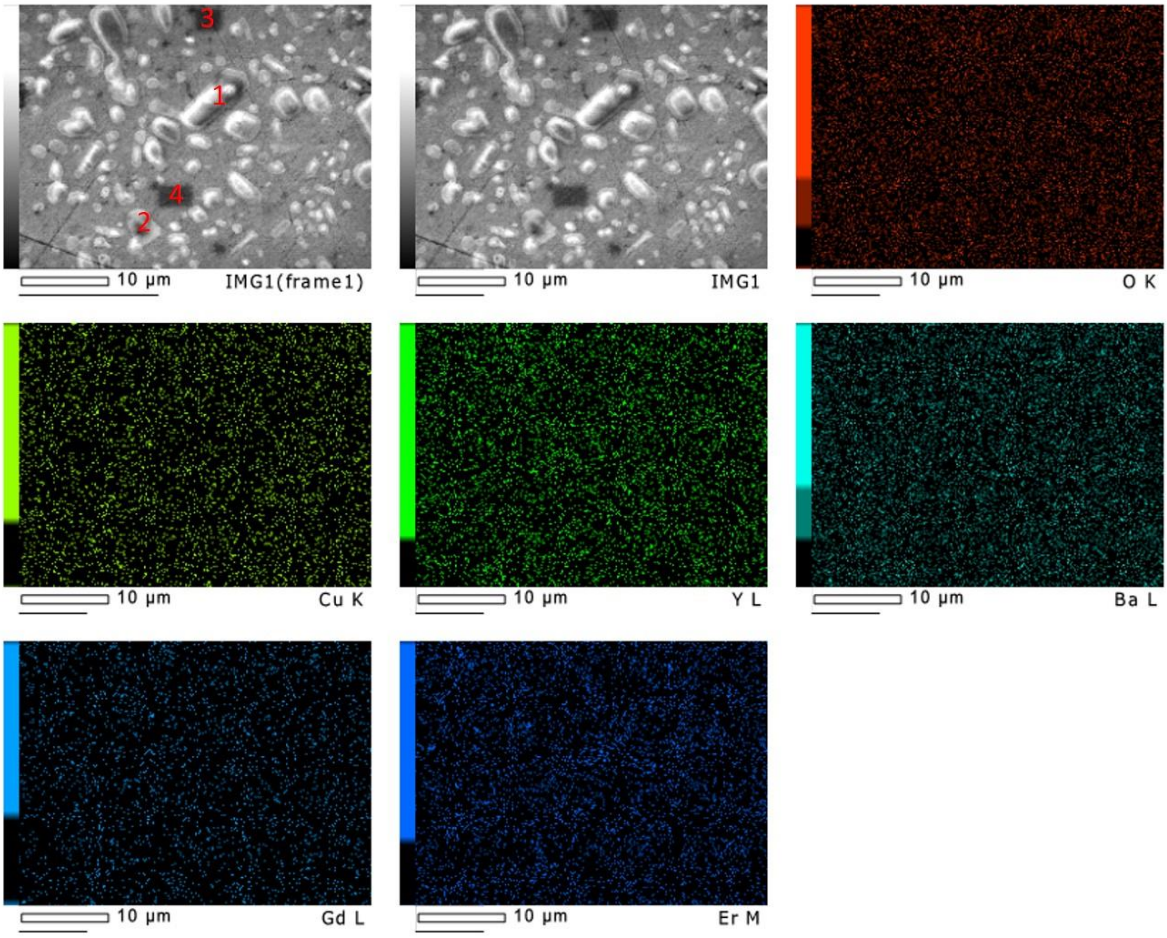

Figure 4.14 EDX mapping of X0.05 sample

Table 4.14 EDX mapping element analysis of the X0.05 sample in Fig 4.14

Area	Gd (at%)	Y (at%)	Er (at%)	Ba (at%)	Cu (at%)	O (at%)
1	8.25	16.50	5.32	18.78	13.67	37.49
2	7.37	15.23	5.78	18.70	14.28	38.64
3	2.99	5.40	1.76	24.30	25.63	39.92
4	3.07	5.18	1.62	24.45	25.25	40.43

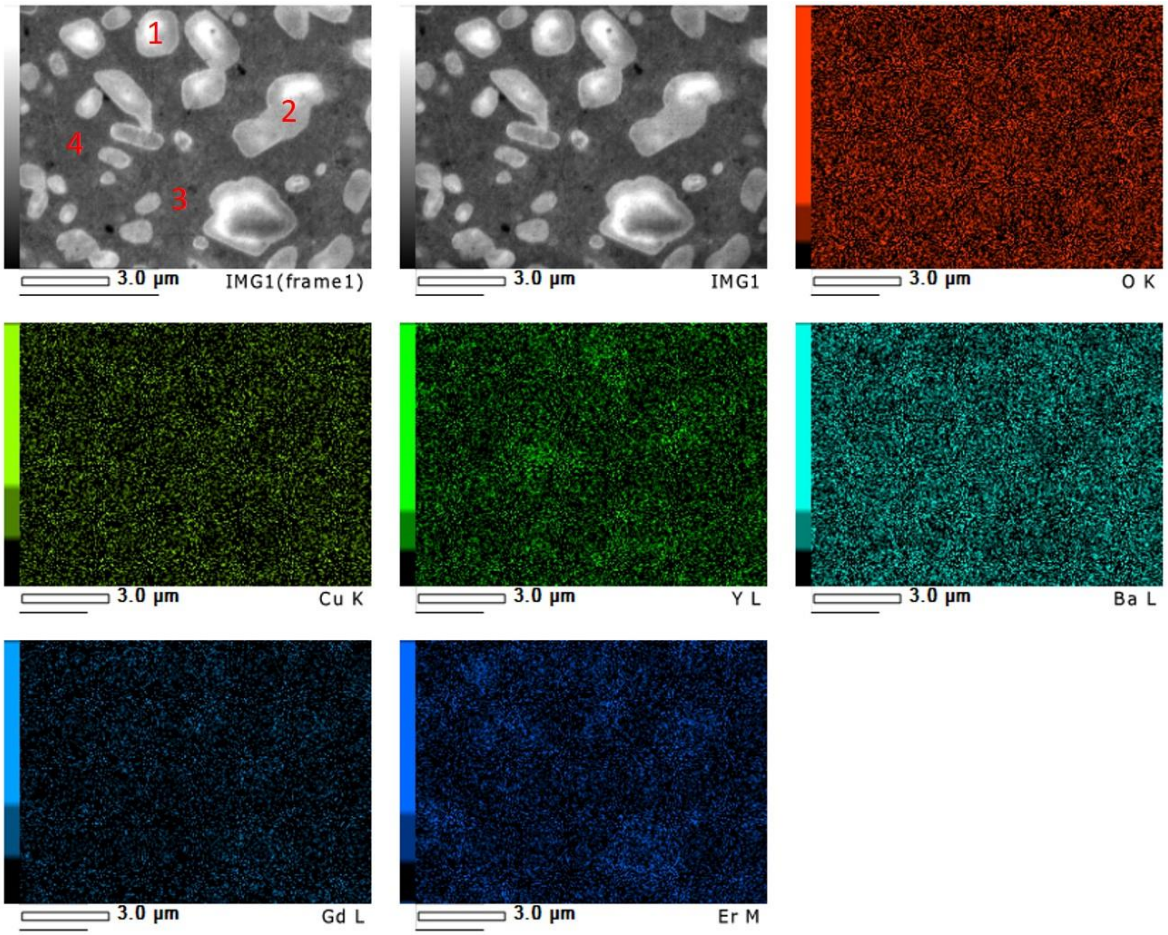

Figure 4.15 EDX mapping of X0.1 sample

Table 4.5 EDX mapping element analysis of the X0.1 sample in Fig 4.15

Area	Gd (at%)	Y (at%)	Er (at%)	Ba (at%)	Cu (at%)	O (at%)
1	12.85	8.76	4.63	18.93	13.73	41.11
2	7.30	11.71	6.40	20.72	15.46	38.42
3	3.47	4.49	2.02	24.40	25.44	40.18
4	3.34	5.26	1.91	24.32	25.54	39.63

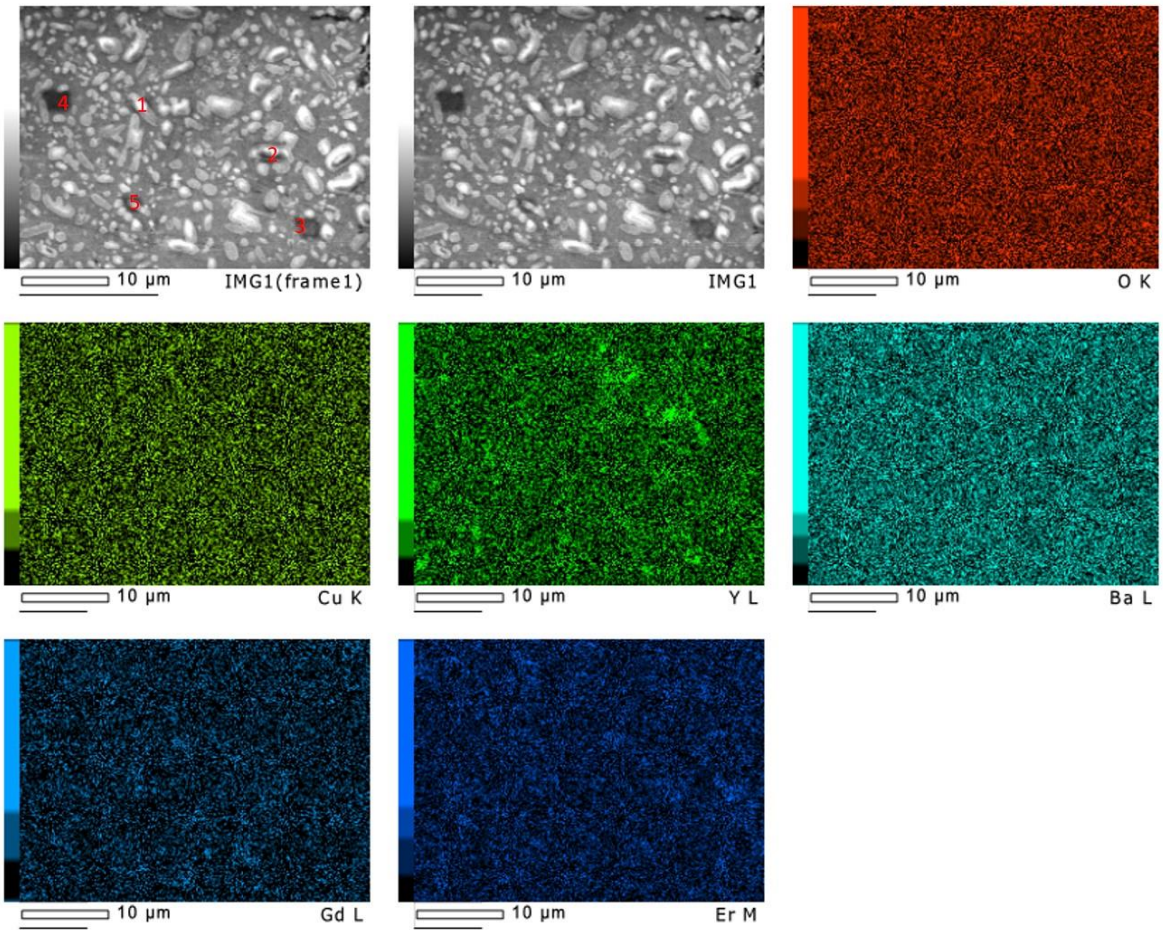

Figure 4.16 EDX mapping of X0.15 sample

Table 4.6 EDX mapping element analysis of the X0.15 sample in Fig 4.16

Area	Gd (at%)	Y (at%)	Er (at%)	Ba (at%)	Cu (at%)	O (at%)
1	9.50	8.60	6.31	20.08	15.96	39.56
2	9.58	10.80	6.45	20.01	14.49	38.68
3	2.98	3.41	2.32	26.05	25.97	39.27
4	3.07	3.56	2.38	25.67	25.86	39.46
5	8.41	5.73	6.2	21.54	17.81	40.31

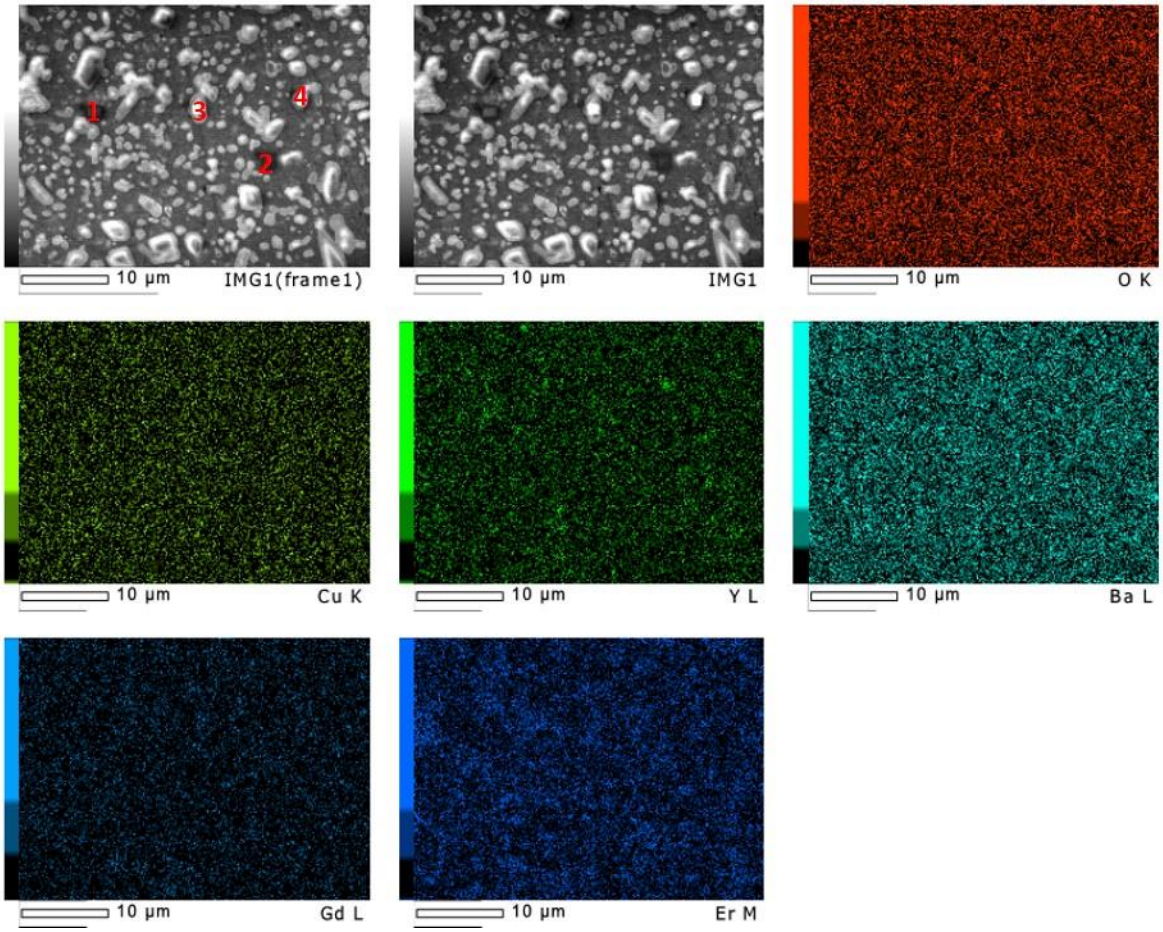

Figure 4.17 EDX mapping of X0.2 sample

Table 4.7 EDX mapping element analysis of the X0.2 sample in Fig 4.17

Area	Gd (at%)	Y (at%)	Er (at%)	Ba (at%)	Cu (at%)	O (at%)
1	3.31	3.40	2.67	24.31	24.87	41.43
2	3.41	2.63	2.93	24.03	24.93	42.07
3	8.17	7.38	8.75	18.82	14.17	42.72
4	6.34	2.64	12.46	19.43	14.69	44.45

4.4 Conclusions

We successfully fabricated bulk (Gd,Y,Er)-123 superconductors by the infiltration growth process. Using preform with Er-rich composition resulted in an improved performance of the bulk. In all samples, XRD results and trapped field distribution profiles clearly showed the single-grain nature of the bulks. $T_{c,onset}$ values of all samples were around 91.5 K - 92 K and ΔT_c was less than 1 K. The highest trapped field and J_c were achieved in X0.2 ($(Gd_{0.33}Y_{0.13}Er_{0.53})$-123) bulk. The highest TF value at 77 K was 0.53 T, while the self-field J_c was 63.05 kA/cm^2 at 77 K and 238.86 kA/cm^2 at 50 K. Microstructure of (Gd,Y,Er)-123 observed by FESEM clearly indicated fine (Gd,Y,Er)-211 particles dispersed in the matrix. (Gd,Y,Er)-211 particles size decreased with increasing Er concentration. EDX analysis revealed that the ratio of atom percentage in (Gd,Y,Er)-123 phase was stoichiometric. The fine RE-211 particles in X0.2 sample contained more Er than large particles. Bulks with large number of Er-rich (RE)-211 secondary phases showed significant improvement in the superconducting performance. This study shows an improved superconducting performance of the Er-rich (Gd,Y,Er)-123 system synthesized in air by IG process. We can further optimize this process by controlling particle size of (Gd,Y,Er)-211 via mechanical refinement technique such as ball milling or ultra-sonication to enhance the superconducting properties. Aside the improvement of superconducting properties, a very important gain of this study is the possibility to prepare these superconductors in air, which significantly simplifies the scale-up of the technology to industrial production.

References

1. Nakamura, T., et al., *Development of a superconducting bulk magnet for NMR and MRI.* Journal of Magnetic Resonance, 2015. **259**: p. 68-75.
2. Durrell, J.H., et al., *Bulk superconductors: a roadmap to applications.* Superconductor Science and Technology, 2018. **31**(10): p. 103501.
3. Miki, M., et al., *Development of a synchronous motor with Gd–Ba–Cu–O bulk superconductors as pole-field magnets for propulsion system.* Superconductor Science and Technology, 2006. **19**(7): p. S494-S499.
4. Murakami, M., *Processing and Applications of Bulk RE–Ba–Cu–O Superconductors.* International Journal of Applied Ceramic Technology, 2007. **4**(3): p. 225-241.
5. Werfel, F.N., et al., *Superconductor bearings, flywheels and transportation.* Superconductor Science and Technology, 2011. **25**(1): p. 014007.
6. Tomita, M. and M. Murakami, *High-temperature superconductor bulk magnets that can trap magnetic fields of over 17 tesla at 29 K.* Nature, 2003. **421**(6922): p. 517-520.
7. Cardwell, D.A., *Processing and properties of large grain (RE)BCO.* Materials Science and Engineering: B, 1998. **53**(1-2): p. 1-10.
8. Murakami, M., *Melt Processed High-Temperature Superconductors*. Melt Processed High-Temperature Superconductors. 1992.
9. Schmitz, G.J. and B. Nestler, *Simulation of phase transitions in multiphase systems: peritectic solidification of (RE)$Ba_2Cu_3O_{7-x}$ superconductors.* Materials Science and Engineering: B, 1998. **53**(1): p. 23-27.
10. Murakami, M., *Melt-processing of high temperature superconductors.* Progress in Materials Science, 1994. **38**: p. 311-357.

11. Chow, J.C.L., et al., *Processing, Y_2BaCuO_5 distribution and critical current density in large grain Pt-doped YBCO.* Materials Science and Engineering: B, 1998. **53**(1): p. 79-85.

12. Kim, C.-J. and G.-W. Hong, *Defect formation, distribution and size reduction of in melt-processed YBCO superconductors.* Superconductor Science and Technology, 1999. **12**(3): p. R27-R42.

13. Diko, P. and G. Krabbes, *Macro-cracking in melt-grown YBaCuO superconductor induced by surface oxygenation.* Superconductor Science and Technology, 2002. **16**(1): p. 90-93.

14. Murakami, M., et al., *Melt-processed light rare earth element-Ba-Cu-O.* Superconductor Science and Technology, 1996. **9**(12): p. 1015-1032.

15. Yoo, S.I., et al., *Melt processing for obtaining $NdBa_2Cu_3O_y$ superconductors with high T_c and large J_c.* Applied Physics Letters, 1994. **65**(5): p. 633-635.

16. Sudhakar Reddy, E. and T. Rajasekharan, *Microstructural and magnetic properties of textured $GdBa_2Cu_3O_y/Gd_2BaCuO_5$ composites fabricated from Gd_2BaCuO_5 preforms.* Physica C Superconductivity, 1999. **316**: p. 279.

17. Cloots, R., et al., *From RE-211 to RE-123. How to control the final microstructure of superconducting single-domains.* Superconductor Science and Technology, 2004. **18**(3): p. R9-R23.

18. Reddy, E.S. and T. Rajasekharan, *Shape Forming Simultaneous with J_c Enhancement in $REBa_2Cu_3O_7$ Superconductors.* Journal of Materials Research, 1998. **13**(9): p. 2472-2475.

19. Iida, K., et al., *Seeded infiltration and growth of large, single domain Y–Ba–Cu–O bulk superconductors with very high critical current densities.* Superconductor Science and Technology, 2005. **18**(11): p. 1421.

20. Babu, N.H., et al., *Improved magnetic flux pinning in melt processed (Y,Nd)$Ba_2Cu_3O_{7-\delta}$ superconductor.* Superconductor Science and Technology, 2004. **18**(2): p. S38-S42.

21. Kim, M., et al., *$YSmBaCuO_5$ distribution within $Y_{0.5}Sm_{0.5}Ba_2Cu_3O_{7-x}$ superconductors fabricated by infiltration and side-seeded melt-growth process.* Physica C: Superconductivity, 2008. **468**(15-20): p. 1399-1403.

22. Muralidhar, M., et al., *Irreversibility field above 14 T at 77 K in (Nd,Eu,Gd)$Ba_2Cu_3O_y$.* IEEE Transactions on Applied Superconductivity, 2003. **13**(2): p. 3091-3094.

23. Muralidhar, M., et al., *Pinning characteristics in chemically modified (Nd,Eu,Gd)–Ba–Cu–O superconductors.* Applied Physics Letters, 2003. **82**(6): p. 943-945.

24. Muralidhar, M., et al., *Effect of nanoscopic ZrO_2 particles on flux pinning in (Nd,Eu,Gd)-123/Gd-211 composites.* Superconductor Science and Technology, 2004. **17**: p. 1129.

25. Muralidhar, M., et al., *New Type of Vortex Pinning Structure Effective at Very High Magnetic Fields.* Physical Review Letters, 2002. **89**(23): p. 237001.

26. Shi, Y., et al., *The growth and superconducting properties of RE–Ba–Cu–O single grains with combined RE elements (RE = Gd and Y).* Superconductor Science and Technology, 2020. **33**(3): p. 035003.

27. Volochová, D., et al., *Influence of Gd Addition on the Microstructure and Superconducting Properties of YBCO Bulk Superconductors.* IEEE Transactions on Applied Superconductivity, 2018. **28**(4): p. 1-5.

28. Jirsa, M., et al., *Engineering of Jc–B characteristics of RE–Ba–Cu–O melt-textured superconductors.* Physica C: Superconductivity, 2002. **378-381**: p. 707-712.

29. Muralidhar, M., et al., *Nanoscale Gd_2BaCuO_5 particles in $(Sm_{0.33}Eu_{0.33}Gd_{0.33})Ba_2Cu_3O_y$ and magnetic levitation at 90.2 K.* Superconductor Science and Technology, 2005. **18**(3): p. L9.

30. Pavan Kumar Naik, S., et al., *Growth and physical properties of top-seeded infiltration growth processed large grain (Gd, Dy) BCO bulk superconductors.* Journal of Applied Physics, 2017. **122**(19): p. 193902.

31. Cardwell, D.A. and N. Hari Babu, *Processing and properties of single grain (RE)–Ba–Cu–O bulk superconductors.* Physica C: Superconductivity and its Applications, 2006. **445-448**: p. 1-7.

32. Pinmangkorn, S., et al., *Enhancing the superconducting performance of melt grown bulk $YBa_2Cu_3O_y$ via ultrasonically refined Y_2BaCuO_5 without PtO_2 and CeO_2.* Materials Chemistry and Physics, 2020. **244**: p. 122721.

33. Pinmangkorn, S., et al., *Effect of Ultra-sonicated Y_2BaCuO_5 on Top-Seeded Melt Growth $YBa_2Cu_3O_y$ Bulk Superconductor.* Journal of Superconductivity and Novel Magnetism, 2020.

34. Bean, C.P., *Magnetization of High-Field Superconductors.* Reviews of Modern Physics, 1964. **36**(1): p. 31-39.

35. Chen, D.X. and R.B. Goldfarb, *Kim model for magnetization of type-II superconductors.* Journal of Applied Physics, 1989. **66**(6): p. 2489-2500.

36. Reddy, E.S. and T. Rajasekharan, *Fabrication of textured (RE = Y, Gd) composites by infiltration and growth of preforms by liquid phases.* Superconductor Science and Technology, 1998. **11**(5): p. 523-534.

37. Foerster, C.E., et al., *Mechanical Properties of $(RE)Ba_2Cu_3O_{7-\delta}$ Superconductor With RE Obtained From Xenotime Mineral.* IEEE Transactions on Applied Superconductivity, 2011. **21**(2): p. 52-59.

38. Muralidhar, M., et al., *Improvement in Field Trapping Capability of (Nd,Eu,Gd)$Ba_2Cu_3O_y$ with Ag_2O Addition.* Japanese Journal of Applied Physics, 2001. **40**(11R): p. 6329.

39. Nakazato, K., et al., *Fabrication of bulk Y–Ba–Cu–O superconductors with high critical current densities through the infiltration-growth process.* Cryogenics, 2014. **63**: p. 129-132.

40. Iida, K., et al., *Superconducting properties and microstructures of Er–Ba–Cu–O superconductor.* Superconductor Science and Technology, 2003. **16**(6): p. 699.

41. Iida, K., et al., *Seeded infiltration and growth of single-domain Gd–Ba–Cu–O bulk superconductors using a generic seed crystal.* Superconductor Science and Technology, 2006. **19**(7): p. S478.

42. Das, D., et al., *Top-seeded infiltration growth of (Y,Gd)$Ba_2Cu_3O_y$ bulk superconductors with high critical current densities.* Superconductor Science and Technology, 2017. **30**(10): p. 105015.

43. Saitoh, T., et al., *Microstructures and superconducting properties of melt-processed (RE,RE')-Ba-Cu-O.* Physica C: Superconductivity, 1997. **288**(1): p. 141-147.

44. Muralidhar, M., et al., *Levitation of NEG-123 at the temperature of liquid oxygen (90.2 K).* Superconductor Science and Technology, 2003. **16**(11): p. L46-L48.

45. Dew-Hughes, D., *Flux pinning mechanisms in type II superconductors.* The Philosophical Magazine: A Journal of Theoretical Experimental and Applied Physics, 1974. **30**(2): p. 293-305.

46. Sai Srikanth, A., et al., *Optimization of Carbon Encapsulated Boron Doping for High-Performance Bulk Sintered MgB_2.* Advanced Engineering Materials, 2020. **22**(11): p. 2000478.

47. Koblischka, M.R., et al., *Analysis of pinning in $NdBa_2Cu_3O_{7-\delta}$ superconductors.* Physical Review B, 1998. **58**(5): p. 2863-2867.

48. Muralidhar, M., et al., *Progress in melt-processed (Nd–Sm–Gd)$Ba_2Cu_3O_y$ superconductors.* Superconductor Science and Technology, 2002. **16**(1): p. R1.

49. Koblischka-Veneva, A., et al., *Comparison of Temperature and Field Dependencies of the Critical Current Densities of Bulk YBCO, MgB_2, and Iron-Based Superconductors.* IEEE Transactions on Applied Superconductivity, 2019. **29**(5): p. 1-5.

50. Setoyama, Y., et al., *Systematic change of flux pinning in (Dy,RE)123 and (Y,RE)123 melt-solidified bulks with unit cell orthorhombicity.* Superconductor Science and Technology, 2014. **28**(1): p. 015014.

51. Kumar, N.D., et al., *Unprecedented current density to high fields in $YBa_2Cu_3O_{7-\delta}$ superconductor through nano-defects generated by preform optimization in infiltration growth process.* Superconductor Science and Technology, 2010. **23**(10): p. 105020.

52. Mahmood, A., et al., *Pre-sintering effects on the critical current density of YBCO bulk prepared by infiltration method.* Physica C: Superconductivity, 2008. **468**(15-20): p. 1350-1354.

Chapter 5

Spatial Variation of $(Gd_{0.33},Y_{0.13},Er_{0.53})Ba_2Cu_3O_y$ Bulk Superconductors

5.1 Introduction

Uniformity of microstructure and superconducting properties of bulk $REBa_2Cu_3O_y$ (RE-123, RE = rare earth) superconductors is essential for practical applications such as medical and transportation devices [1]. One of the most attractive applications of bulk superconductors is trapped-field magnet. Bulk RE-123 samples can trap magnetic field much higher than a conventional permanent magnet [2]. A good quality single-grain RE-123 bulk can be fabricated by both top seeded melt texture growth, TSMG, and infiltration growth, IG, processes. Using the TSMG process, several problems have been observed such as shrinkage, generation of large pores, large cracks, large-size secondary phase particles,

inhomogeneously distributed, and an undesirable multiple matrix growth nucleation [3-6]. The IG process seems to solve majority of these problems and enables to control microstructure quality (especially size and distribution of RE-211) [7]. Some recent studies have shown that IG is not still perfect and an inhomogeneous RE-211 distribution in the final bulk sometimes appears [8-10]. Hence, we tried to check the structural homogeneity in the ternary REBCO bulk that we optimized previously. The results shown in chapter 4 indicate that ($Gd_{0.33}Y_{0.13}Er_{0.53}$)$Ba_2Cu_3O_y$ exhibits the best performance in Gd, Y, and Er ternary REBCO system [11]. In this chapter, the bulk ($Gd_{0.33}Y_{0.13}Er_{0.53}$)$Ba_2Cu_3O_y$ sample is spatially analyzed in terms of the microstructural and superconducting properties.

5.2 Experimental details

In this experiment, the fully grown ($Gd_{0.33}Y_{0.13}Er_{0.53}$)$Ba_2Cu_3O_y$ bulk (Fig. 5.1(a)) was cut into small pieces to studied and verify the uniformity of superconducting properties and microstructure. The small specimens (dimensions approximately 1.5x1.5x0.5 mm^3) were cut along *c*-axis into small specimen shown in Fig. 5.1(b). The critical current density (J_c) (estimated from *M-H* loops by the extended Bean critical state model) and critical temperature (T_c) were examined in all specimens by SQUID magnetometer (MPMS5 model) [12, 13]. The microstructure was observed using the field-emission scanning electron microscope (FESEM).

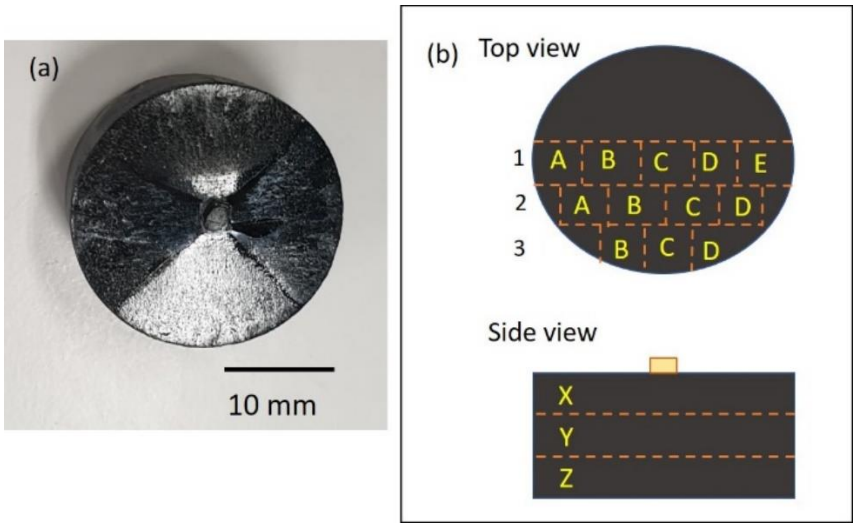

Figure 5.1 (a) Bulk ($Gd_{0.33}Y_{0.13}Er_{0.53}$)-123 sample, and (b) Cutting method, and the label position indicating each specimen of the bulk sample

To support the variation of RE-211 secondary phase in the matrix, we studied the microstructure at various stages of RE-211 preform during the conventional thermal profile. We attempted to view the evolution of the reaction as well as LP infiltration as a function of time. As shown in Fig. 5.2(a), same set up of the (Gd,Y,Er)-123 sample fabrication as used in chapter 4 was employed in this study. The sample is quenched (room temperature, air) at two stages of the thermal cycle, at 880 and 1050ºC as shown in Figs. 5.2 (b)-(c) and microstructure of the samples was characterized.

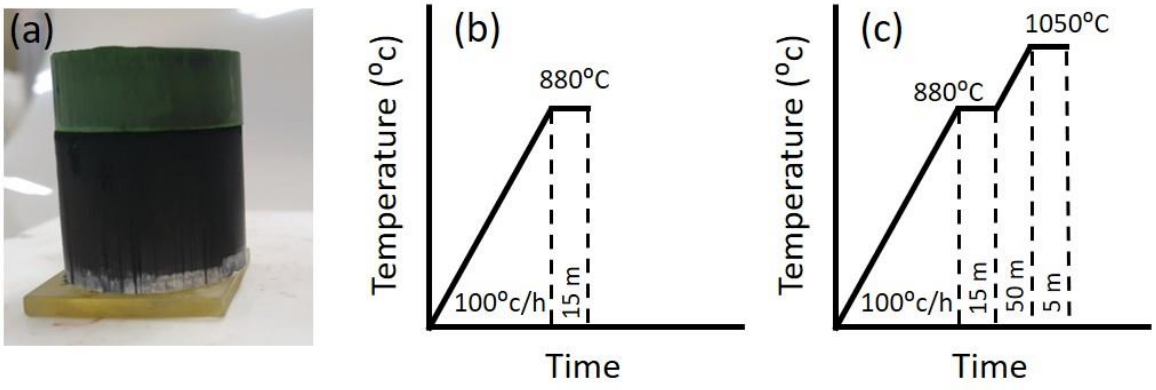

Figure 5.2 (a) The preparation of the samples for IG process and temperature profile of RE-211 preforms at (b) 880ºC, and (c) 1050ºC

5.3 Results and discussion

5.3.1 Variation of superconducting properties

5.3.1 (a) Critical temperature (T_c)

T_c is considered as the main intrinsic property characterizing each superconductor. For example, T_c of MgB_2 is ~39 K, T_c of RE-123 (Y-123, (Gd,Y)-123 and (Nd,Eu,Gd)-123) is ~91-93 K [14-17]. The magnetization was measured after zero-field cooling, upon applying field of 1 mT parallel to the *c*-axis of the samples.

Temperature dependence of the normalized DC susceptibility (χ) is shown in Fig. 5.3. Table 5.1 shows the values of $T_{c,onset}$, $T_{c,offset}$, and ΔT_c estimated from Fig. 5.3. T_c at various positions is nearly constant. The average values of $T_{c,onset}$, $T_{c,offset}$, and ΔT_c were 92.15, 91.35, and 0.8 K, respectively. The value of ΔT_c below 1 K indicates (1) good quality and (2) sufficient amount of oxygen content in the samples [18].

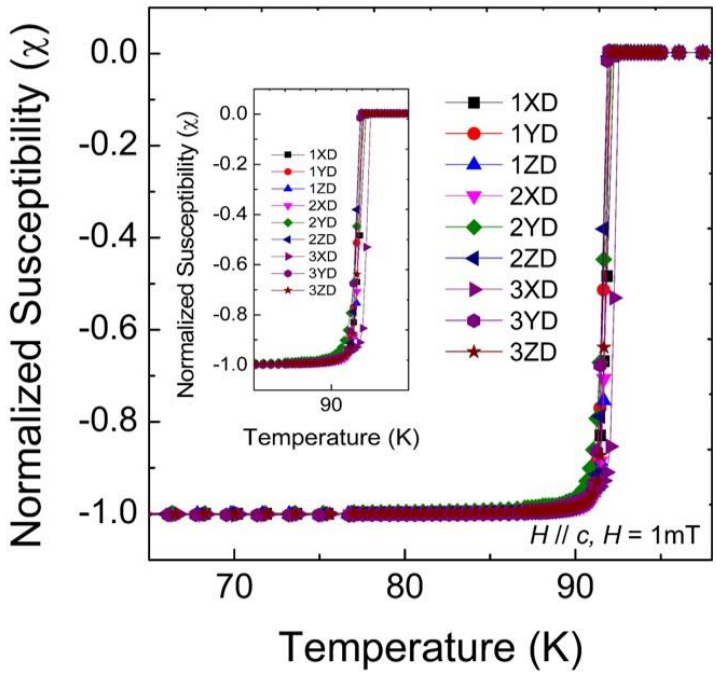

Figure 5.3 Temperature dependence of normalized dc magnetization for specimens cut from various positions

Table 5.1 T_c values at various positions of ($Gd_{0.33}$,$Y_{0.13}$,$Er_{0.53}$)-123 bulk sample

Positions	$T_{c,onset}$ (K)	$T_{c,offset}$ (K)	ΔT_c (K)
1XD	92.36	91.40	0.96
1YD	92.14	91.30	0.84
1ZD	92.05	91.36	0.69
2XD	92.06	91.18	0.88
2YD	92.15	91.15	1.00
2ZD	92.05	91.30	0.75
3XD	92.55	91.90	0.65
3YD	91.97	91.18	0.79
3ZD	92.06	91.42	0.64

5.3.1 (b) Critical current density (J_c)

Figs. 5.4 (a)-(i) show the J_c-B curves at 77 K, H//c-axis at different positions. The sample nomenclature follows the one previously shown in Fig. 5.1 (b). The self-field J_c plotted as a function of the sample position is shown in Fig. 5.5 and J_c values at various applied magnetic fields are summarized in Table 5.2.

For layer 1, J_c at the bulk periphery (positions A and E) is larger than that at the center (position C, under the seed). 1XA exhibits the highest J_c value of 81.13 kA/cm^2 at self-field and 20 kA/cm^2 at 1 T. This value is considerably large comparing to other superconductors. The self-field J_c of 1XC located at the center below the seed was 66.43 kA/cm^2, the value slightly lower than that at periphery of the pellet. For comparison, the previous publication on Y-123 reported $J_c \sim 40$ kA/cm^2 at self-field and < 10 kA/cm^2 at 1T [15, 19]. According to the results of J_c shown in Table 5.2, we conclude that J_c increases as we go away from the position under the seed (1XC) towards pellet periphery. An opposite trend was observed along the direction of c-axis, i.e. J_c decreased with increasing distance from the seed. This trend of J_c drop along c-axis is consistent with previous results [10], whereas the J_c increase along a/b-axis seems to be inconsistent with few prior reports [9]. The layers 2 and 3 showed a similar behavior, i.e. J_c decrease along c-axis direction away from the seed.

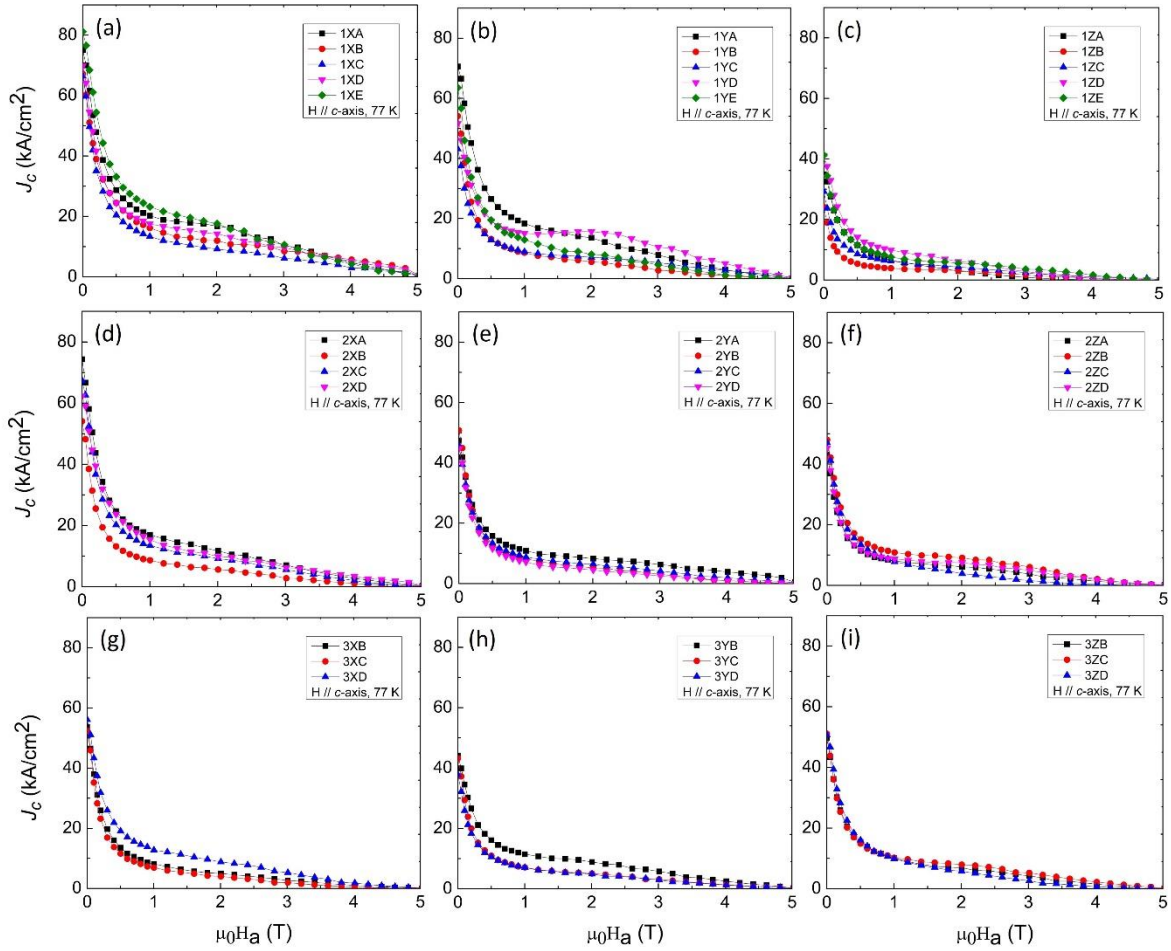

Figure 5.4 J_c-B curves of $(Gd_{0.33},Y_{0.13},Er_{0.53})$-123 bulk sample at various positions

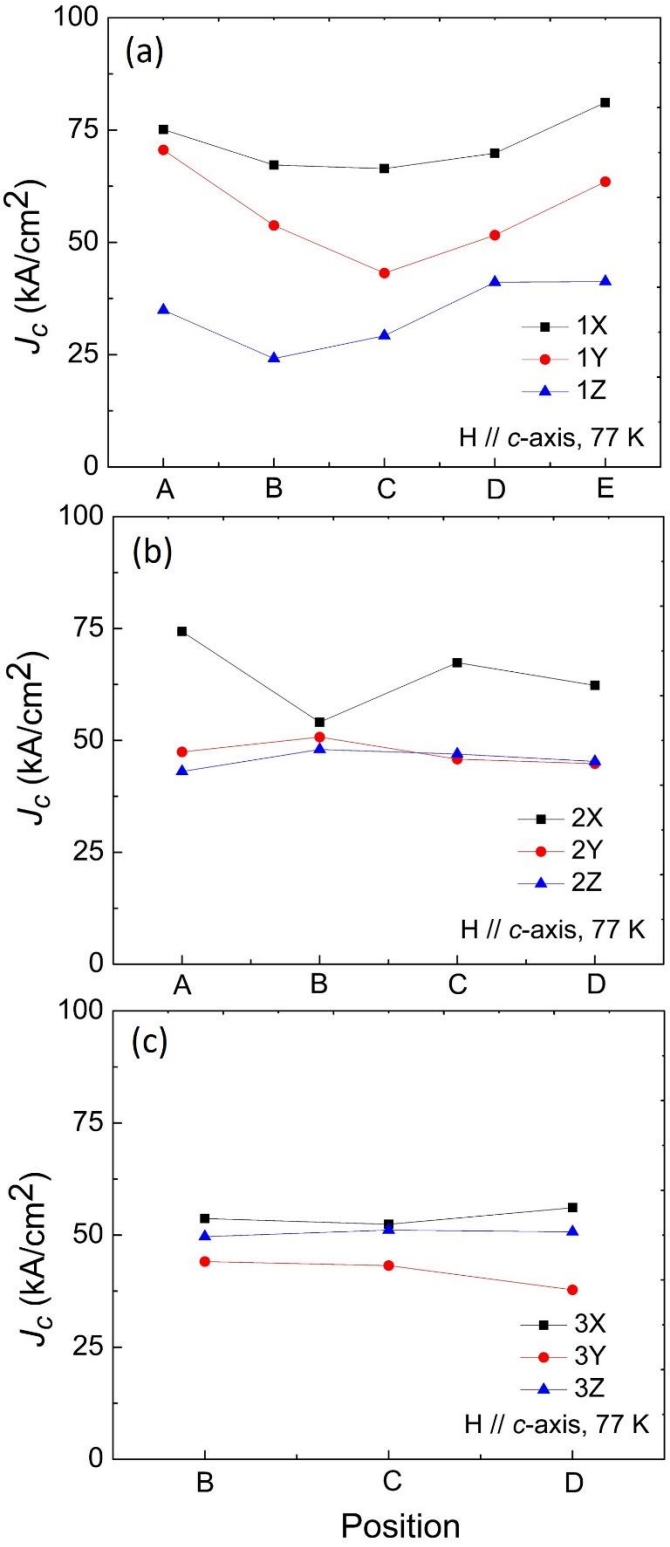

Figure 5.5 J_c values at self-field, 77 K versus the position in the bulk sample (a) layer 1, (b) layer 2, and (c) layer 3

Table 5.2 J_c values at various positions and fields of $(Gd_{0.33},Y_{0.13},Er_{0.53})$-123 bulk sample

Positions	J_c (kA/cm^2) at 77 K, H // c-axis						
	0 T	0.5 T	1 T	1.5 T	2 T	2.5 T	3 T
1XA	75.13	28.71	20.23	18.31	16.77	14.26	10.28
1XB	67.22	24.47	16.14	13.27	11.98	10.68	8.47
1XC	66.43	20.43	13.34	11.26	9.20	8.43	6.09
1XD	69.85	27.76	17.53	15.91	14.23	11.82	9.65
1XE	81.13	33.11	23.19	20.47	17.61	15.11	10.63
1YA	70.58	26.51	18.35	15.99	13.58	10.70	7.83
1YB	53.78	16.86	13.56	13.11	12.92	12.33	9.77
1YC	43.15	12.86	8.92	7.82	7.09	6.51	5.31
1YD	51.60	19.22	15.06	15.00	15.67	14.77	10.46
1YE	63.51	19.50	12.92	10.33	8.05	6.97	4.54
1ZA	34.91	11.48	6.48	5.02	2.91	2.02	0.86
1ZB	24.13	5.36	3.88	3.46	3.11	2.60	1.70
1ZC	29.21	8.59	6.24	5.11	4.31	3.57	2.45
1ZD	41.12	14.16	9.87	8.27	6.10	4.97	2.82
1ZE	41.27	11.62	7.57	6.43	5.52	5.06	3.54
2XA	74.34	24.69	16.92	14.47	11.70	10.16	7.01
2XB	54.07	13.18	8.62	7.21	5.59	4.61	2.75
2XC	67.38	20.19	13.45	11.16	9.16	8.19	5.55
2XD	62.29	23.69	15.33	12.55	9.84	8.47	6.20
2YA	47.43	15.79	10.83	9.44	8.27	7.57	6.30
2YB	50.75	12.86	8.24	6.68	5.20	4.22	3.06
2YC	45.80	13.38	8.75	7.46	6.48	5.65	4.13
2YD	44.79	11.59	7.16	5.50	4.51	3.76	2.53
2ZA	43.07	11.41	8.09	7.24	6.09	5.42	3.75
2ZB	47.97	15.17	10.85	9.86	9.08	8.36	6.02
2ZC	46.96	13.39	7.79	5.94	3.84	2.94	1.57
2ZD	45.30	11.78	8.72	7.86	7.51	6.75	4.88
3XB	53.68	13.55	8.17	6.34	4.96	4.11	2.63
3XC	52.42	11.56	6.91	5.41	4.00	3.17	1.93
3XD	56.11	19.05	12.74	11.33	8.79	7.82	5.27
3YB	44.11	16.10	11.47	10.09	8.87	7.97	5.75
3YC	43.20	10.93	7.09	5.90	5.05	4.34	3.13
3YD	37.79	10.57	7.04	5.89	4.89	4.14	2.97
3ZB	49.66	15.45	10.08	8.07	6.96	5.96	4.20
3ZC	51.12	14.90	10.20	8.92	7.94	7.15	5.24
3ZD	50.73	15.99	9.90	7.69	5.77	4.45	2.64

Our results show a spatial variation of J_c value in the sample grown by IG process that agrees with our previous results reported by Das et al and Iida et al. [9, 18]. The variation of J_c at self-field for 1X, 1Y and 1Z layers (calculated from the percentage difference between the minimum and maximum value of the considered layer), was around 25, 40 and 35 %, respectively. This indicates that the J_c uniformity of bulk degrades with distance from the seed. On the other hand, the J_c variation of all specimens in the layer 1, 2, and 3 was around 70.26, 42.06, and 29.60%, respectively. The high J_c variation in layer 1 results from a disparity in oxygen content in the inner and outer part of the bulk grown by IG process, due to a high density that hinders oxygen diffusion [20].

5.3.2 Variation of microstructure

In order to analyze the secondary phase embedded in the RE-123 matrix, microstructures at various positions were examined by FESEM as illustrated in Figs. 5.6 - 5.8. According to these figures, fine RE-211 secondary phase particles (light gray color) are uniformly distributed throughout the RE-123 matrix (dark gray color). It is known that the amount and morphology of RE-211 particles control the superconducting performance of RE-123 at low fields. In our samples, a large variation in RE-211 secondary phase size (few μm to several hundred nm) was observed. These results are in contradiction to some prior works reporting homogeneous dispersion and size of RE-211 particles in the bulk prepared via IG [9, 21].

The large particles can form due to accumulation of RE-211 particles before reacting with Ba-Cu-O liquid during the heating period. Therefore, the standard deviation of the particles size in layers 2 and 3 is higher than in layer 1. Especially in layer 3, the largest and smallest RE-211 particle sizes observed were 6.5 and 200 nm. We can also consider the role of unintentional and uncontrollable factors such as local temperature distribution during growth process, solid-liquid interaction during peritectic reaction, and forced reaction among the particles [22, 23]. The particle size analysis of each layer is shown in Fig. 5.9 and table 5.3.

The average particle sizes were ~ 1 μm and the number of particles in layer 1 is more than layers 2 and 3 that support the high J_c value in layer 1.

From FESEM image of layer 1 shown in Fig. 5.6, an average V_{f211} of 1X, 1Y, and 1Z specimen was estimated to be 43.57, 39.29 and 35.42 %, respectively. It was noticed that V_{f211} decreased with distance from the seed along *c*-axis. Since V_{f211} directly reflects J_c value, spatial dependence of J_c might be roughly estimated from spatial dependence of V_{f211}. In addition, it was proven that IG process provides an advantage of a lower porosity in the RE-123 matrix. From the FESEM image, it was found that the pore size was less than 1 μm. However, a non-uniformity still occurs since the size and number of pores in the bottom layer is slightly larger than in the top layer.

A gradient in color was observed in some particles in FESEM images. This is a result of an instability in RE-211 formation. This phenomenon was absent in a single-element superconductor. The color (shades of white and black) in the FESEM image reflects the element ratio in the ternary RE-211 in the same particle. These characteristics support the previous EDX results shown in chapter 4.

The conversion of the RE-211 preform to the RE-123 matrix can be effectively optimized by controlling the temperature profile. Some research groups used pre-heated RE-211 preform in order to control a porosity of pellet [21, 24, 25].

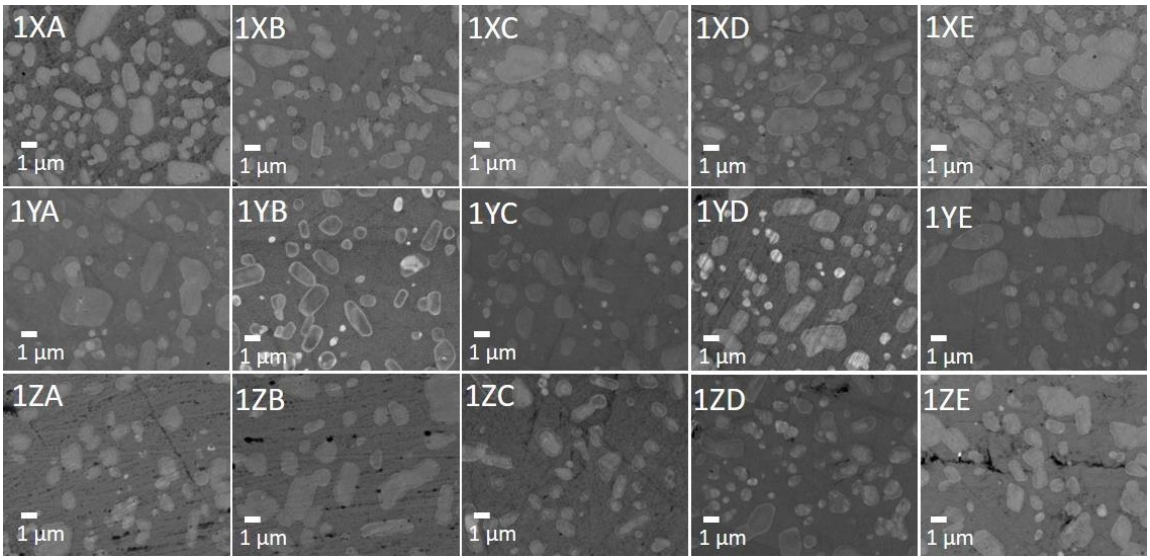

Figure 5.6 FESEM images of the layer 1

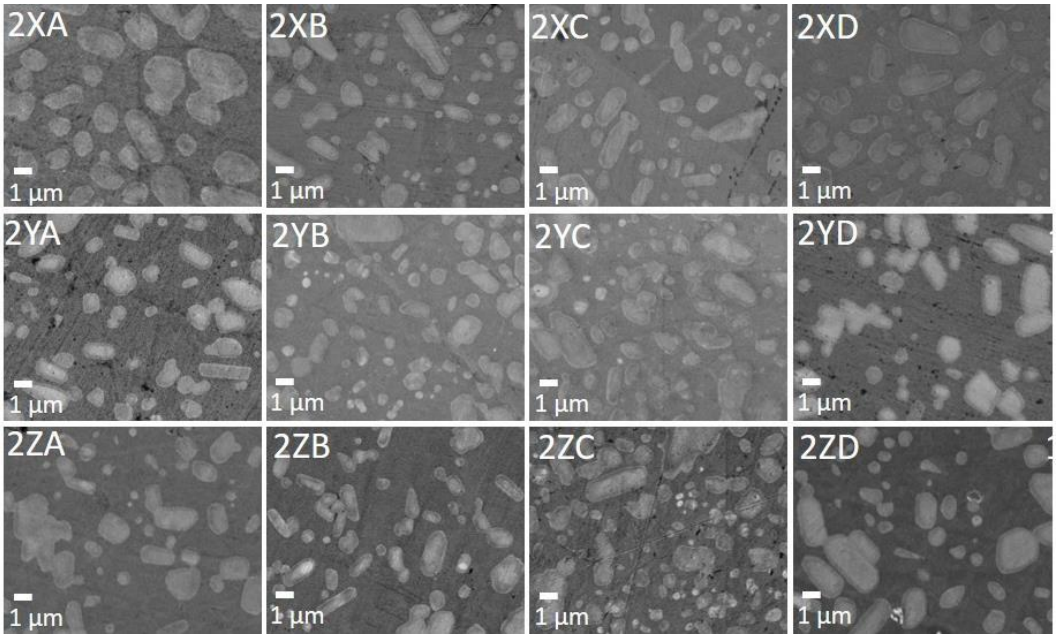

Figure 5.7 FESEM images of the layer 2

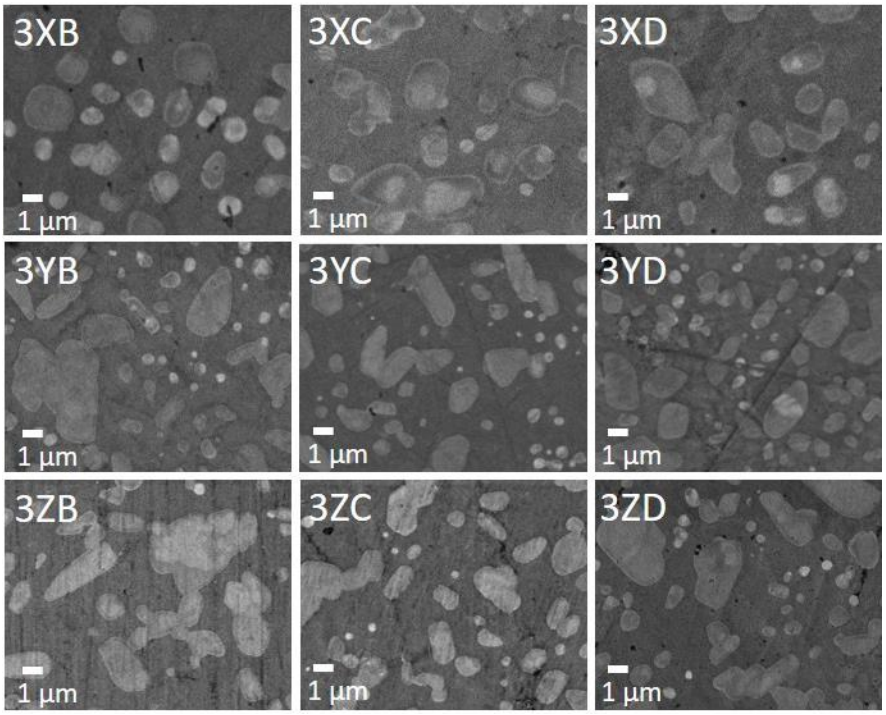

Figure 5.8 FESEM images of the layer 3

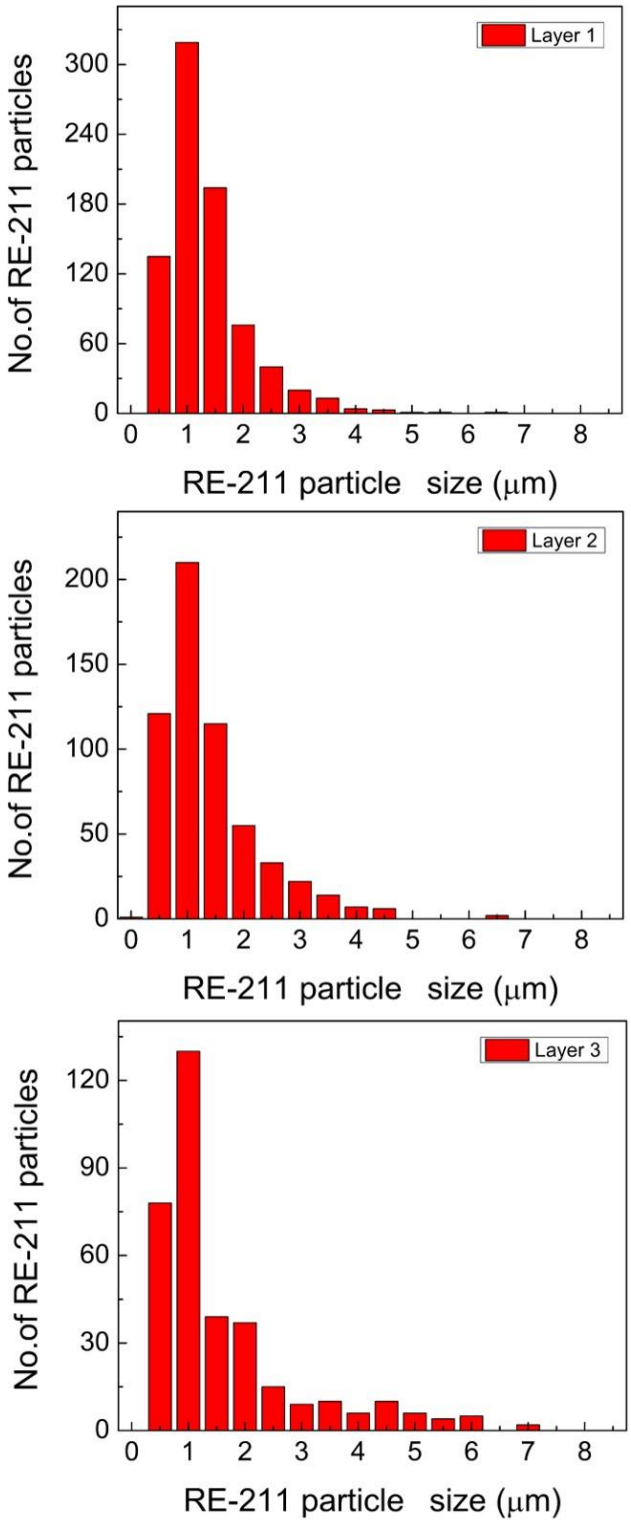

Figure 5.9 The histograms of the ($Gd_{0.33}$,$Y_{0.13}$,$Er_{0.53}$)-211 secondary particles size in each layer

Table 5.3 The secondary ($Gd_{0.33}$,$Y_{0.13}$,$Er_{0.53}$)-211 particle size at various positions

Positions	($Gd_{0.33}$,$Y_{0.13}$,$Er_{0.53}$)-211 particle (μm)		
	Minimum	Maximum	Average
1XA	0.25	3.31	0.85
1XB	0.23	2.52	1.04
1XC	0.16	4.84	0.90
1XD	0.15	2.99	0.84
1XE	0.27	2.65	1.06
1YA	0.14	4.49	1.09
1YB	0.14	2.67	0.81
1YC	0.12	5.41	0.96
1YD	0.11	2.63	0.82
1YE	0.17	2.83	0.80
1ZA	0.14	2.17	0.84
1ZB	0.36	3.90	1.44
1ZC	0.22	2.92	0.82
1ZD	0.15	3.40	1.10
1ZE	0.21	3.06	0.96
2XA	0.60	3.86	1.90
2XB	0.09	4.19	0.91
2XC	0.24	3.89	1.11
2XD	0.21	3.60	1.37
2YA	0.36	2.95	1.13
2YB	0.21	3.93	0.93
2YC	0.39	3.67	1.21
2YD	0.30	3.79	1.44
2ZA	0.15	5.59	1.08
2ZB	0.36	2.71	1.30
2ZC	0.27	3.65	1.07
2ZD	0.27	4.53	1.40
3XB	0.63	2.16	1.34
3XC	0.33	5.61	1.66
3XD	0.57	4.38	1.72
3YB	0.28	6.31	1.59
3YC	0.30	4.39	1.02
3YD	0.38	8.44	1.84
3ZB	0.38	8.44	1.84
3ZC	0.30	4.41	1.26
3ZD	0.39	4.01	1.24

5.3.3 Variation of RE-211 pellet in the processes

Due to absence of decomposition step in IG process, we expected the problem with RE-211 phase observed in the samples grown by TSMG process will be solved [4, 26]. However, according to the recent reports [18, 27], the distribution of the secondary phase in the bulk grown by IG process is similar to what we have observed with the TSMG process. Fracture surface of unreacted RE-211 preform is shown in Fig. 5.10. The initial particle sizes of Gd-211, Y-211 and Er-211 powders before mixing were less than 3 µm. The surface morphology of our RE-211 preform is similar to what was observed by A. Mahmood et al. [14] and S. Pavan et al. [24, 28]. The sample set-ups quenched at 880ºC and 1050ºC are shown in Figs. 5.11 (a) and (b), respectively. After first quenching in air at 880ºC, no infiltration or reaction was observed as shown in Fig. 5.11 (a). Due to the peritectic temperature of LP phase (Er-123 and $Ba_3Cu_5O_8$) lying between 880ºC (melting temperature of $Ba_3Cu_5O_8$) and 990ºC (peritectic temperature of pure Er-123 [29]). However, in case of quenching at 1050ºC, RE-211 pellet's color changed from green to black as shown in Fig. 5.11 (b). It indicates the reaction between RE-211 and Ba-Cu-O liquid. At this temperature, LP preform decomposes to solid RE-211 and Ba-Cu-O liquid, which infiltrates into the top RE-211 preform, and forms the RE-123 matrix. In Fig. 5.11 (c) shows the positions on the RE-211 pellet, where microstructure was characterized, are marked.

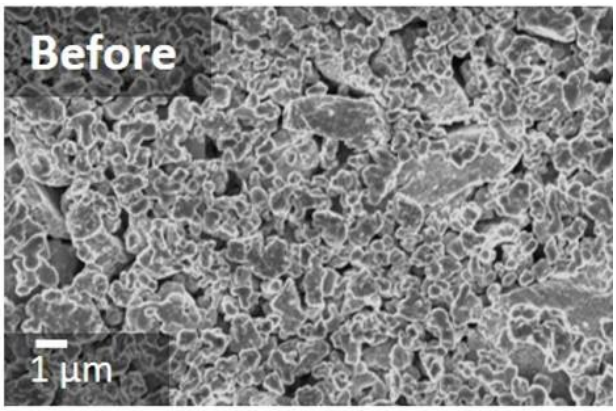

Figure 5.10 Surface morphology of RE-211 pellet before heat-up process

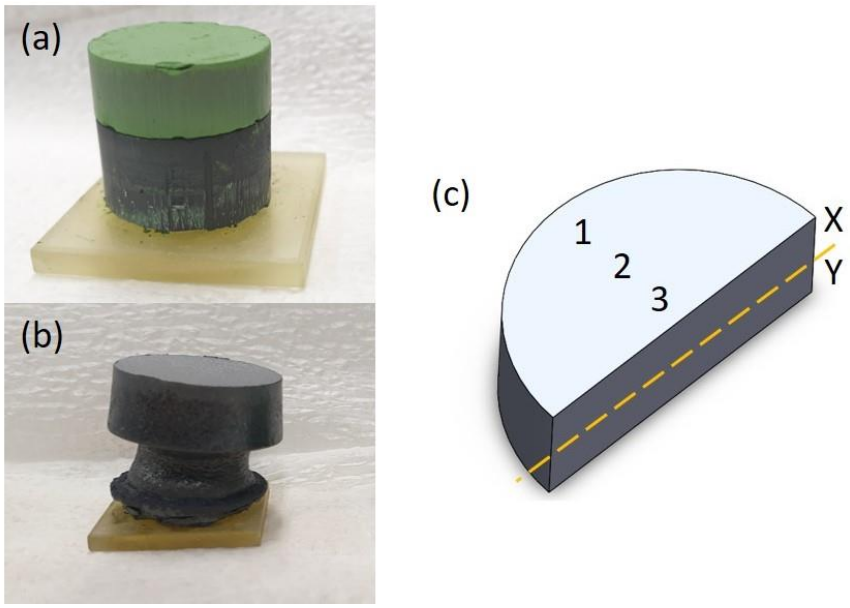

Figure 5.11 The heated samples at (a) 880ºC, (b) 1050ºC, and (c) positions of each specimen in the RE-211 preform

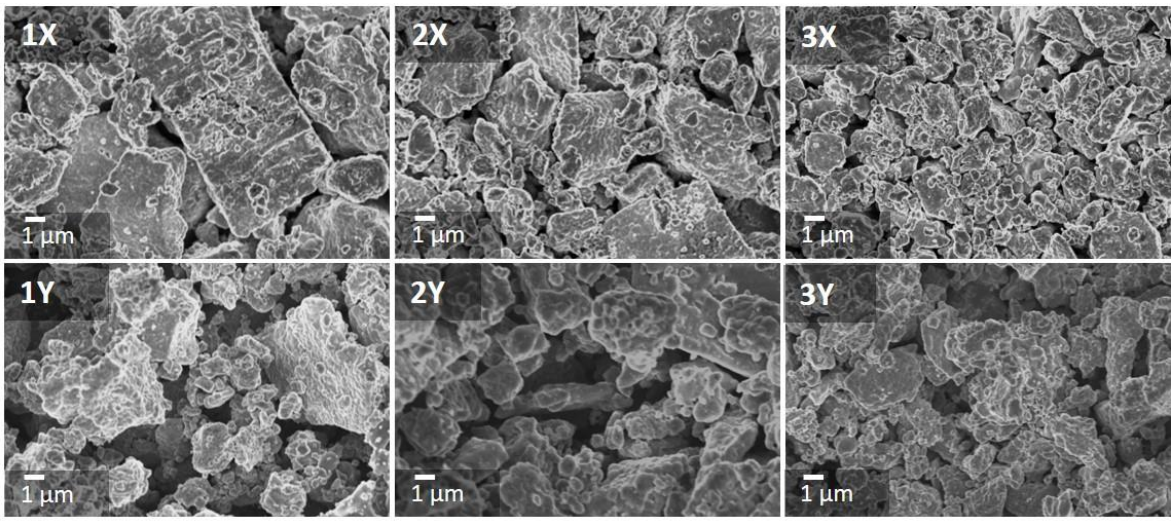

Figure 5.12 FESEM images of RE-211 pellet at various positions of sample quenched at 880ºC

In Fig. 5.11 (c), the labels X and Y refer to the top and bottom layers, respectively, and the labels 3 to 1 mark the positions apart from center. From Fig. 5.12, it is obvious that the surface morphology is totally different from the unheated RE-211 (shown in Fig. 5.10).

When heated to 880ºC, small RE-211 particles agglomerated to form large ones. The average size of unheated RE-211 particles was approximately 1-4 μm, whereas at 1X and 1Y positions, the particles size reached ~12 μm and ~8.5 μm, respectively. At the center of the bulk, in 3X and 3Y positions, the particle size was slightly larger than that in the pristine RE-211 preform. These results point out that the particles size at the periphery of the sample is larger than in the center part. The reason might be a thermal gradient, due to insufficient heat transfer from the surface to the inside of the pellet. Small particles which are closely pressed during pelletizing can coalesce or merge during high temperatures to form bigger particles [24, 28]. This in turn results in increase of porosity. It was clearly evident that the size of pores in the unheated RE-211 were smaller than that of the heated one.

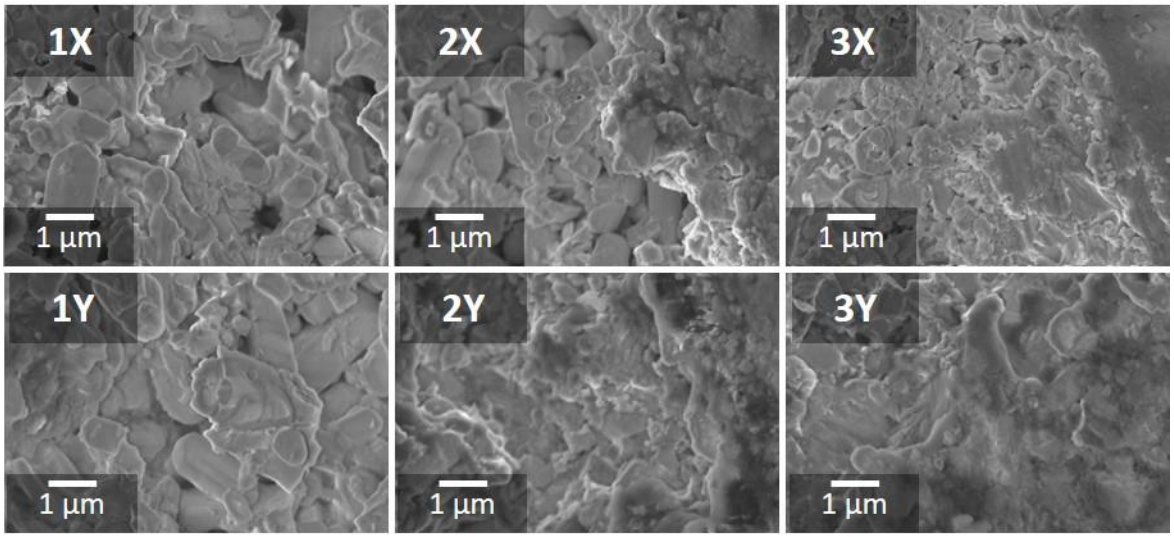

Figure 5.13 FESEM images of RE-211 pellet at various positions of sample quenched at 1050ºC

Fig. 5.13 shows the RE-211 pellet after heating up to 1050ºC and quenching to room temperature. As mentioned previously, since this temperature is higher than T_p of LP (Er-123 and $Ba_3Cu_5O_8$), LP decomposes to RE-211 and Ba-Cu-O liquid; then only Ba-Cu-O liquid infiltrates into the RE-211 preform. Therefore, at this temperature, the pores inside the RE-211 sample are filled by the Ba-Cu-O liquid. This results in a decrease of porosity observed in the surface morphology shown in Fig. 5.13. Ba-Cu-O liquid infiltrates from

bottom to top, and from the center to edge via capillary forces and chemical potential [26]. The reaction between the Ba-Cu-O liquid and RE-211 causes the spatial dependence of the surface morphology in the studied RE-211 sample.

The experimental results of surface morphology of RE-211 pellet at 880ºC and 1050ºC can be summarized as follows:

(1) Thermal effect is one of the factors for changing structural morphology in RE-211 inside the preform.

(2) Thermal gradient during the heating process and infiltration of Ba-Cu-O liquid causes non-uniformity in the RE-211 preform

(3) Large secondary phase particles are possibly formed in spite of no peritectic reaction in the IG process.

5.4 Conclusions

(i) The spatial variation of superconducting properties analyzed T_c and J_c, (ii) microstructure of bulk ($Gd_{0.33}Y_{0.13}Er_{0.35}$)$Ba_2Cu_3O_y$ (RE-123) superconductors, and (iii) the surface morphology of ($Gd_{0.33}Y_{0.13}Er_{0.35}$)$_2BaCuO_5$ (RE-211) pellet before and after IG process are investigated in this chapter. The value of T_c is almost constant over the entire sample. This indicates a sufficient amount of oxygen incorporated into the structure. J_c value at self-field along *a/b*-axis increased with increasing distance from the center, whereas the value along *c*-axis decreased. The spatial variation of J_c is caused by the non-uniform distribution of RE-211 secondary particles in the RE-123 matrix. This problem is often observed in the sample grown by TSMG process. To conclude, IG process solves several problems faced in TSMG, however, the inhomogeneity of RE-211 particles is not yet completely optimized, which leads to a non-uniformity of superconducting properties in the bulk. RE-211 preform is usually robust and is expected to be unaffected during the IG process, but, according to FESEM images, the surface morphology changes due to a heat variation during fabrication process. FESEM images revealed the size of RE-211 particles and porosity of each heat process in the structure. At the periphery, the pore size became larger due to fusion of RE-

211 particles before an infiltration of Ba-Cu-O liquid. The thermal gradient significantly affects the size of particles and pores in the RE-211 pellet.

References

1. Durrell, J.H., et al., *Bulk superconductors: a roadmap to applications.* Superconductor Science and Technology, 2018. **31**(10): p. 103501.
2. Gruss, S., et al., *Superconducting bulk magnets: Very high trapped fields and cracking.* Applied Physics Letters, 2001. **79**(19): p. 3131-3133.
3. Diko, P. and G. Krabbes, *Macro-cracking in melt-grown YBaCuO superconductor induced by surface oxygenation.* Superconductor Science and Technology, 2002. **16**(1): p. 90-93.
4. Namburi, D.K., et al., *Control of Y-211 content in bulk YBCO superconductors fabricated by a buffer-aided, top seeded infiltration and growth melt process.* Superconductor Science and Technology, 2016. **29**(3): p. 034007.
5. Kim, C.-J., Y.A. Jee, and G.-W. Hong, *Variables affecting the fabrication of single grain $YBa_2Cu_3O_{7-y}$ superconductors by the top-seeded melt growth process.* Superconductor Science and Technology, 2000. **13**(6): p. 709.
6. Jiao, Y.L., et al., *J_c–B characteristics for bulk single domain YBCO superconductors.* Physica C: Superconductivity, 2003. **386**: p. 266-270.
7. Chen, Y.L., et al., *A new method for net-shape forming of large, single-domain $YBa_2Cu_3O_{6+X}$.* Physica C: Superconductivity, 1994. **234**(3): p. 232-236.
8. Chen, S.-Y., et al., *Remarkable peak effect in $J_c(H, T)$ of Y–Ba–Cu–O bulk by using infiltration growth (IG) method.* Materials Science and Engineering: B, 2008. **151**(1): p. 31-35.
9. Das, D., et al., *Top-seeded infiltration growth of $(Y,Gd)Ba_2Cu_3O_y$ bulk superconductors with high critical current densities.* Superconductor Science and Technology, 2017. **30**(10): p. 105015.
10. Iida, K., et al., *Seeded infiltration and growth of large, single domain Y–Ba–Cu–O bulk superconductors with very high critical current densities.* Superconductor Science and Technology, 2005. **18**(11): p. 1421.
11. Pinmangkorn, S., et al., *$(Gd,Y,Er)Ba_2Cu_3O_y$ bulk superconducting system processed via infiltration growth.* Journal of Alloys and Compounds, 2021. **881**: p. 160535.

12. Bean, C.P., *Magnetization of High-Field Superconductors.* Reviews of Modern Physics, 1964. **36**(1): p. 31-39.
13. Chen, D.X. and R.B. Goldfarb, *Kim model for magnetization of type-II superconductors.* Journal of Applied Physics, 1989. **66**(6): p. 2489-2500.
14. Sai Srikanth, A., et al., *Optimization of Carbon Encapsulated Boron Doping for High-Performance Bulk Sintered MgB_2.* Advanced Engineering Materials, 2020. **22**(11): p. 2000478.
15. Pinmangkorn, S., et al., *Enhancing the superconducting performance of melt grown bulk $YBa_2Cu_3O_y$ via ultrasonically refined Y_2BaCuO_5 without PtO_2 and CeO_2.* Materials Chemistry and Physics, 2020. **244**: p. 122721.
16. Muralidhar, M., et al., *Improvement in Field Trapping Capability of (Nd,Eu,Gd)$Ba_2Cu_3O_y$ with Ag_2O Addition.* Japanese Journal of Applied Physics, 2001. **40**(11R): p. 6329.
17. Shi, Y., et al., *The growth and superconducting properties of RE–Ba–Cu–O single grains with combined RE elements (RE = Gd and Y).* Superconductor Science and Technology, 2020. **33**(3): p. 035003.
18. Iida, K., et al., *Seeded infiltration and growth of single-domain Gd–Ba–Cu–O bulk superconductors using a generic seed crystal.* Superconductor Science and Technology, 2006. **19**(7): p. S478.
19. Pinmangkorn, S., et al., *Effect of Ultra-sonicated Y_2BaCuO_5 on Top-Seeded Melt Growth $YBa_2Cu_3O_y$ Bulk Superconductor.* Journal of Superconductivity and Novel Magnetism, 2020: p. 1-7.
20. Namburi, D. and Y. Shi, *Fabrication of bulk (RE)BCO superconductors by the infiltration and growth process: past, present and future.* 2015.
21. Muralidhar, M., et al., *Microstructure, critical current density and trapped field experiments in IG-processed Y-123.* Superconductor Science and Technology, 2016. **29**(5): p. 054003.
22. Bolling, G. and J. Cisse, *A theory for the interaction of particles with a solidifying front.* Journal of Crystal Growth, 1971. **10**(1): p. 56-66.

23. Endo, A., et al., *Macrosegregation of $Y_2Ba_1Cu_1O_5$ particles in $Y_1Ba_2Cu_3O_{7-\delta}$ crystals grown by an undercooling method.* Journal of Materials Research, 1996. **11**(4): p. 795-803.
24. Mahmood, A., et al., *Pre-sintering effects on the critical current density of YBCO bulk prepared by infiltration method.* Physica C: Superconductivity, 2008. **468**(15-20): p. 1350-1354.
25. Muralidhar, M., et al., *Record critical current densities in IG processed bulk $YBa_2Cu_3O_y$ fabricated using ball-milled $Y_2Ba_1Cu_1O_5$ phase.* physica status solidi (a), 2016. **213**(2): p. 443-449.
26. Fang, H., et al., *On the study of the liquid infiltration and seeded growth process.* Superconductor Science and Technology, 2003. **17**(2): p. 269-273.
27. Iida, K., et al., *The microstructure and properties of single grain bulk Ag-doped Y–Ba–Cu–O fabricated by seeded infiltration and growth.* Physica C: Superconductivity, 2008. **468**(15): p. 1387-1390.
28. Pavan Kumar Naik, S., et al., *Infiltration growth processing of bulk mixed $REBa_2Cu_3O_{7-x}$ superconductors: nano-metal oxides and rare earth elements effects on microstructural properties.* Superconductivity and Particle Accelerators 2018, 2019. **11054**: p. 110540H.
29. Murakami, M., *Melt processed high-temperature superconductors*. Vol. 9. 1992: World Scientific.

Chapter 6

(Gd,Y,Er)$Ba_2Cu_3O_y$ Superconductors with Ultra-sonicated Secondary Phase Particles

6.1 Introduction

For a good superconducting performance it is necessary to achieve a high superconducting critical current density (J_c) and trapped field (TF) at high temperatures and high magnetic fields [1]. Critical current density can be improved by reducing the size of RE_2BaCuO_5/RE-211 secondary phase particles and controlling the homogeneity of RE-211 distribution in the RE-123 matrix [2]. Microstructural defects contribute to magnetic flux pinning and enhance J_c and TF [3]. The effect of RE-211 precipitates is usually observed at low magnetic fields as they contribute as δl pinning and hence result in a high self-field critical current density. On the other hand, in bulk superconductors, point-like

defects and oxygen off-stoichiometric phases result in peak effect at high magnetic fields [4, 5]. The refinement of RE-211 (RE: Gd,Y,Er) secondary phase particles being dispersed in bulk RE-123 superconductors has been utilized using e.g. adding grain growth inhibitor agents like Pt, CeO_2, etc. [6, 7]. Ball-milling is also widely used to refine the RE-211 secondary particles, but this method produces undesirable impurities [8, 9]. The alternative technique to refine RE-211 particle is the high-energy ultra-sonication that generates powerful waves using vibrations [10, 11]. These ultra-sonic waves cause turbulence in the medium and pass the energy to the particles which leads to separation and size reduction of the particles [12, 13]. Combination of grain refinement agents and ultra-sonication technique can result in high-performance bulk RE-123 superconductors.

From our previous studies, we learned that 80 minutes of ultra-sonication with constant power of 300W and 20 kHz frequency resulted in optimum refinement of RE-211 particles [11]. The ternary bulk (Gd,Y,Er)-123 superconductor has been prepared by infiltration growth "IG" process in air. The Gd-211, Y-211, and Er-211 powders treated in this chapter were refined via ultra-sonication for 80 minutes, then pelletized into preforms, and studied systematically while varying the composition, similar to chapter 4. The superconducting performance, microstructure and trapped field measured at liquid nitrogen on the IG-processed (Gd,Y,Er)-123 material produced of ultra-sonicated (Gd,Y,Er)-211 powder were investigated. Since we used the ultra-sonicated powder (much finer than regular calcined powders), we expected improvement in the superconducting performance.

6.2 Experimental details

The effect of refinement via ultra-sonication technique on RE-211 particles was analyzed by field-emission scanning electron microscope (FESEM). The ultra-sonicated Gd-211, Y-211, and Er-211 powders were mixed in molar ratio of $(Gd_{0.33},Y_{0.33-X},Er_{0.33+X})$-211, where X = 0, 0.05, 0.01, 0.15, and 0.2, and 0.5 wt% of PtO_2 was added to prepare the RE-

211 pellet. The liquid phase (LP) was made of Er123 and $Ba_3Cu_5O_8$ mixed in 1:1 ratio. All the preforms were pelletized using a 20 mm diameter die under an applied pressure of 70 MPa. These pellet preforms were used to fabricate the single-grain (Gd,Y,Er)-123 bulk superconductors via IG process. The as-grown bulks were referred to as XU0, XU0.05, XU0.1, XU0.15, and XU0.2 respective to the molar ratio of RE-211 powders used in the preform. The temperature profile for fabrication of (Gd,Y,Er)-123 bulk samples was same as in chapter 4 (fig 4.2(b)). The oxygen annealing was done for 400 h at 500-375°C in continuous oxygen flow (flow rate = 0.3 l/min). The trapped field was measured by field cooling method at 77.3 K under a field of 0.45 T. The Hall probe was placed 0.3 and 1.3 mm above the top surface for scanning the TF value. The superconducting critical temperature (T_c) was determined using SQUID, Model MPMS5. The field dependence of the critical current density (J_c) was calculated using extended Bean's critical state model, from *M-H* loops, H//*c*-axis measured at constant temperature [14]. Investigation of the microstructure was carried out using FESEM.

6.3 Results and discussion

6.3.1 Ultra-sonicated secondary phase particle analysis

The FESEM images of calcined and ultra-sonicated (for 80 minutes) Gd-211, Y-211, and Er-2111 powders are displayed in Fig. 6.1. One can observe that the calcined (Gd,Y,Er)-211 powders agglomerate and particles are larger than 5 µm, while the ultra-sonicated RE-211 powders consist of particles much smaller and well dispersed. The average size of the ultra-sonicated Gd-211, Y-211 and Er-211 powders was around 1-3 µm, 1-0.7 µm and 200-500 nm, respectively. For more comprehensive view, high magnification of FESEM images of ultra-sonicated Gd-211, Y-211 and Er-211 powders were displayed in Figs. 6.2(a)-(c), respectively. Ultra-sonicated Gd-211 particles were largest, whereas the Er-211 ones were smallest. Further, Gd-211 and Y-211 exhibited different sharp edges. The smallest Er-211 particles experienced better ultra-sonication effect compared to Gd-211 and Y-211. Nano-sized ultra-sonicated Er-211 powder was depicted in Fig. 6.2(c). On the

other hand, ultra-sonication time with constant power and frequency should be properly optimized for Gd-211 and Er-211 powders for best refinement. The optimization is usually related to the bombarding energy as well as frequency of ultrasound [15, 16].

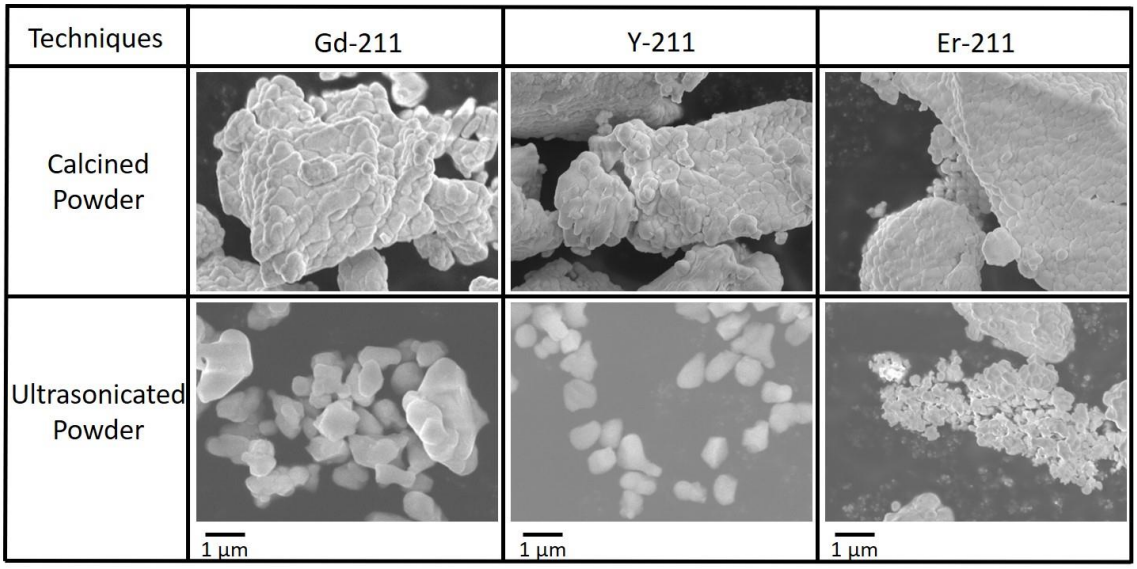

Figure 6.1 FESEM images of calcined and ultra-sonicated Gd-211, Y-211 and Er-211 powders

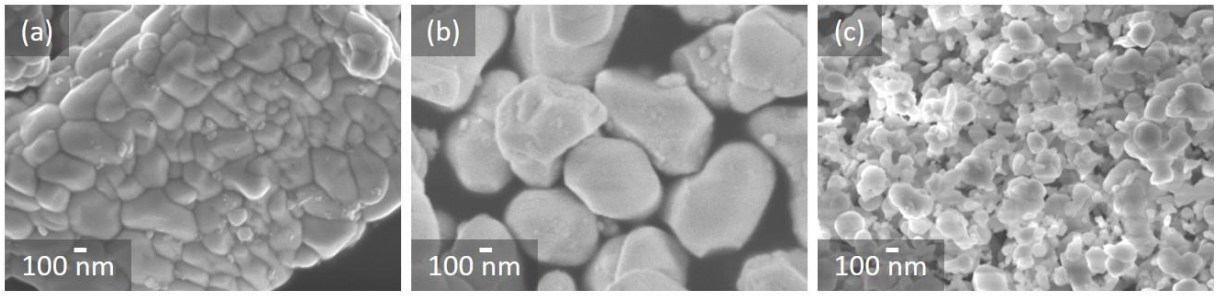

Figure 6.2 High magnification of FESEM images of ultra-sonicated Gd-211, Y-211 and Er-211 powders

6.3.2 Fabrication of bulk (Gd,Y,Er)$Ba_2Cu_3O_y$ superconductors

The top view of as-grown samples is shown in Figs 6.3(a)-(e). No spontaneous satellite grain nucleation was observed, and all the bulks exhibited four-fold growth sector boundaries on their top surfaces that indicates single grain nature.

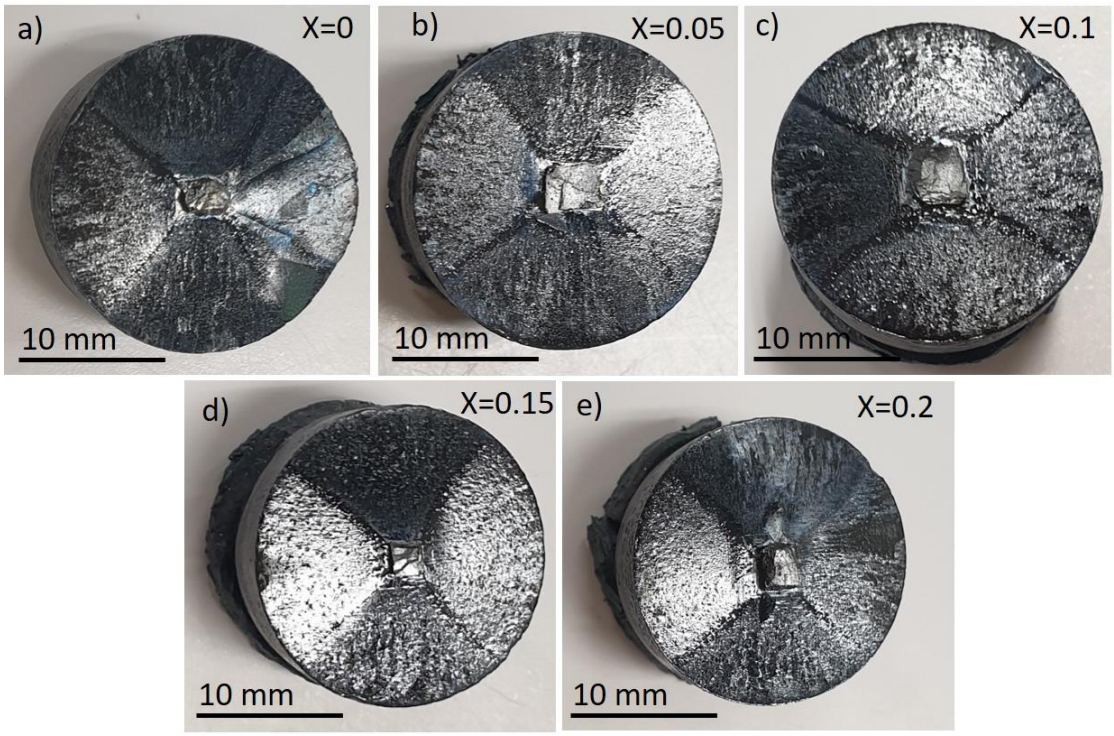

Figure 6.3 As-grown bulk ($Gd_{0.33}$,$Y_{0.33-X}$,$Er_{0.33+X}$)$Ba_2Cu_3O_y$ superconductors

6.3.3 Trapped field experiments

For measuring trapped field, all the samples were field cooled by liquid nitrogen (77.3 K) at the applied magnetic field of 0.45 T of a properly sized permanent magnet. Hall sensor was placed 0.3 mm above the surface (surface touched) of bulk samples XU0, XU0.05, XU0.1, XU0.15, and XU0.2, which showed TF values of 0.32, 0.36, 0.35, 0.33, and 0.37 T. At 1.3 mm distance above the sample surface, the TF values reached 0.22, 0.24, 0.25, 0.24, and 0.29 T, respectively. The trapped field values slightly increased with increase in Er concentration in bulk $(Gd_{0.33}Y_{0.33-x}Er_{0.33+x})$-123 samples, similar to results observed in the $(Gd_{0.33}Y_{0.33-x}Er_{0.33+x})$-123 samples fabricated with calcined (Gd,Y,Er)-211 powder. The trapped field distribution profiles of $(Gd_{0.33}Y_{0.33-x}Er_{0.33+x})$-123 samples measured at 77.3 K are depicted in Figs 6.4(a)-(e). All the samples show the single-cone peak behavior confirming the single-grain character without cracks [17, 18]. The bulk (Gd,Er,Y)-123 superconductor fabricated with ultra-sonicated (Gd,Y,Er)-211 powders exhibited better trapped field values than with common calcined (Gd,Y,Er)-211 powder. It shows an improvement of trapped field value with achieving smaller and more uniform (Gd,Y,Er)-211 secondary phase particles in the (Gd,Y,Er)-123 matrix due to IG processing and using ultra-sonicated powder precursors.

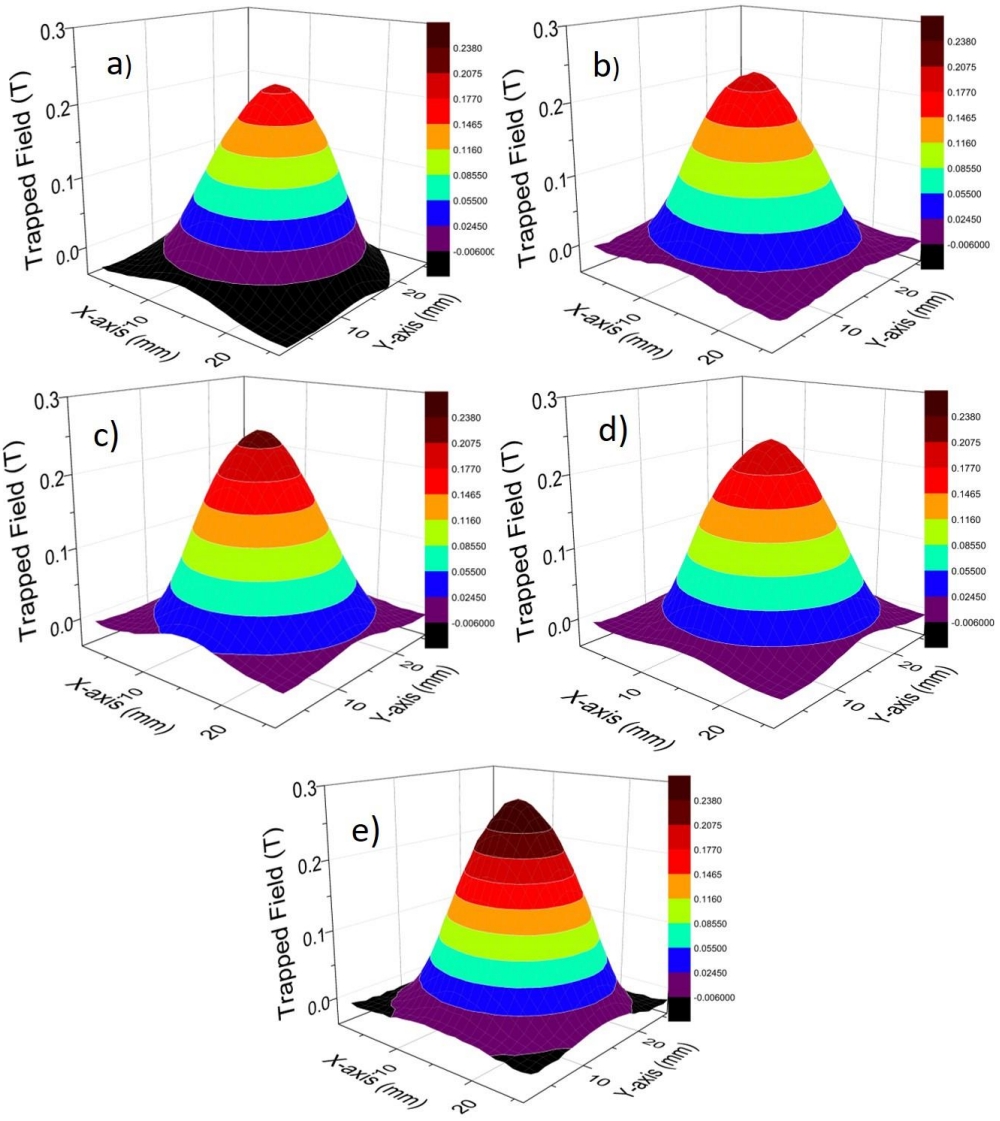

Figure 6.4 Trapped field distribution profiles of (a) XU0, (b) XU0.05, (c) XU0.1, (d) XU0.15, and (e) XU0.2

6.3.4 Superconducting properties

Fig. 6.5 shows superconducting transition temperature of bulk $(Gd_{0.33},Y_{0.33-x},Er_{0.33+x})Ba_2Cu_3O_y$ superconductors determined from measuring temperature dependence of DC susceptibility in zero field cooled (ZFC) mode and field-warming at 1 mT. XU0, XU0.05, XU0.1, XU0.15, and XU0.2 samples exhibited $T_{c,onset}$ at 92.07, 91.07, 90.66, 91.66, and 91.68 K, respectively, close to the $T_{c,onset}$ of bulk (Gd,Y)-123 and Y-123 superconductors [17, 19-21]. The superconducting transition was ~1 K wide. This implies a successful production of contamination-free ultra-sonicated (Gd,Y,Er)-211 powders and suppression of the unwanted RE/Ba solid solution in the final bulk [22, 23]. According to these results, it can be stated that ultra-sonication technique does not affect the superconducting transition temperature.

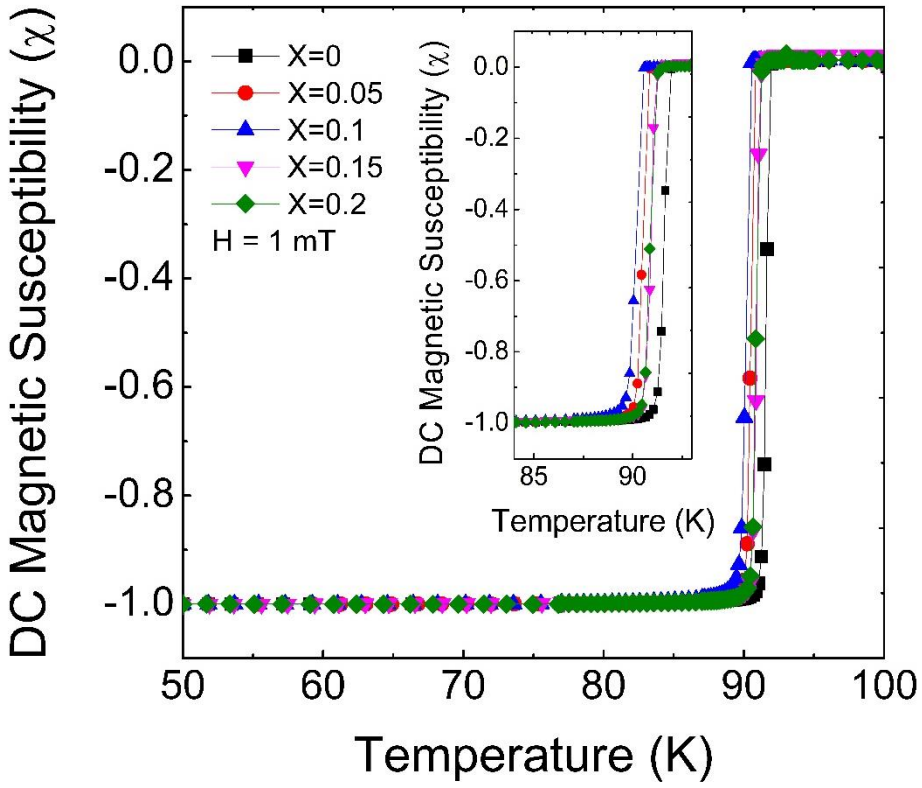

Figure 6.5 The temperature dependence of the normalized DC susceptibility measurements

The *M-H* loops were measured at 77 K and J_c was calculated using the extended Bean critical state model [14]. Fig. 6.6 shows the field dependences of J_c for $(Gd_{0.33},Y_{0.-33-x},Er_{0.33+x})$-123 samples obtained by SQUID magnetometer. The XU0.2, which is highest Er concentration sample, showed the highest self-field J_c value at 77 K (H// *c*-axis), 75.56 kA/cm^2, while the XU0 exhibited the lowest self-field J_c value, around 63 kA/cm^2. The J_c values increased with increasing Er-211 concentration in the (Gd,Y,Er)-211 preform, similar to J_c results of the (Gd,Y,Er)-123 fabricated with calcined (Gd,Y,Er)-211 powders. The improvement of J_c values in $(Gd_{0.33},Y_{0.33-x},Er_{0.33+x})$-123 samples is related to the Er concentration. There are two possible reasons: first, the peritectic temperature in the (Gd,Y,Er)-123 system decreased with increasing Er-211 content as it has the lowest peritectic temperature among other RE members. Second, Er-211 allows for the best refinement by ultra-sonication amongst all others and thus the increase of Er-211 content in the (Gd,Y,Er)-211 preform leads to an overall reduction of the 211 grains in the final bulk and an increment in self-field J_c.

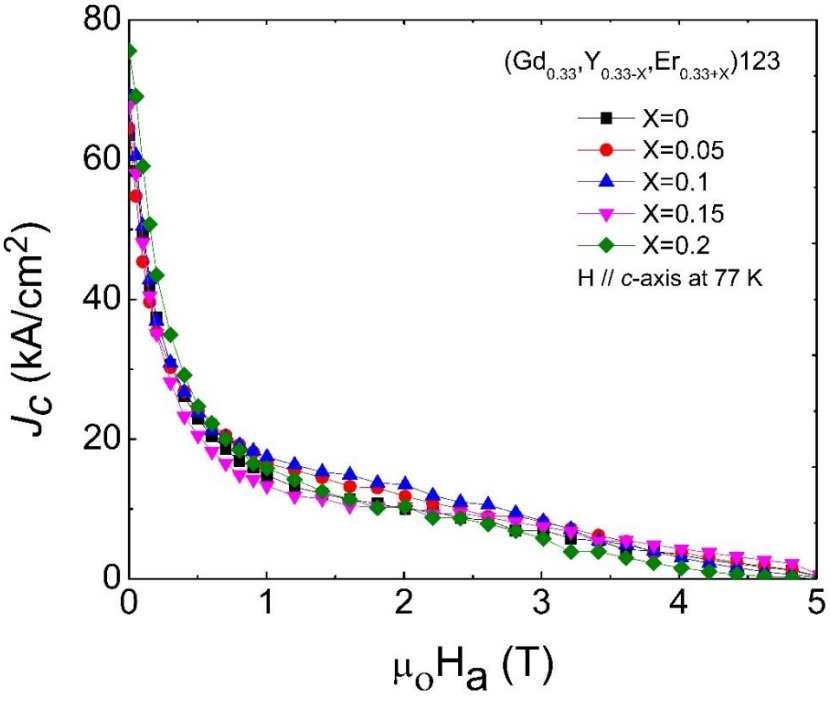

Figure 6.6 Field dependences of the critical current density (J_c) at 77 K, H //*c*-axis

The self-field J_c values of XU0.2 sample at 50, 55, 60, 65, and 70 K were 226.80, 192.35, 163.62, 136.27, 110.36 kA/cm^2, respectively, and the J_c value even at 4.5 T and 50 K was ~100 kA/cm^2, as shown in Fig.6.7. These results piont out to the wide range of applicability of the optimized (Gd,Y,Er)-123 in real applications at various temeperatures and fields. The J_c value of the ternary bulk (Gd,Y,Er)-123 superconductor prepared by IG process was higher than in binary systems (Gd,Y)-123, (Gd,Dy)-123 [21, 22, 24], as well as single-element systems Y-123, Er-123 [25, 26] at self-field, high field, and also at various temperatures.

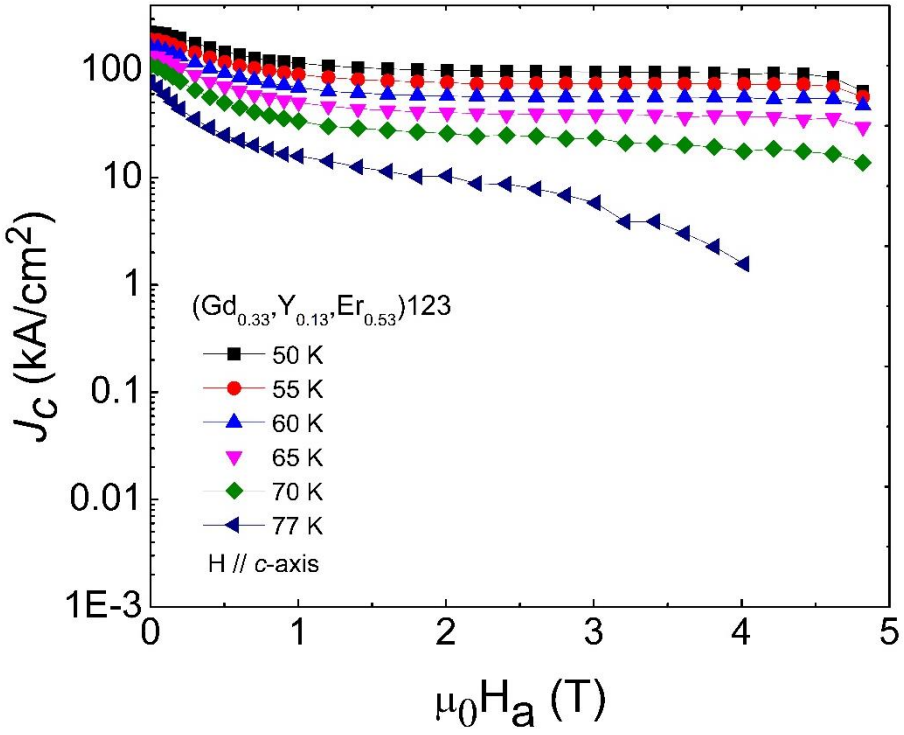

Figure 6.7 J_c values at 77, 70, 65, 60, 55, and 50 K, H // *c*-axis of $(Gd_{0.33},Y_{0.13},Er_{0.53})$-123, (XU0.2) sample

6.3.5 Microstructure analysis

Microstructures of (Gd,Y,Er)-123 samples with various ratios of Er and Y are shown in Figs. 6.8 (a)-(e). It can be seen that the (Gd,Y,Er)-211 particles are homogeneously distributed in the (Gd,Y,Er)-123 matrix. One can also observe different sizes and shapes of (Gd.Y,Er)-211 particles. Most (Gd.Y,Er)-211 particles were round, the particles larger than 3 μm were rectangular. The (Gd.Y,Er)-211 particles in Fig. 6.8 (e) are extremely fine and uniform, which is likely the reason of the highest J_c value in this series. For good pinning properties it is very important to control the RE-211 particle size and their distribution in the RE-123 matrix [27]. These microstructural results clearly justify the superconducting properties (J_c value and TF) and the highest J_c value and TF exhibited by XU0.2 sample showing the finest RE-211.

The microstructure along with element composition line scans of XU0 and XU0.2 samples are depicted in Fig. 6.9. The scanning lines on the microstructure were chosen so that it included both the (Gd,Y,Er)-211 secondary phase particles and (Gd,Y,Er)-123 matrix. Different colors of spectra correspond to different elements. According to the spectral analysis, the secondary particles show a varying ratio of Gd, Y, and Er elements. This confirms the chemical fluctuation of RE elements (Gd, Y, and Er) in the RE-211, which was also observed in few reports by other authors [20, 23]. Points 1 and 2 on the Fig. 6.8 (b) contain all three RE elements, but they are Y-rich and Er-rich, respectively. The points 3 and 4 of XU0.2 sample were focused on large secondary phase particles that showed inhomogeneous RE distribution. The dark areas (supposedly matrix) comprised of Gd, Y, and Er elements in equal ratio, whereas the bright areas (RE-211) were Er-rich. This analysis indicates different types of secondary phase particles in the studied compositions.

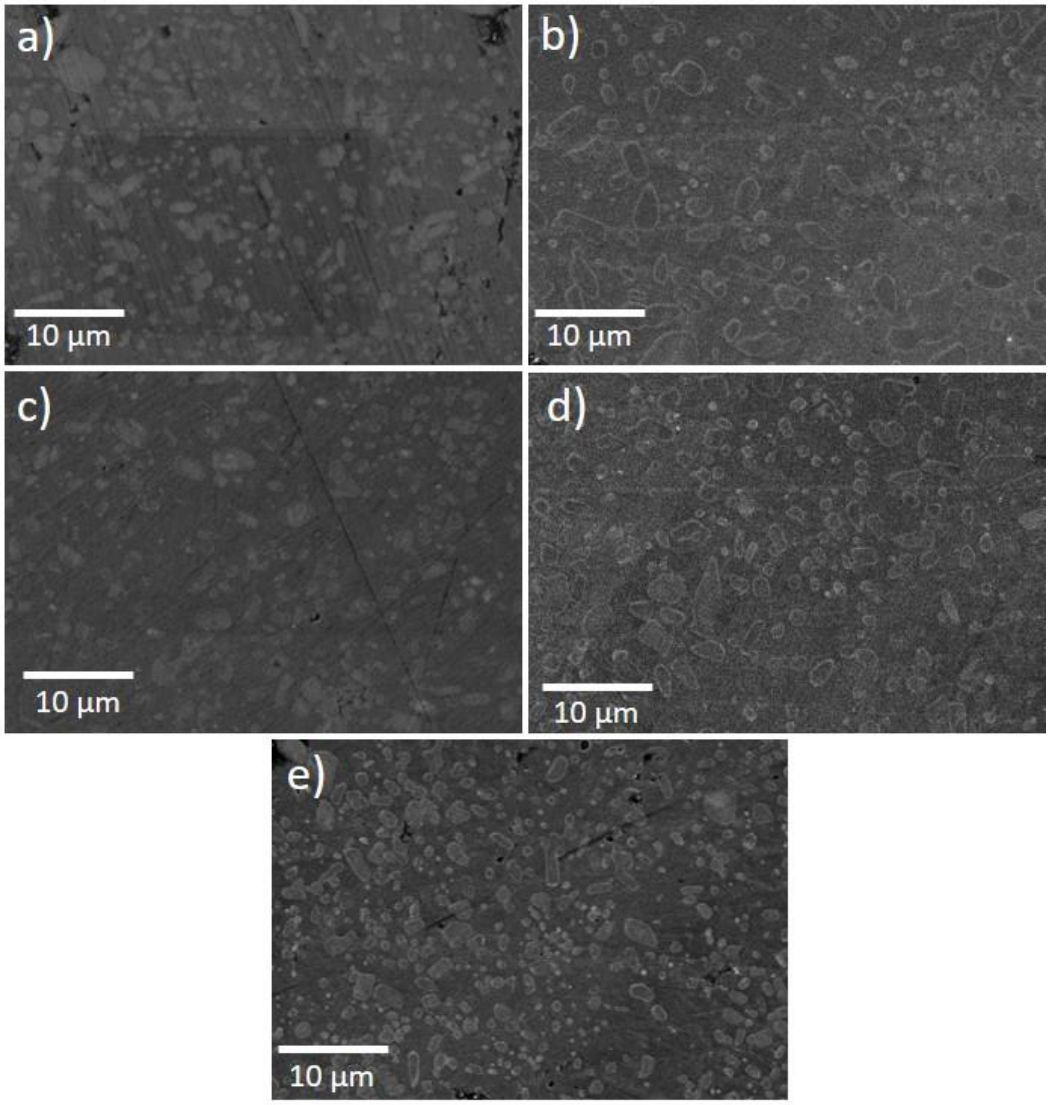

Figure 6.8 FESEM images for (a) XU0, (b) XU0.05, (c) XU0.1, (d) XU0.15, and (e) XU0.2 samples

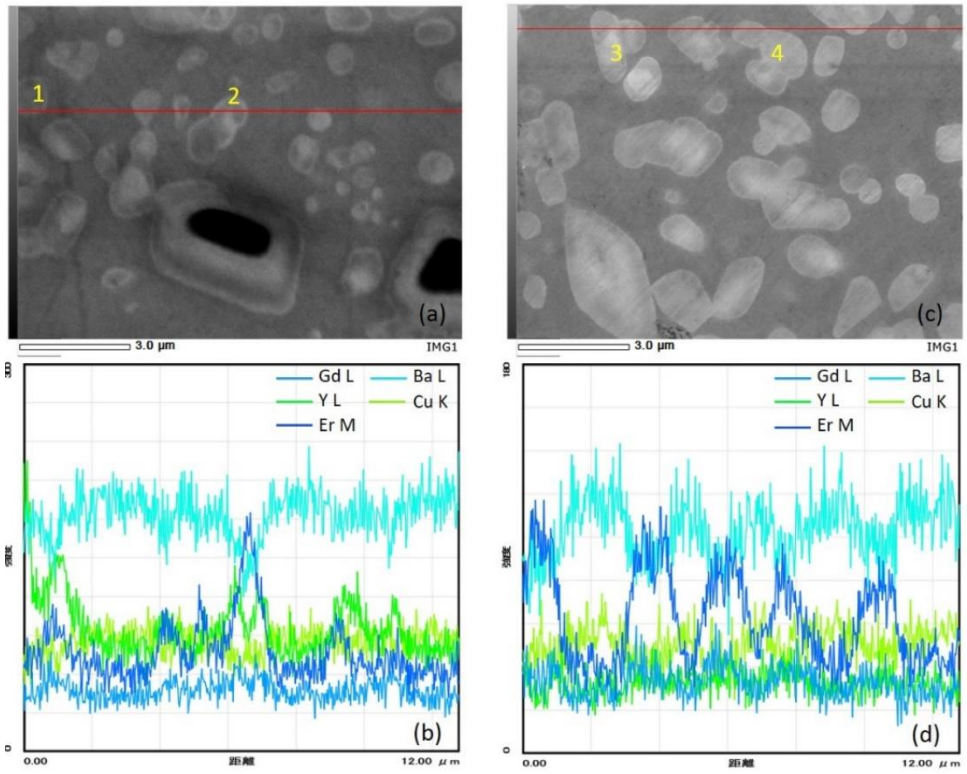

Figure 6.9 EDX line scan analysis of microstructure and individual element line spectra of (a) and (b) for XU0 sample, (c) and (d) for XU0.2 sample

6.4 Batch production of bulk ($Gd_{0.33}$,$Y_{0.13}$,$Er_{0.53}$)-123

With the bulk ($Gd_{0.33}$,$Y_{0.13}$,$Er_{0.53}$)-123 superconductor exhibiting the best values of trapped field and J_c (see Fig. 6.4 ang Fig 6.6), we tested production of a large number of samples at a single run. It would considerably reduce the production cost needed for industrial applications. The bulk ($Gd_{0.33}$,$Y_{0.13}$,$Er_{0.53}$)-123 samples were processed in a normal box furnace with a useable volume of 21 x 15 x 16 cm^3, i.e. in the laboratory scale. First, three samples were placed in the furnace (with a uniform temperature distribution (Figs 6.10(a)-(b))). In the second batch, six samples (Figs 6.11(a)-(b)) were fabricated by optimizing the temperature profile. To verify the samples' performance, trapped field

performance was measured at 77.3 K (liquid nitrogen temperature) after applying the external field of 1 T.

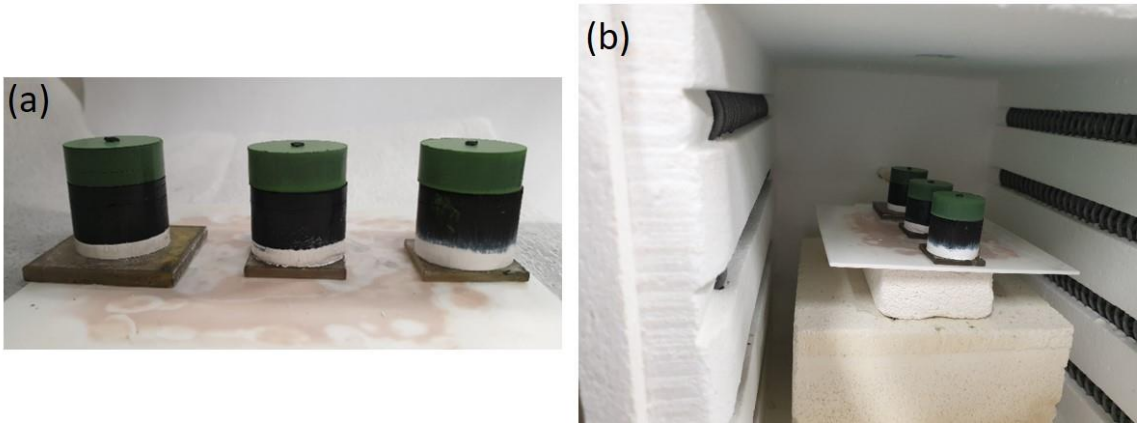

Figure 6.10 Three samples of the first batch production of (a) ($Gd_{0.33}$,$Y_{0.13}$,$Er_{0.53}$)-123 preform for IG process and (b) set-up samples in the normal box furnace

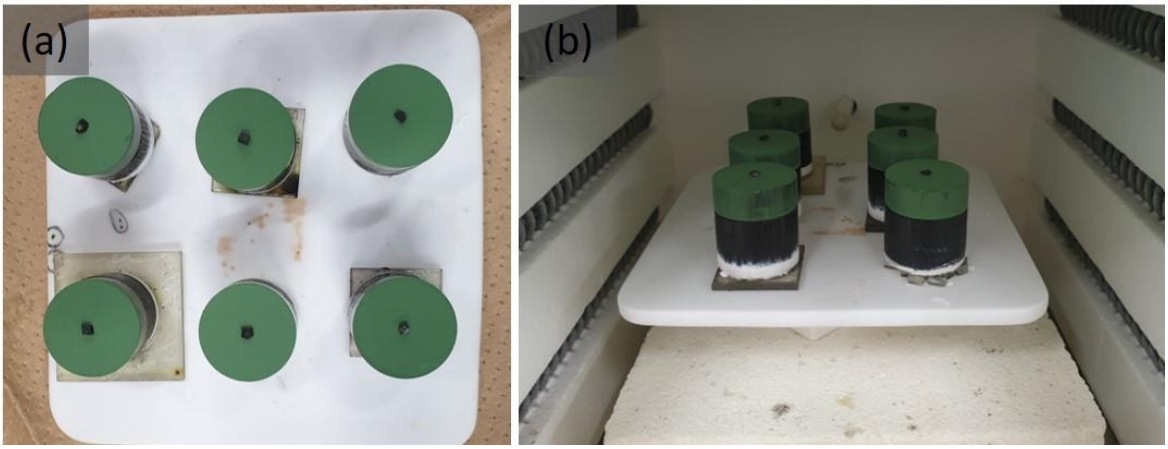

Figure 6.11 Six samples of the second batch production of (a) ($Gd_{0.33}$,$Y_{0.13}$,$Er_{0.53}$)-123 preform for IG process and (b) set-up samples in the normal box furnace

The batch production of single-grain samples grown by infiltration growth process in the normal box furnace is shown in Fig. 6.12-6.13. These samples grew fully into single-grains form without spontaneous nucleation, with the typical four-fold growth facet

running from the seed. All the samples were prepared by the IG process in a conventional furnace in air, employing cold-seeding technique.

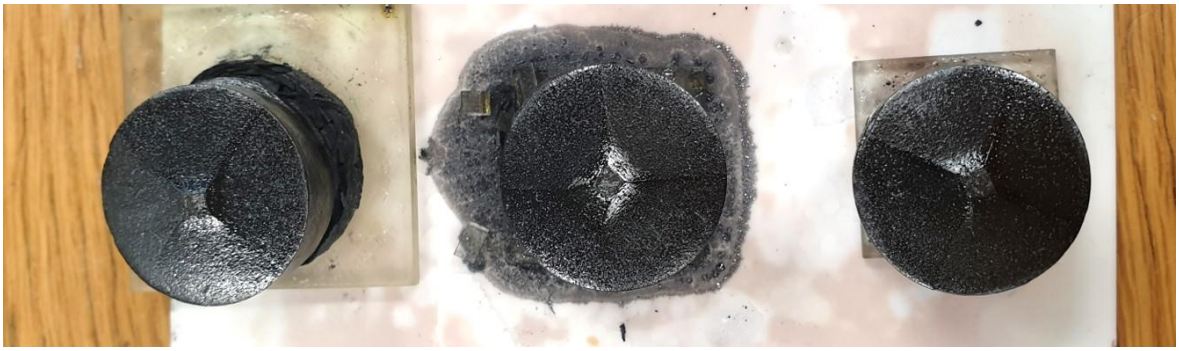

Figure 6.12 Top view of as-grown ($Gd_{0.33}$,$Y_{0.13}$,$Er_{0.53}$)-123 bulk samples for the first batch production

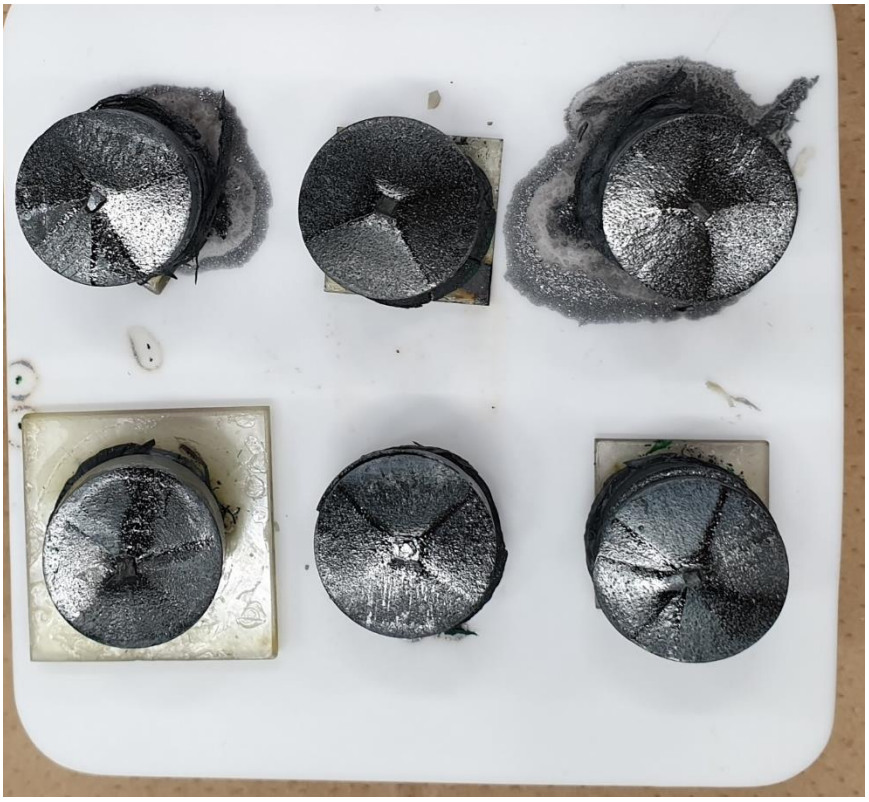

Figure 6.13 Top view of as-grown ($Gd_{0.33}$,$Y_{0.13}$,$Er_{0.53}$)-123 bulk samples for the second batch production

We measured trapped field of each sample 0.3 mm above top surface at 77.3 K, after applying external field of 1 T as shown in Fig. 6.14. Sample No.1 showed the maximum value of a single cone trapped magnetic field 0.65 T (see Fig 6.15). Remaining 5 samples showed trapped field higher than 0.5 T. The present results indicate that mixed bulk (Gd,Y,Er)-123 superconductors can be produced by IG process in batch regime, which will be crucial for the scale-up to industrial production.

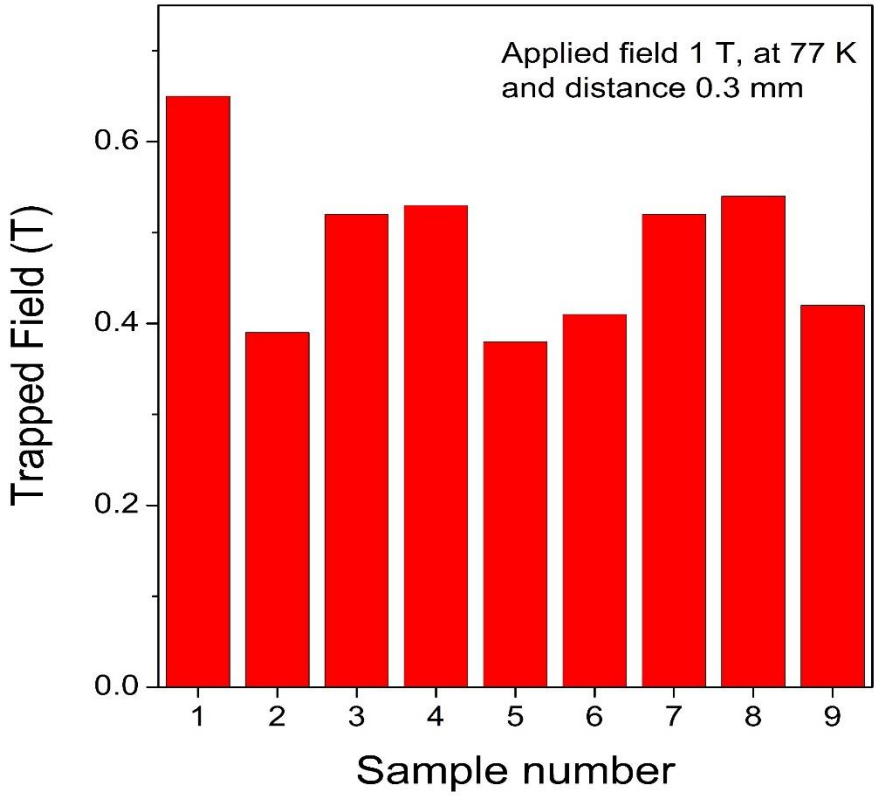

Figure 6.14 The trapped field values of each bulk $(Gd_{0.33},Y_{0.33-x},Er_{0.33+x})Ba_2Cu_3O_y$

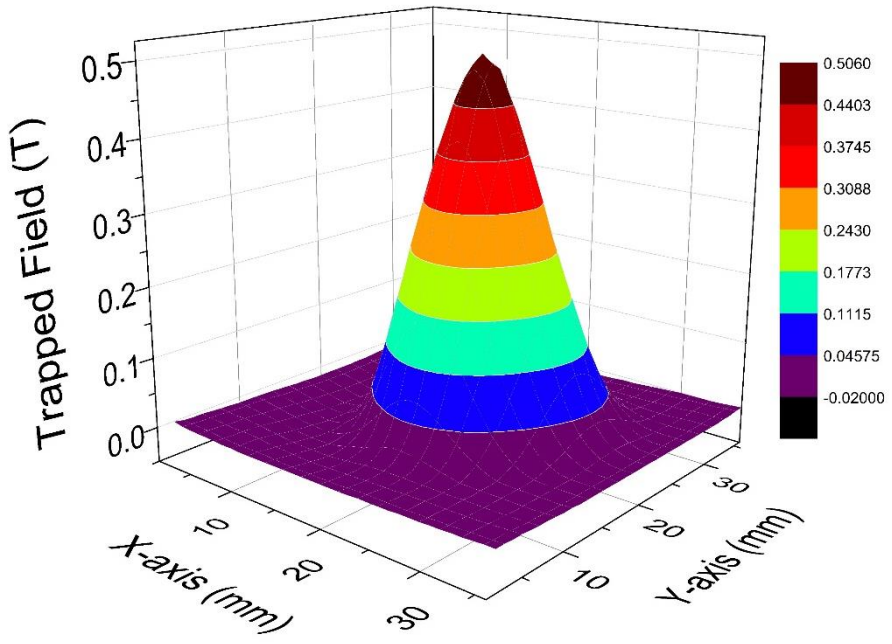

Figure 6.15 The trapped field profile at 77.3 K for bulk $(Gd_{0.33},Y_{0.33-x},Er_{0.33+x})Ba_2Cu_3O_y$ of diameter 20 mm.

6.5 Conclusions

The ultra-sonication technique enables the refinement of initial Gd-211, Y-211, and Er-211 secondary phase particles. In this study, the ternary bulk $(Gd_{0.33},Y_{0.33-x},Er_{0.33+x})Ba_2Cu_3O_y$ samples were fabricated by IG process from the preform made of ultra-sonicated (Gd,Y,Er)-211 powder. The fully grown bulk samples and trapped field distribution profiles clearly showed the single-grain nature of the bulks. The good quality of bulk (Gd,Y,Er)-123 samples was confirmed by a sharp superconducting transition with an average $T_{c,onset}$ of 91.42 K. The highest trapped field and J_c were achieved in XU0.2 ($(Gd_{0.33}Y_{0.13}Er_{0.53})$-123) sample. TF values up to 0.37 and 0.29 at 77.3 K, 0.3 and 1.3 mm above top surface were observed, respectively (the applied field was 0.45 T). The self-field J_c of the bulk was 75.56 kA/cm^2 at 77 K and 226.80 kA/cm^2 at 50 K. We can see approximately 20% improvement in J_c value at self-field, mainly due to the ultra-sonically

refined RE-211 preform. Microstructure revealed a homogeneous distribution of (Gd,Y,Er)-211 particles in the (Gd,Y,Er)-123 matrix. XU0.2 (high Er concentration) sample shows large number of fine (Gd,Y,Er)-211 particles that resulted in a significant improvement in the superconducting performance. Chemical analysis indicated RE compositional fluctuations in the secondary phase particles as well as in (Gd,Y,Er)-123 matrix. To achieve the batch production, we has demonstrated the feasibility of fabrication bulk ($Gd_{0.33}$,$Y_{0.13}$,$Er_{0.53}$)-123 superconductors for batch production. In order to reduce production cost of production, the normal furnace that can generate a stable, uniform temperature, were employed for fabricate large number of samples. We have successfully produced nine single grain samples and exhibit good trapped field ability. The fabrication of ternary bulk (Gd,Y,Er)-123 superconductor by IG process and ultra-sonication technique illustrate the significant potential for batch production due to the technique's low cost and time effectiveness.

References

1. Campbell, A.M. and D.A. Cardwell, *Bulk high temperature superconductors for magnet applićations.* Cryogenics, 1997. **37**(10): p. 567-575.
2. Koblischka-Veneva, A., et al., *Crystallographic Orientation of $Y_2Ba_4CuMO_x$ (M=Nb, Zr, Ag) Nanoparticles Embedded in Bulk, Melt-Textured YBCO Studied by EBSD.* Journal of the American Ceramic Society, 2007. **90**(8): p. 2582-2588.
3. Muralidhar, M., et al., *New Type of Vortex Pinning Structure Effective at Very High Magnetic Fields.* Physical Review Letters, 2002. **89**(23): p. 237001.
4. Muralidhar, M., et al., *Pinning characteristics in chemically modified (Nd,Eu,Gd)–Ba–Cu–O superconductors.* Applied Physics Letters, 2003. **82**(6): p. 943-945.
5. Muralidhar, M., et al., *Enhancement of J_c by 211 particles in ternary $(Nd_{0.33}Eu_{0.33}Gd_{0.33})Ba_2Cu_3O_y$ melt-processed superconductors.* Applied Physics Letters, 2000. **76**(1): p. 91-93.
6. Kim, C.-J., et al., *Microstructure of melt-textured Y-Ba-Cu-O oxides with addition and the formation mechanism of the Ba-Cu-O platelet structure.* Superconductor Science and Technology, 1996. **9**(2): p. 76-87.
7. Muralidhar, M., et al., *Influence of combined Pt and CeO_2 additions on microstructure and magnetic properties in (Nd,Eu,Gd)-Ba-Cu-O.* Superconductor Science and Technology, 2001. **14**(10): p. 832.
8. Muralidhar, M., et al., *Vortex pinning by mesoscopic defects: A way to levitation at liquid oxygen temperature.* Applied Physics Letters, 2003. **83**(24): p. 5005-5007.
9. Iida, K., et al., *The effect of nano-size ZrO_2 powder addition on the microstructure and superconducting properties of single-domain Y–Ba–Cu–O bulk superconductors.* Superconductor Science and Technology, 2004. **18**(3): p. 249-254.
10. Pinmangkorn, S., et al., *Enhancing the superconducting performance of melt grown bulk $YBa_2Cu_3O_y$ via ultrasonically refined Y_2BaCuO_5 without PtO_2 and CeO_2.* Materials Chemistry and Physics, 2020. **244**: p. 122721.

11. Pinmangkorn, S., et al., *Effect of Ultra-sonicated Y_2BaCuO_5 on Top-Seeded Melt Growth $YBa_2Cu_3O_y$ Bulk Superconductor*. Journal of Superconductivity and Novel Magnetism, 2020.
12. Pavan Kumar Naik, S., et al., *Novel method of tuning the size of Y_2BaCuO_5 particles and their influence on the physical properties of bulk $YBa_2Cu_3O_{7-\delta}$ superconductor*. Applied Physics Express, 2019. **12**(6): p. 063002.
13. Franco, F., L.A. Pérez-Maqueda, and J.L. Pérez-Rodríguez, *The effect of ultrasound on the particle size and structural disorder of a well-ordered kaolinite.* Journal of Colloid and Interface Science, 2004. **274**(1): p. 107-117.
14. Bean, C.P., *Magnetization of High-Field Superconductors.* Reviews of Modern Physics, 1964. **36**(1): p. 31-39.
15. Qian, M., A. Ramirez, and A. Das, *Ultrasonic refinement of magnesium by cavitation: Clarifying the role of wall crystals.* Journal of Crystal Growth, 2009. **311**(14): p. 3708-3715.
16. Bang, J.H. and K.S. Suslick, *Applications of Ultrasound to the Synthesis of Nanostructured Materials.* Advanced Materials, 2010. **22**(10): p. 1039-1059.
17. Namburi, D.K., et al., *A novel, two-step top seeded infiltration and growth process for the fabrication of single grain, bulk (RE)BCO superconductors.* Superconductor Science and Technology, 2016. **29**(9): p. 095010.
18. Muralidhar, M., et al., *Microstructure, critical current density and trapped field experiments in IG-processed Y-123.* Superconductor Science and Technology, 2016. **29**(5): p. 054003.
19. Koblischka-Veneva, A., et al., *Comparison of Temperature and Field Dependencies of the Critical Current Densities of Bulk YBCO, MgB_2, and Iron-Based Superconductors.* IEEE Transactions on Applied Superconductivity, 2019. **29**(5): p. 1-5.
20. Shi, Y., et al., *The growth and superconducting properties of RE–Ba–Cu–O single grains with combined RE elements (RE = Gd and Y).* Superconductor Science and Technology, 2020. **33**(3): p. 035003.

21. Das, D., et al., *Top-seeded infiltration growth of (Y,Gd)$Ba_2Cu_3O_y$ bulk superconductors with high critical current densities.* Superconductor Science and Technology, 2017. **30**(10): p. 105015.
22. Pavan Kumar Naik, S., et al., *Growth and physical properties of top-seeded infiltration growth processed large grain (Gd, Dy) BCO bulk superconductors.* Journal of Applied Physics, 2017. **122**(19): p. 193902.
23. Muralidhar, M., et al., *Microstructure of (Nd,Eu,Gd)-123 matrix with (Nd,Eu,Gd)-211 inclusions.* Journal of Materials Research, 2001. **16**(2): p. 407-412.
24. Setoyama, Y., et al., *Systematic change of flux pinning in (Dy,RE)123 and (Y,RE)123 melt-solidified bulks with unit cell orthorhombicity.* Superconductor Science and Technology, 2014. **28**(1): p. 015014.
25. Iida, K., et al., *Superconducting properties and microstructures of Er–Ba–Cu–O superconductor.* Superconductor Science and Technology, 2003. **16**(6): p. 699.
26. Chen, S.-Y., et al., *Remarkable peak effect in J_c(H, T) of Y–Ba–Cu–O bulk by using infiltration growth (IG) method.* Materials Science and Engineering: B, 2008. **151**(1): p. 31-35.
27. Kim, C.-J. and G.-W. Hong, *Defect formation, distribution and size reduction of in melt-processed YBCO superconductors.* Superconductor Science and Technology, 1999. **12**(3): p. R27-R42.

Chapter 7

Conclusions and Future Prospect

7.1 Conclusions

The aim of this dissertation is to develop a good quality high-temperature bulk $REBa_2Cu_3O_y$ or RE-123 superconductors. We believe that bulk high-quality RE-123 superconductors will be used as a fundamental material in several industrial applications in near future. For large-scale production, an effective sample processing is required that reduces cost and time consumption.

In this work, we developed a fabrication process for RE-123 suitable for fabrication of binary and ternary RE-123 bulk superconductors in air. To obtain the possible best microstructure, the secondary particles were refined by ultra-sonic bombardment technique. To introduce multiple flux pinning centers, we developed a novel ternary (Gd,Y,Er)-123

superconducting compound. The report consists of several chapters' content of which can be summarized as follows:

Chapter 1: A general background of superconductors including history and basic theory is briefly described. The literature review on some examples of melting processes for fabrication of bulk RE-123 is presented along with the research purpose.

Chapter 2: Details of $REBa_2Cu_3O_y$ preparation (RE=rare earth, Gd, Y, and Er), shortly RE-123, of the secondary phase RE_2BaCuO_5, called as RE-211, and $Ba_3Cu_5O_8$ liquid phase (LP) powders for the infiltration growth process of bulk Y-123 and (Gd,Y,Er)-123 superconductors are briefly described. Relevance of grain growth inhibitors is explained, and the ultra-sonication technique used for the powder's refinement is justified. Further, the details of both top seeded melt growth (TSMG) and infiltration growth (IG) together with the oxygen annealing process are discussed. The methods of measuring and analyzing particle size, testing the superconducting properties, and characterizing microstructure are discussed.

Chapter 3: We proposed a fabrication technique that uses high power ultra-sonic waves to control and refine the secondary phase particles explored for fabrication of the bulk superconductors. This ultra-sonication technique successfully refined Y-211 secondary phase particles which provided performance enhancement with reasonable cost and less contamination. In our experiments, the effects of ultra-sonicated Y-211 powder and PtO_2 addition were studied. The samples were grown by TSMG process using ultra-sonicated Y-211 powder. PtO_2 was also added as a grain growth inhibitor. The ultra-sonication time on Y-211 was varied from 0 to 100 minutes with a constant power and frequency. Our results show that the bulk Y-123 samples could be successfully grown with good superconducting performances when the Y-211 was ultra-sonicated for 80 minutes and PtO_2 was used. This resulted in highest J_c of 47 kA/cm^2 at self-field, 77 K and trapped field of 0.47 T under applied field 1 T at 77.3 K.

Chapter 4: The motivation of this chapter is to improve the superconducting properties (J_c and trapped field, TF) by mixing several RE elements. Peritectic temperature (T_p) is one of

the crucial factors for choosing the RE elements. The elements with a low T_p are appropriate for a mixture with good superconducting properties. In our work, the combination of Gd, Y, Er was chosen. Bulk was fabricated using both TSMG and IG processes. Our results show that the Y-123 sample grown by IG process provides a better spatial J_c uniformity at self-field (30.5 %) than in TSMG (42.5 %). In addition, the sample grown by IG process also shows more uniform distribution of Y-211 secondary phase in the Y-123 matrix than the sample grown by TSMG process. According to this result, we finally selected the IG process to fabricate the bulk (Gd,Y,Er)-123 samples.

The $(Gd_{0.33},Y_{0.33-x},Er_{0.33+x})Ba_2Cu_3O_y$ samples were grown by IG process in air with varying X=0, 0.05, 0.1, 0.15 and 0.2. By optimizing the temperature profile, we successfully grew single grain bulks. According to the superconducting property results, $T_{c,onset}$ of all samples was estimated to be around 91.5 K - 92 K, and ΔT_c was less than 1 K. The sample with composition of $(Gd_{0.33}Y_{0.13}Er_{0.53})$-123 (X=0.2) showed TF at 77.3 K as high as 0.53 T. The self-field J_c at 77 and 50 K were 63.05 and 238.86 kA/cm^2, respectively. The analysis of microstructure revealed that the fine (Gd,Y,Er)-211 particles were distributed uniformly in the (Gd,Y,Er)-123 matrix. Our results also established that, with increasing Er concentration, the particles size of (Gd,Y,Er)-211 decreased. Hence, the superconducting performance of the Er-rich (Gd,Y,Er)-123 bulk significantly improved.

Chapter 5: Variation of the microstructure of the (Gd,Y,Er)-211 pellet before and after the reaction with Ba-Cu-O liquid, and the spatial distribution of superconducting properties (T_c and J_c) in (Gd,Y,Er)-123 bulk were studied. First, we studied the preform behavior during heating. Results showed that the RE-211 pellet was stable and remained in the solid form during IG process, but the surface morphology slightly changed due to the high temperature. The FESEM images revealed that the particle sizes and pores in RE-211 preform grew during heating (especially at periphery). Due to thermal gradient, the size of particles and pores varied depending on the positioning in the (Gd,Y,Er)-211 pellet. The value of T_c was almost constant throughout the entire sample. The self-field J_c value increased with increasing distance from the center along *a/b*-axis and decreased with the increasing distance along *c*-axis. The spatial variation of J_c was caused by the non-uniform distribution of (Gd,Y,Er)-

211 particles in the (Gd,Y,Er)-123 matrix. Even though the IG overcame several problems of the TSMG process, inhomogeneity of (Gd,Y,Er)-211 particle size and non-uniformity of superconducting properties have not been resolved completely.

Chapter 6: The optimized ternary bulk $(Gd_{0.33},Y_{0.33-x},Er_{0.33+x})Ba_2Cu_3O_y$ samples grown by IG process with the secondary phase refined by ultra-sonication technique were spatially analyzed. The four-faceted growth and the uniform TF distribution profiles implied single-grain nature of the bulks. The bulk (Gd,Y,Er)-123 samples showed a sharp superconducting transition with the average $T_{c,onset}$ of 91.42 K. The $(Gd_{0.33}Y_{0.13}Er_{0.53})$-123 (X = 0.2) sample achieved the highest TF and J_c values. The value of TF was 0.37 T at 77.3 K measured at 0.3 mm above the top surface. The self-field J_c at 77 and 50 K was 75.56 and 226.80 kA/cm^2, respectively. Use of ultra-sonically refined (Gd,Y,Er)-211 improved the J_c value at self-field approximately by 20% compared to bulks prepared with conventional calcined (Gd,Y,Er)-211. Laboratory production has demonstrated the feasibility of fabrication bulk $(Gd_{0.33},Y_{0.13},Er_{0.53})$-123 superconductors for batch production. In order to reduce production cost of production, the normal furnace that can generate a stable, uniform temperature, were employed for fabricate large number of samples. Nine bulk $(Gd_{0.33},Y_{0.13},Er_{0.53})$-123 samples with reproducible properties were successfully produced and exhibit high trapped filed value by IG process in air combined with a cold-seeding technique for variety of applications.

Due to the several influences on the mixed RE bulk superconductor that effect to the superconducting properties such as chemical fluctuation of the RE-123 matrix and RE-211 secondary phase, so we need to consider on those effects. The refinement of RE-211 secondary particles can improve by optimizing ultra-sonication condition for each RE-211 powder to achieve superior superconducting properties.

Summarizing our results, we optimized fabrication of ternary bulk (Gd,Y,Er)-123 superconductor by IG process using the ultra-sonically refined precursors. The final products demonstrate the potential for batch production of high-performance bulks with low cost and time consumption.

In this study, we showed the benefits of employing the novel ultra-sonication technique. To achieve high-quality and high-performance bulk superconducting material, we explored the ternary (Gd,Y,Er)$Ba_2Cu_3O_y$ superconductor and manifested its excellent properties. We hope this thesis will be beneficial for the young students or researchers who are interested in making the fabrication process cost-efficient, reproducible and reliable.

7.2 Future prospect

This work might be expanded for a further study in the following directions:

- The high-resolution transmission-electron microscopy (HR-TEM) should be utilized to develop further understanding on the formation of mixed RE elements in the matrix and the RE-211 secondary phase particles.
- To explore the microstructure and chemical composition of the substance by high-resolution transmission-electron microscopy (HR-TEM). In this way, the exact boundaries between (1) the matrix and the secondary phase particles and between (2) different secondary phase particles in mixed RE element RE-123 should be understood.

Since the aim of this work is to focus on the fabrication of IG processed large bulk $REBa_2Cu_3O_y$ superconductors in batch production, we expect to continually improve the quality of bulk mixed $REBa_2Cu_3O_y$ superconductors with respect to low cost and time consumption. Homogeneity of superconducting performance is also still challenging issue in this material. For every fabrication process for RE-123, such as top seeded melt growth, infiltration growth, buffer-aided infiltration growth etc., the optimized conditions for mass production need a further investigation.